First Principles Investigation of the Thermodynamic and Kinetic Properties of Lithium Transition Metal Oxides

by

Anton Van der Ven

Submitted to the Department of Materials Science and Engineering
in partial fulfillment of the requirements for the degree of

Doctor of Philosophy in Materials Science

at the

MASSACHUSETTS INSTITUTE OF TECHNOLOGY

Aug 2000

Author .....
Department of Materials Science and Engineering
Aug 15, 2000

Certified by .....8/29/2000.....
Gerbrand Ceder
Union Minière Professor of Materials Science
Thesis Supervisor

Accepted by .....
Carl V. Thompson III
Stavros Salapatas Professor of Electronic Materials
Chairman, Departmental Committee on Graduate Students

First Principles Investigation of the Thermodynamic and Kinetic Properties of Lithium Transition Metal Oxides

by

Anton Van der Ven

Submitted to the Department of Materials Science and Engineering
on Aug 15, 2000, in partial fulfillment of the
requirements for the degree of
Doctor of Philosophy in Materials Science

Abstract

We perform a first principles investigation of the electronic, thermodynamic and kinetic properties of Li_xCoO_2, an important cathode material for rechargeable lithium batteries. In a lithium battery, the lithium concentration x in Li_xCoO_2 can be varied between 0 and 1. Such concentration variations result in important changes of the electronic properties, the relative stability of different forms of Li_xCoO_2 and the mechanisms for lithium diffusion within the CoO_2 host structure. To study the electronic and thermodynamic properties of Li_xCoO_2, we have used density functional theory within the local density approximation (LDA) along with the cluster expansion formalism. We have also developed a scheme to calculate from first principles, the diffusion coefficient in systems with significant configurational disorder.

Building on previous first principles investigations of lithium transition metal oxides, we show that the lithium insertion into CoO_2 results in a shift in the nature of bonding between the cobalt and oxygen ions which is predominantly of a covalent character at low x and progressively becomes more ionic as x increases. The net effect of this change in bonding is an increased polarization of charge toward the oxygen ions. The variation in electronic properties with x is responsible for important structural changes of the host with x.

A thorough investigation of phase stability in the layered form of Li_xCoO_2 has clarified the nature of poorly characterized phase transformations observed experimentally at low x and has exposed the thermodynamic origin of a large structural phase transformation between crystallographically similar forms of Li_xCoO_2 at high x. Within layered Li_xCoO_2, the lithium ions reside in octahedral sites forming a two dimensional triangular lattice between O-Co-O sheets. Our calculations predict a staging transformation around x=0.15 whereby lithium ions segregate to alternating lithium planes leaving the remaining lithium planes vacant. The calculations predict that this phase transformation is accompanied by a dramatic drop in the lattice parameter, c, of the host, a phenomenon observed experimentally. Using thermodynamic arguments, we demonstrate that a concentration driven metal-insulator transition can induce a first order structural phase transformation. We propose that

this mechanism is operative in causing the first-order structural phase transformation in Li_xCoO_2 at high x.

The nature of the crystal structure of the host as well as the presence of defects in the host can be important in determining specific electrochemical properties of lithium intercalation compounds. To determine the effect of crystal structure on the electrochemical properties of Li_xCoO_2 we calculated the properties of the spinel-like form of Li_xCoO_2 and compare them with those of the layered form. Spinel-like Li_xCoO_2 differs from the layered form in that it offers both octahedral as well as tetrahedral interstitial sites for the lithium ions. This results in a voltage versus concentration profile that is significantly different from that of layered Li_xCoO_2. We have also investigated the effect of oxygen vacancies within the layered Li_xCoO_2 host on the compound's electrochemical properties. To this end, we have used a local cluster expansion to describe the dependence of the oxygen vacancy formation energy on the lithium-vacancy arrangement. The calculations show that oxygen vacancies have an important effect on voltage curve especially at high x. Furthermore, we find that oxygen vacancies tend to depress the order-disorder transition temperatures of ordered-lithium phases.

The lithium mobility within the CoO_2 host determines the rate at which lithium ions can be removed and reinserted into the host. A study of the activation barriers in Li_xCoO_2 within the local density approximation shows that the migration mechanism and activation barriers depend strongly on the local lithium-vacancy arrangement around the migrating lithium ion. We identify two hopping mechanisms. The first involves the migration into an isolated vacancy whereby lithium squeezes through a dumbbell of oxygen ions. The second mechanism involves migration into a divacancy whereby the migration path passes through an adjacent tetrahedral site. The latter mechanism has a significantly lower activation barrier than the former. By parameterizing the activation barriers with a local cluster expansion and applying it in kinetic Monte Carlo simulations, we predict that lithium diffusion in layered Li_xCoO_2 is mediated by divacancies at all lithium concentrations except at almost infinite vacancy dilution. Our calculations show that the activation barriers have a strong concentration dependence due to variations in the lattice parameter c and the changes in effective valence of the Co ions with x. This results in a predicted diffusion coefficient that varies within several orders of magnitude with x.

Thesis Supervisor: Gerbrand Ceder
Title: Union Minière Professor of Materials Science

Acknowledgments

I would foremost like to thank my thesis advisor Professor Gerbrand Ceder. His creativity and enthusiasm were an invaluable inspiration throughout my graduate career. Gerbrand's expert guidance, constant encouragement and contagious confidence were essential to make this thesis possible.

I am also grateful to my thesis committee members, Professors Yet-Ming Chiang, Efthimios Kaxiras and Bernhardt Wuensch, whose generosity in accommodating my questions at critical stages of my research is much appreciated. Their unique insights about various aspects of materials science and physics were of great value to my research.

I express special thanks to Patrick Tepesch, Adrian Kohan and Gerardo Garbulsky, former members of our research group who were very helpful during the first years of graduate school. All three are great teachers, who displayed boundless patience with me and whose example made me a better researcher than I would have otherwise been had I not had the opportunity to work alongside them. It was also a great pleasure to work with Patrick again during my summer practicum at Sandia National Laboratory in Livermore, California.

Professor Kadri Aydinol who did much pioneering work on lithium transition metal oxides in our group, was a great pleasure to collaborate with and to have as a friend. Without his initial ground work, much of this thesis would not have been possible. I look forward to other opportunities to work with him.

I am also lucky to have worked in the same group as Dane Morgan and Axel van de Walle with whom I had many useful and stimulating discussions. The ambiance created by other members of the group, Shuba Balasubramanian, Eric Wu, Sally Buta, John Reed, Chris Marianetti, Takeshi Takahashi, Carles Comas Snigdaraj Mishra, Stefano Curtarolo, Dinesh Balachandran Elena Arroyo and Ashley Predith made life in the office enjoyable most of the time and always interesting and entertaining.

It was a pleasure and an enriching experience to work with Mark Asta and Stephen Foiles during my summer practicum at Sandia National Laboratory in Livermore.

The Department of Materials Science and Engineering at MIT and the Department of Energy Computational Science Graduate Fellowship Program are gratefully acknowledged for financial support.

I thank Professor Luc Delaey for his constant encouragements and friendship both during my undergraduate and graduate studies. His colorful and unconventional teaching style made studying materials science exciting and rewarding during my undergraduate years. I am especially grateful for the time he spent with me sharing his wisdom and insights about phase transformations and physical metallurgy.

Thanks to my parents in law, Judy and Colvin Smith for their encouragements and support and for their incentives and bribes to hasten my graduation (such as the lavish graduation gift given several months before the thesis was actually written).

I thank my parents, Paula and Joris, for their unwavering support throughout my life and graduate school years. I have always been able to depend on them and greatly valued their encouragements when I was in doubt.

Most of all, I thank my wife, Aimée Smith whose patience, understanding, humor and love was crucial to make this all possible.

Contents

Chapter 1

Intercalation compounds and electrochemical cells

Lithium transition metal oxides are important intercalation compounds that are well suited for electrochemical applications such as lithium batteries and electrochromic displays. These compounds typically serve as cathodes in electrochemical cells due to their remarkably high voltage with respect to a metallic lithium anode. Li_xCoO_2 is currently one of the most important intercalation compounds. In this thesis, we perform a comprehensive first principles investigation of the electronic, thermodynamic and kinetic properties of Li_xCoO_2. We begin this chapter with a brief description of intercalation compounds (section 1.1) placing our emphasis on lithium transition metal oxides and their important crystal structures (section 1.2). The chapter ends with a motivation and an overview of this thesis (section 1.3).

1.1 Intercalation compounds

Intercalation compounds are a special class of materials that can accommodate foreign species over large concentration intervals. They are characterized by a crystalline host with relatively open one, two or three dimensional channels through which guest ions such as lithium or sodium can migrate freely. A familiar intercalation compound is graphite. It consists of sheets of carbon covalently bonded in an arrangement of a two

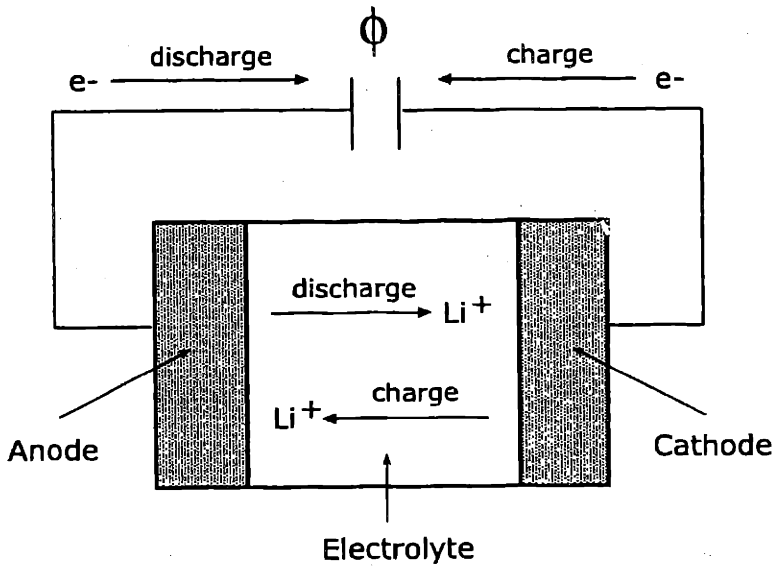

Figure 1-1: Schematic picture of a rechargeable lithium battery.

dimensional honeycomb pattern. The open gaps between the sheets, which are held together by weak Van der Waals forces, enable graphite to serve as host to a wide variety of guest species ranging from alkali metals to molecules. The intercalated guest species can be removed reversibly to form pure graphite again.

Another important category of intercalation compounds are transition metal dichalcogenides denoted by MX_2 with M a transition metal and X a chalcogenide such as oxygen or sulfur. Lithium frequently serves as the guest ion in these compounds and important lithium transition metal dichalcogenides include Li_xTiS_2 [1, 2], Li_xCoO_2 [3] and Li_xMnO_2 [4, 5]. The transition metal dichalcogenides often consist of close-packed planes of sulfur or oxygen ions with transition metal ions ordered over octahedral and/or tetrahedral interstitial sites. During intercalation or deintercalation, lithium ions fill or vacate a subset of the remaining interstitial sites within the host.

The ability of intercalation compounds to undergo large variations in lithium concentration makes them ideal as insertion electrodes in electrochemical cells, in particular in rechargeable lithium batteries [6]. In a lithium battery (Fig. 1-1), lithium ions are shuttled back and forth between an anode and a cathode. The voltage of the battery is proportional to the difference in chemical potentials of lithium

in the cathode and the anode. Both the anode and the cathode are typically an intercalation compound, but the cathode by definition has a higher voltage with respect to a reference electrode of metallic lithium than does the anode intercalation compound. In lithium batteries, graphite is commonly employed as the anode while various lithium transition metal dichalcogenides can serve as the cathode. When the battery is discharged, lithium ions are released at the anode in ionized form and travel through an electrolyte to the cathode. This results in a lowering of the chemical potential of the lithium ions. For each lithium ion released at the anode, an electron travels through the external circuit where it performs work. The free energy reduction associated with the transfer of lithium from the anode to the cathode constitutes the maximum reversible work that can be extracted from the battery. Upon charging the battery, lithium ions are forced back to the anode by an externally imposed voltage. In order for the electrodes to function, they must be both ionically as well as electronically conducting. The electrolyte, which is typically a salt dissolved in an organic solvent or a polymer, must be an electronic insulator but allow for rapid diffusion of lithium in ionized form.

Lithium transition metal dichalcogenides exhibit a variety of interesting thermodynamic, electronic and kinetic properties. As the lithium concentration within Li_xMX_2 is varied, several phenomena can occur [7, 8]. During deintercalation for example, vacancies are introduced on the lithium sites of the host. This produces configurational disorder among the lithium ions and the vacancies. At particular lithium concentrations, it may become energetically favorable for the lithium ions and the vacancies to order. It is also possible that above a critical vacancy concentration, the host becomes unstable or metastable and transforms to a new crystal structure. Phase transformations such as these, though interesting from a scientific point of view, are undesirable for battery applications as they are often accompanied by irreversibilities and large volume changes.

Variations in lithium concentration also produce changes in the electronic properties of the transition metal dichalcogenide host. As lithium is added, its valence electron is generally donated to the host where it can either shift the valence state of the

transition metal ion and/or alter the nature of the bonds between the transition metal and the chalcogenide ions. Changes in lithium concentration have been observed to induce metal-insulator transitions [9, 10], Jahn-Teller distortions [4, 5, 11, 12] as well as magnetic order-disorder transitions of the magnetic moments on the transition metal ions [13, 14, 15].

The lithium diffusivity, which is a measure of the mobility of the lithium ions within the host, is currently not well understood, yet it is an important property since it determines the rate at which lithium ions can be removed and inserted into the cathode. In intercalation compounds, a non-dilute concentration of vacancies is present at most lithium concentrations, a characteristic that is generally absent in many other materials. Complicating an understanding of diffusion in these compounds is the effect of lithium-vacancy disorder and short range order on the collective motion of lithium ions through the host. Furthermore, lithium disorder can be expected to affect migration paths for individual hops as well as their corresponding activation barriers.

Early lithium batteries used Li_xTiS_2 as the cathode, but attention during the last two decades has shifted to lithium transition metal oxides as they have a higher voltage than the transition metal sulfides [6]. Important lithium transition metal oxides include Li_xCoO_2, Li_xNiO_2 and $Li_xMn_2O_4$. Of these three compounds, Li_xCoO_2 currently exhibits the best electrochemical properties and is used as cathode in the majority of commercial lithium batteries [6]. The recent research on compounds such as Li_xNiO_2 and $Li_xMn_2O_4$ has been spurred by a desire to find alternatives for Li_xCoO_2 since cobalt is expensive and slightly toxic. Nevertheless, Li_xNiO_2 is difficult to synthesize without defects [16, 17, 18, 19, 20, 21, 22] and $Li_xMn_2O_4$ degrades rapidly with cycling of the battery due to reasons that are only vaguely understood [23, 24, 25, 26, 27, 28]. The latest trend has, therefore, shifted to identifying alloying additions that could improve the properties of Li_xCoO_2, Li_xNiO_2 and Li_xMnO_2. Compounds such as $Li_xCo_yNi_{1-y}O_2$ [29, 30] , $Li_xMn_yAl_{1-y}O_2$ [31, 32] and most recently $Li_xCr_yMn_{1-y-z}Li_zO_2$ [33] are receiving much attention.

1.2 Crystal Structures

The lithium transition metal oxides that show most promise as cathode materials in rechargeable lithium batteries have either a layered crystal structure or a crystal structure similar to the well-known spinel $MgAl_2O_4$. Compounds such as Li_xCoO_2 [3, 34], Li_xNiO_2 [17] and Li_xMnO_2 [35, 36] are stable or have been synthesized as a metastable layered phase. $Li_xMn_2O_4$ [23] and $Li_xTi_2O_4$ [37] are compounds that are stable in a spinel-like structure and layered $Li_{0.5}NiO_2$ has been observed to transform to spinel upon heating [38]. Furthermore, with recent low temperature synthesis routes, forms of $LiCoO_2$ have been produced that can be considered a defective derivative of the spinel structure [39, 40, 41, 42, 43].

An important layered crystal structure for lithium transition metal oxides is shown in Fig. 1-2(a) and consists of close-packed oxygen planes. Between the oxygen planes are layers of transition metal ions alternated by layers of lithium ions. The layered crystal structure of Fig. 1-2(a), exhibits rhombohedral symmetry and belongs to the $R\bar{3}m$ space group. The close-packed oxygen planes have an ABCABC stacking sequence. The lithium and transition metal ions occupy octahedrally coordinated interstitial sites in the oxygen skeletal framework. The collection of occupied interstitial sites are characterized by an fcc-like connectivity on which the lithium and transition metal ions can be viewed as occupying alternating (111) planes. This layered form is often referred to as O3 [44] and is represented in Fig. 1-2 in an hexagonal setting. The hexagonal unit cell, however, is triply primitive and a primitive cell can be defined in a rhombohedral setting.

When the transition metal oxide serves as a cathode, lithium ions are removed from and reinserted into the lithium layers resulting in the creation and annihilation of vacancies. The octahedral lithium sites of the layered crystal structure form a two dimensional triangular lattice within the lithium layers. Adjacent to the octahedral lithium sites are other interstitial sites which are tetrahedrally instead of octahedrally coordinated by oxygen. These sites form an undulating honeycomb network with the octahedral lithium sites at the center of each hexagon of tetrahedral sites. The

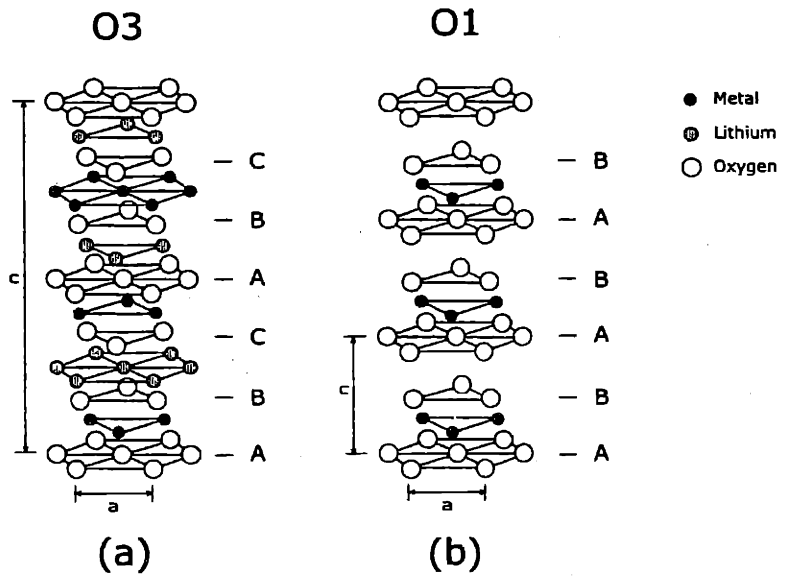

Figure 1-2: Two layered crystal structures that are commonly observed in lithium transition metal oxides. (a) The O3 structure. (b) The O1 structure.

tetrahedral sites are energetically unfavorable for occupation by lithium ions, since they share faces with the oxygen octahedra surrounding the transition metal ions. The close proximity of a lithium ion in a tetrahedral site to the positively charged metal ions results in a large electrostatic repulsion between the two species.

Other layered phases with different stacking sequences are possible and are observed. A common form has an hexagonal close-packed oxygen stacking with ABAB sequence. This form is observed in the deintercalated CoO_2 [45] and NiO_2 [46] compounds. The transition metal ions in this form occupy alternating layers between close-packed oxygen planes. The remaining layers between oxygen planes are vacant. The occupied interstitial sites are characterized by an AAA stacking sequence. This layered form is sometimes referred to as O1 [44]. In nature, it is observed that the O1 crystal structure is more stable when the bonding between the ions is of a covalent nature, while O3 is more stable when the bonding is more ionic. Hence $CdCl_2$, which is characterized by ionic bonding, is stable in the O3 crystal structure while CdI_2, which is more covalent in character, is stable in the O1 crystal structure [47]. Usually, O3 is referred to as the $CdCl_2$ structure and O1 is referred to as the CdI_2 structure.

The other important host structure for lithium transition metal oxides is related

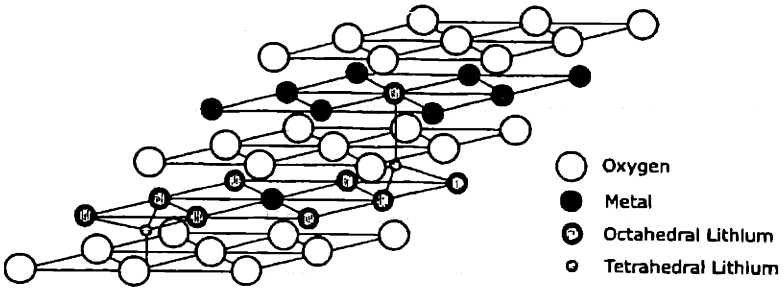

Figure 1-3: The spinel crystal structure. The particular ordering of the transition metal ions results in a set of tetrahedral sites that can be occupied by lithium ions.

to the spinel crystal structure [48] (Fig. 1-3) which also consists of a close-packed oxygen framework. As with the O3 structure, the oxygen planes again have an AB-CABC stacking sequence, however, the transition metal ions are distributed more uniformly among the octahedral interstitial sites: 3/4 of the metal ions reside in alternating layers between close-packed oxygen planes while the remaining 1/4 of the metal ions reside in the other alternating planes. This particular ordering of the metal ions produces a transition metal oxide host structure that exhibits cubic symmetry and belongs to the $Fd\bar{3}m$ space group. While the lithium ions can occupy vacant interstitial octahedral sites in this host a subset of tetrahedral interstitial sites is also available; the metal ordering in spinel results in a set of tetrahedral sites that do not share faces with oxygen octahedra surrounding a metal ion. When compared to spinel $MgAl_2O_4$, the transition metal ions of the spinel-like intercalation compound occupy the same sites as Al and the tetrahedral sites available to lithium correspond to the those occupied by Mg. The availability to lithium of additional tetrahedral sites in the spinel-like host produces marked features in electrochemical properties that are absent in the layered phase. In the remainder of this text, we will refer to Li_xCoO_2 having a spinel-like host simply as spinel Li_xCoO_2.

1.3 Motivation and Overview

In this thesis, we investigate the thermodynamic, electronic and kinetic properties of Li_xCoO_2 from first principles. While Li_xCoO_2 currently ranks among the best cath-

ode materials available, remarkably little is known about its relevant properties. At low lithium concentration, the layered form of Li_xCoO_2 undergoes a series of poorly characterized structural phase transformations that are accompanied by significant volumetric changes [49, 45]. These phase transformations constitute a major impediment to cycling the Li_xCoO_2 compound below x=0.5 in a lithium battery. At high lithium concentration, a large first-order structural phase transformation occurs whereby two crystallographically-equivalent layered forms of Li_xCoO_2 coexist over a large concentration interval [50, 49, 45]. The mechanism by which this phase transformation occurs was previously not understood. The first principles calculations of this thesis remove the uncertainties around these phase transformations. At low lithium concentration, the calculations predict that Li_xCoO_2 undergoes a staging transformation. We also show that the first-order phase transformation at high lithium concentration is driven by a metal-insulator transition.

Other aspects of lithium transition metal oxides that are poorly understood include the effect of defects in the CoO_2 host on the electrochemical properties of the compound and the mechanisms of lithium diffusion within the host structure. In this thesis, we have developed methodologies that enable an investigation of these properties from first principles and we have applied them to Li_xCoO_2.

Because of crystallographic similarities with other lithium transition metal oxides, a comprehensive study of Li_xCoO_2 will be of value in understanding a broad class of technologically-important intercalation compounds. Furthermore, the variety of phase transformations and kinetic phenomena exhibited by Li_xCoO_2 are rarely displayed by more traditional materials. A deeper characterization of these phenomena serves as an enriching addition to our current state of knowledge within the field of materials science.

In the remainder of this text, we focus on four major aspects of Li_xCoO_2.

(i) We study the changes in the electronic properties of Li_xCoO_2 as the lithium concentration is varied.

(ii) We perform an extensive investigation of phase stability in the Li_xCoO_2 system as a function of lithium concentration x and temperature.

(iii) We investigate the effect of the symmetry of the CoO_2 host structure and the presence of defects within the host structure on the electrochemical properties of Li_xCoO_2

(iv) We study the lithium diffusion mechanisms within layered Li_xCoO_2.

The first principles calculation of both thermodynamic and kinetic properties requires as input the energetics arising from the interactions between the constituents of the solid. Currently, the method of choice for calculating first principles energies of solids is density functional theory (DFT) which was developed in the sixties [51, 52]. The starting point of DFT is the electronic charge density as opposed to the many electron wave function. DFT is most commonly implemented within the local density approximation (LDA) [52]. It is only with the significant increases in computer speeds and the major algorithmic improvements [53, 54] of the last decade that a study of systems such as Li_xCoO_2 with DFT-LDA has become possible.

At non-zero temperature entropic effects become important. These can be studied with statistical mechanics. In an intercalation compound such as CoO_2, a major component of the entropy arises from the configurational disorder associated with the many different ways of distributing lithium ions and vacancies over the interstitial sites of the host. A natural tool for studying systems with configurational disorder is the cluster expansion formalism [55] which can be considered a generalization of the Ising model and was put on a firm theoretical footing in the mid- eighties [56]. A cluster expansion enables an accurate and rapid extrapolation of the total energy of any lithium-vacancy arrangement within the CoO_2 from the first-principles energy values of a relatively small number of arrangements. This feature makes it possible to study complicated materials such as Li_xCoO_2 with standard statistical mechanics techniques such as Monte Carlo simulations.

The thesis is divided into two parts. In part I (chapters 2-6), we focus on thermodynamic properties. Chapter 2 reviews the thermodynamics of intercalation compounds and describes the tools used in alloy theory to study phase stability. These include the cluster expansion formalism and density functional theory. In chapter 3, we study the electronic properties of Li_xCoO_2. In chapters 4 and 5, we investigate

phase stability in layered and spinel Li_xCoO_2 respectively. The effect of dilute concentrations of oxygen vacancies on the electrochemical properties of layered Li_xCoO_2 are considered in chapter 6.

In part II (chapters 7 and 8) we focus on kinetic properties. In chapter 7, we describe the elements of irreversible thermodynamics that lead to the well known Kubo-Green equations which relate the macroscopic diffusion coefficient to fluctuations of lithium ions at the atomistic level. We then present a procedure that enables the calculation of the diffusion coefficient in solids with configurational disorder from first principles. We apply this procedure for the study of lithium diffusion in layered Li_xCoO_2 in chapter 8.

Chapter 2

Thermodynamics from first principles

Although solids are complex on a microscopic level, many of their relevant properties can be described with only a limited set of macroscopic thermodynamic and kinetic parameters. Thermodynamics, however, is a phenomenological theory and the desire always exists to obtain a deeper and more mechanistic understanding of the underlying atomic interactions that collectively produce the solid's macroscopic properties. The behavior of the elementary particles (atomic nuclei and electrons) that form the solid is dictated by quantum mechanics. Statistical mechanics serves as the link between the description of the solid on the atomic scale and thermodynamics. Only within recent years has it become possible to implement the tools of these fields to qualitatively, and to an increasing extent also quantitatively, determine and predict thermodynamic properties from first principles. In this chapter, after a preliminary review of the thermodynamics associated with intercalation compounds, we describe the theories that enable the *ab initio* investigation and prediction of phase stability.

2.1 Thermodynamics of intercalation compounds

It is well known that phase stability and the occurrence of phase transformations in a solid at constant temperature T and pressure P are ultimately dictated by the solid's

Gibbs free energy. For most solids, the Gibbs free energy is difficult to obtain. For intercalation compounds such as Li_xMO_2, however, a wealth of information about its free energy, $G^{host}(x)$, can be obtained by a straightforward measurement of the open circuit voltage $V(x)$ of Li_xMO_2 with respect to a reference anode. This convenient fact follows from the Nernst equation [7] which for the Li_xMO_2 compounds can be written as

$$V(x) = -\frac{(\mu_{Li} - \mu_{Li}^{anode})}{ze} \tag{2.1}$$

where z is the valence of Li in the electrolyte (*i.e.* z=1 for Li), e is the charge of an electron, μ_{Li} is the lithium chemical potential in Li_xMO_2 and μ_{Li}^{anode} is the chemical potential of Li in the anode. When the anode is metallic lithium, μ_{Li}^{anode} is constant and knowledge of $V(x)$ then directly yields μ_{Li} through (2.1). G_f^{host}, the Gibbs free energy per Li_xMO_2 formula unit can subsequently be calculated with

$$G_f^{host}(x) = G_f^{host}(x_o) + \int_{x_o}^{x} \mu_{Li} dx \tag{2.2}$$

The simplicity of (2.2) follows from the fact that as the lithium concentration x is varied, the amount of host material MO_2 remains constant in the electrochemical cell. As a result, the lithium chemical potential is simply the slope of G_f^{host} with respect to x since

$$\mu_{Li} = \left(\frac{\partial G^{host}}{\partial n_{Li}}\right)_{T,P,N_{host}} = \left(\frac{\partial G_f^{host}}{\partial x}\right)_{T,P,N_{host}} \tag{2.3}$$

where n_{Li} is the number of lithium ions and can be written as $n_{Li} = xN_{host}$ with N_{host} the number of MO_2 formula units in the cathode. Integrating (2.3) yields (2.2).

The free energy is the characteristic potential that describes the equilibrium state of a solid at fixed concentration, temperature and pressure. Knowledge of $G_f^{host}(x)$ for the relevant phases of Li_xMO_2 can be used to construct an equilibrium concentration versus temperature phase diagram with the familiar common tangent method, a geometric translation of the requirement that the phase(s) with the lowest free energy will be present in thermodynamic equilibrium.

While G_f^{host} at constant T and P is useful to construct a T versus x phase di-

agram for Li_xMO_2, the independent intensive variables in an electrochemical cell containing Li_xMO_2 as a cathode are not T, P and x but are instead T, P and μ_{Li}. In an electrochemical cell, the lithium concentration is changed by a variation of the lithium chemical potential which in turn is determined by the imposed voltage through (2.1). Under these conditions, the characteristic thermodynamic potential is the grand canonical free energy which can be derived from the free energy $G_f^{host}(x)$ through a Legendre transform as

$$\Omega_f^{host} = G_f^{host} - x\mu_{Li} \tag{2.4}$$

With the above two characteristic potentials, G_f^{host} and Ω_f^{host}, it is possible to categorize different types of phase transformations. Phase transformations are accompanied by discontinuities in the derivatives of the characteristic potentials with respect to a particular intensive variable [57, 58, 59]. A distinction is made between phase transformations that cause a discontinuity of the first derivative of the characteristic potential (first order phase transformation) and those that cause a discontinuity or divergence in the second derivative of the characteristic potential (second order phase transformation) [57].

A familiar phase transformation is a polymorphic transition at constant pressure whereby a single-component solid or a multicomponent compound undergoes a structural change upon heating (cooling) above (below) a transition temperature T_o. These transformations are characterized by the release (absorption) of a latent heat as a result of a discontinuity in the enthalpy at T_o, which we denote by ΔH^{host}, between the initial and final phases of the transition. In equilibrium, the free energies of the initial and final phases are equal at T_o and the entropy must, therefore, change discontinuously by $\Delta H^{host}/T_o$ at T_o. Since the entropy is the first derivative of the Gibbs free energy with respect to temperature,

$$S^{host} = -\left(\frac{\partial G^{host}}{\partial T}\right)_{P,x} \tag{2.5}$$

a polymorphic phase transformation is of first order. Examples of second order transformations can include special types of order-disorder transitions of the different species in a multicomponent solid or of the magnetic moments in magnetic materials. These transitions are not characterized by the release or absorption of a latent heat at T_o but instead by a divergence of the heat capacity which is the second derivative of the Gibbs free energy with respect to temperature

$$C_p = \left(\frac{\partial^2 G^{host}}{\partial T^2} \right)_{P,x} \tag{2.6}$$

For intercalation compounds, we also have to consider phase transformations under conditions where the chemical potential is an independent variable. In this case, a first order phase transformation is characterized by a discontinuity in the lithium concentration x since the first derivative of the characteristic potential Ω^{host} with respect to the independent intensive variable μ_{Li} is

$$x = -\left(\frac{\partial \Omega^{host}}{\partial \mu_{Li}} \right)_{T,P} \tag{2.7}$$

This type of phase transformation corresponds to the crossing of a two phase region in a temperature versus concentration phase diagram at constant temperature. Within the T, P and x representation, the concentration defining the endpoints of the transformation are determined by the common tangent to the Gibbs free energies G^{host} of the initial and final phases participating in the transformation. In the two phase region, the lithium chemical potential is constant resulting, according to (2.3), in a plateau in the $V(x)$ curve.

In a second-order transition, the second derivative of Ω^{host} with respect to μ_{Li} diverges. This second derivative is typically called a susceptibility χ_μ which is also related to the reciprocal of the derivative of $V(x)$ with respect to x according to

$$\chi_\mu = -\left(\frac{\partial^2 \Omega^{host}}{\partial \mu_{Li}^2} \right)_{T,P} = -\left(\frac{\partial x}{\partial \mu_{Li}} \right)_{T,P} = \frac{1}{ze} \left(\frac{\partial x}{\partial V} \right)_{T,P} \tag{2.8}$$

The above discussion clearly indicates that a measurement of $V(x)$ not only gives

information about G_f^{host} and Ω_f^{host}, but characteristic features in its shape shed light on the nature of the phase transformations that occur in Li_xMO_2 during the electrochemical variation of the lithium concentration. Experimentally, these measurements can be accompanied by in-situ or ex-situ characterization techniques such as X-ray diffraction, TEM and Neutron diffraction which indicate the types of structural changes that occur during the transformation.

2.2 Statistical mechanics for intercalation compounds

While the thermodynamic properties of a solid in equilibrium are time invariant, at the atomic level the solid fluctuates from one state to another [60, 59]. For values of x in Li_xMO_2 that deviate from stoichiometry, there exists a degree of disorder with respect to the distribution of lithium ions over the possible lithium sites in the MO_2 host. At non-zero temperature, thermal energy enables lithium ions to hop into neighboring vacant sites and the overall lithium vacancy configuration within MO_2 evolves over time. On average though, the degree of disorder as measured by either short-range or long-range order parameters is constant. Other fluctuations within the solid occur on a time scale that is much shorter than that between typical lithium hops. The most important of these are vibrational and electronic excitations. In principle, each excitation can be described by a linear combination of quantized states - that is a particular lithium- vacancy configuration along with a combination of phonon and electronic eigenstates .

Each state s has an energy E_s associated with it which is an eigenvalue of the Schrödinger equation of the solid. When T and P are independent intensive variables it is more appropriate to consider the enthalpy of the state s defined as $H_s = E_s + PV_s$ where V_s is the volume. According to statistical mechanics [60, 59] then, the probability that a system is in a particular state s is

$$P_s = \frac{\exp\left(-H_s/k_BT\right)}{Z} \tag{2.9}$$

where k_B is Boltzmann's constant and Z is the partition function defined as

$$Z = \sum_s \exp\left(-H_s/k_BT\right) \tag{2.10}$$

Eq. (2.9) represents a distribution function that assigns the relative importance of different states in determining thermodynamic averages and reflects the fraction of time that a solid resides in each state s. In this way, the average enthalpy can be calculated as

$$H = \sum_s H_s P_s \tag{2.11}$$

Furthermore, the free energy is related to the partition function according to [60]

$$G = -k_BT \ln(Z) \tag{2.12}$$

Clearly, evaluation of thermodynamic properties using (2.9) - (2.12) is complicated as it requires a knowledge of the energy spectrum of the solid for all relevant excitations. Nevertheless, significant simplications become evident after performing a coarse graining of the partition function [61]. These are based on the realization that the various excitations of the solid occur over time scales that can differ by many orders of magnitude. For any given lithium- vacancy arrangement in Li_xMO_2, the solid typically undergoes a large number of vibrations before a thermal fluctuation produces a configurational rearrangement of the lithium ions. Hence, for every configurational lithium-vacancy arrangement, which we will denote by $\vec{\sigma}$ and specify in more detail later, the assumption can be made that the solid is ergodic with respect to vibrational excitations. For delocalized electronic states, the same assumption can be made with respect to electronic excitations. These observations imply a more natural form for the partition function for solids exhibiting configurational disorder

$$Z = \sum_{\vec{\sigma}} \sum_{s \in \vec{\sigma}} \exp\left(-H_s/k_BT\right) \tag{2.13}$$

where the second summation extends over all the vibrational and electronic states

consistent with a given lithium-vacancy arrangement labeled by $\vec{\sigma}$. By introducing a configuration dependent free energy defined as

$$G(\vec{\sigma}) = -k_B T \ln \left(\sum_{s \in \vec{\sigma}} \exp\left(-H_s / k_B T\right) \right) \tag{2.14}$$

the partition function becomes

$$Z = \sum_{\vec{\sigma}} \exp\left(-G(\vec{\sigma}) / k_B T\right) \tag{2.15}$$

The coarse grained partition function, (2.15), is still formally equivalent to the original partition function, (2.10), though now, its only explicit dependence is configuration $\vec{\sigma}$. By making the assumption that the vibrational and electronic degrees of freedom are ergodic on the time scale characterizing configurational excitations, (2.15) becomes equivalent to the partition function for a *lattice model.* Furthermore, (2.15) shows that in principle, the lattice model should reflect the configuration dependence of $G(\vec{\sigma})$ instead of the energy as is often assumed.

$G(\vec{\sigma})$ can be written as

$$G(\vec{\sigma}) = H_o(\vec{\sigma}) + G^{excitations}(\vec{\sigma}) \tag{2.16}$$

where $H_o(\vec{\sigma})$ is the groundstate enthalpy for the the solid having lithium-vacancy arrangement $\vec{\sigma}$. $G^{excitations}(\vec{\sigma})$ is the difference between $G(\vec{\sigma})$ and $H_o(\vec{\sigma})$ and accounts for the free energy arising from the vibrational and electronic excitations when the solid is in the configuration $\vec{\sigma}$. Experience indicates that for most solids with configurational degrees of freedom on a given parent lattice, inclusion of non-configurational excitations only has a quantitative effect on predicted order-disorder transition temperatures but does not alter the topology of the phase diagram [62, 63, 64, 65, 66]. Although examples exist in which the vibrational entropy difference between an ordered phase and the disordered phase are of a comparable magnitude as the configurational entropy difference [67, 66], in general, we expect vibrational and electronic free energies to approximately cancel when comparing free energies of similar phases

[68, 69, 70, 71].

In this thesis, we neglect electronic and vibrational excitations and evaluate thermodynamic properties by approximating $G(\vec{\sigma})$ by $H(\vec{\sigma})$. The approach used in this thesis to calculate first principles thermodynamic properties in Li_xMO_2 compounds can be divided into three stages [55, 72] that will be described in more detail in the next three sections and can be summarized as follows.

(i) First a variety of first principles total energy calculations of different ordered arrangements of lithium ions and vacancies within MO_2 are performed;

(ii) These energies are then used to parameterize a cluster expansion. A well converged cluster expansion enables an accurate and rapid extrapolation of the total energy of any configuration from the first-principles energy values calculated in the first step;

(iii) The cluster expansion is then used in Monte Carlo simulations to calculate thermodynamic properties.

In section 2.3, we review the cluster expansion [56] which can be considered as a generalized Ising model and is a natural way of describing the configurational dependence of any property of the crystal, in particular the configurational enthalpy $H(\vec{\sigma})$. In order to determine the coefficients of a cluster expansion for a particular system, it is necessary to perform first principles total energy calculations of representative lithium-vacancy arrangements in an MO_2 host. In this thesis we have used the local density approximation [52] of density functional theory [51], described in section 2.4, to obtain numerical solutions to the Schrödinger equation of the solid. Once a cluster expansion has been constructed, thermodynamic properties can be calculated with Monte Carlo simulations [73] which are described in section 2.5.

2.3 Cluster expansion formalism

The lithium ions within a transition metal oxide intercalation compound can be assigned to well defined crystallographic sites. Because of ionic relaxations though, the lithium ions rarely reside exactly at these positions. Nevertheless there exists a one

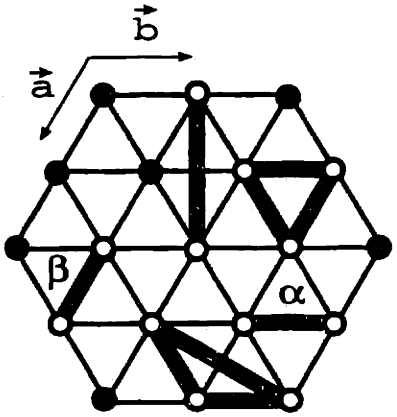

Figure 2-1: Typical clusters on a two dimensional triangular lattice.

to one correspondence between each lithium ion and a crystallographic site. In a given host, there could be m possible lithium sites where m is usually a very large number. Hence there are a total of 2^m possible lithium-vacancy arrangements within the host. It is useful to introduce occupation variables σ_i that are +1 (-1) if a lithium ion (vacancy) resides at site i. The vector $\vec{\sigma}$ which we now define in more detail as $\vec{\sigma} = (\sigma_1, \sigma_2, ..., \sigma_i, ..., \sigma_m)$ then uniquely specifies a configuration within the host. The use of $\vec{\sigma}$, however, is cumbersome and a more versatile way of uniquely characterizing configurations can be achieved with polynomials ϕ_α of occupation variables defined as [56]

$$\phi_\alpha(\vec{\sigma}) = \prod_{i \in \alpha} \sigma_i \tag{2.17}$$

where i are sites belonging to a cluster α of lithium sites within the MO_2 host. Typical examples of clusters are a nearest neighbor pair cluster, a next nearest neighbor pair cluster, a triplet cluster etc. Examples of clusters on a triangular lattice are illustrated in Fig. 2-1. There are 2^m different clusters of lithium sites and therefore 2^m cluster functions $\phi_\alpha(\vec{\sigma})$.

It can be shown [56] that the set of cluster functions $\phi_\alpha(\vec{\sigma})$ form a complete and orthonormal basis in configuration space with respect to the scalar product

$$\langle f, g \rangle = \frac{1}{2^m} \sum_{\vec{\sigma}} f(\vec{\sigma}) g(\vec{\sigma}) \tag{2.18}$$

where f and g are any scalar functions of configuration. The sum in (2.18) extends over all possible configurations of lithium ions and vacancies over the m lithium sites of the MO_2 host. Because of their completeness and orthonormality over the space of configurations, it is possible to expand any function of configuration $f(\vec{\sigma})$ as a linear combination of the cluster functions $\phi_\alpha(\vec{\sigma})$

$$f(\vec{\sigma}) = f_O + \sum_\alpha f_\alpha \phi_\alpha(\vec{\sigma}) \tag{2.19}$$

where the sum extends over all clusters α over the m lithium sites. The coefficients f_α are constants and follow from the scalar product of the function $f(\vec{\sigma})$ with the cluster function $\phi_\alpha(\vec{\sigma})$

$$f_\alpha = \langle f(\vec{\sigma}), \phi_\alpha(\vec{\sigma}) \rangle = \frac{1}{2^m} \sum_{\vec{\sigma}} f(\vec{\sigma}) \phi_\alpha(\vec{\sigma}) \tag{2.20}$$

f_O is the coefficient of the empty cluster $\phi_O = 1$ and is the average of $f(\vec{\sigma})$ over all configurations. (2.19) is referred to as a cluster expansion.

Important examples of functions that depend on configuration are $G(\vec{\sigma})$ and the ground state enthalpy $H_o(\vec{\sigma})$. A cluster expansion of the ground state enthalpy is typically written as

$$H_o = V_O + \sum_\alpha V_\alpha \phi_\alpha(\vec{\sigma}) \tag{2.21}$$

where V_O and V_α are called effective cluster interactions (ECI) and are formally given by

$$V_\alpha = \langle H_o(\vec{\sigma}), \phi_\alpha(\vec{\sigma}) \rangle = \frac{1}{2^m} \sum_{\vec{\sigma}} H_o(\vec{\sigma}) \phi_\alpha(\vec{\sigma}) \tag{2.22}$$

(2.21) can be viewed as a generalized Ising model Hamiltonian containing not only nearest neighbor pair interactions, but also all other pair and multibody interactions extending beyond the nearest neighbors. Through (2.22), a formal link is made between the interaction parameters of the generalized Ising model and the configuration dependent ground state enthalpies of the solid.

Clearly, the cluster expansion for the configurational enthalpy, (2.21), is only

useful if it converges rapidly, *i.e.* there exists a maximal cluster α_{max} such that all ECI corresponding to clusters larger than α_{max} are negligibly small. In this case, the cluster expansion can be truncated to yield

$$H_o(\sigma) = V_O + \sum_{\alpha}^{\alpha_{max}} V_\alpha \phi_\alpha(\vec{\sigma}) \tag{2.23}$$

A-priori mathematical criteria for the convergence of the configurational enthalpy cluster expansion do not exist. Experience indicates that convergence depends on the particular system being considered. In general, though, it can be expected that the lower order clusters extending over a limited range within the crystal will have the largest contribution in the cluster expansion.

As the above exposition illustrates, the cluster expansion is merely a parameterization of the configurational enthalpy in terms of the cluster basis functions ϕ_α. The ECI, V_α, are not to be confused with pair and multi-body potentials that are frequently used for modeling energetics in oxides and metals. They are simply constant expansion coefficients. For a compound such as Li_xMO_2, the number and arrangement of M and O ions remain unchanged as the lithium concentration and/or arrangement are varied. These ions do not contribute to the configurational degrees of freedom within Li_xMO_2 and consequently, there is no explicit reference to them in the cluster expansion. Nevertheless, the cluster expansion describes the enthalpy of the whole crystal. Since, in the expression for V_α in (2.22), the enthalpies $H_o(\vec{\sigma})$ correspond to the fully relaxed ground state enthalpies for configuration $\vec{\sigma}$, the ECI implicitly embody interactions between different lithium ions, lithium ions with the MO_2 host and elastic strain energy due to varying relaxations of the host with changing lithium vacancy arrangements. In general, therefore, it is difficult to attribute simple physical interpretations to the numerical values of the ECI. It is also important to realize that a cluster expansion only describes the configurational dependence of the enthalpy of one particular host structure of MO_2. If other host structures with configurational degrees of freedom compete for stability, a separate cluster expansion needs to be constructed for each of these structures.

2.3.1 Symmetry and the cluster expansion

Simplifications to the cluster expansion (2.21) or (2.23) can be made by taking the symmetry of the crystal into account [55]. Clusters are said to be equivalent by symmetry if they can be mapped onto each other with at least one space group symmetry operation. For example, clusters α and β of Fig. 2-1 are equivalent since a clockwise rotation of β by 60^o followed by a translation by the vector $2\vec{b}$ maps β onto α. The ECI corresponding to clusters that are equivalent by symmetry are equal. In the case of α and β of Fig. 2-1, $V_\alpha = V_\beta$. All clusters that are equivalent by symmetry are said to belong to an orbit Ω_α where α is a representative cluster of the orbit. For any lithium-vacancy arrangement $\vec{\sigma}$ we can define averages over cluster functions $\phi_\alpha(\vec{\sigma})$ as

$$\langle \phi_\alpha(\vec{\sigma}) \rangle = \frac{1}{|\Omega_\alpha|} \sum_{\beta \in \Omega_\alpha} \phi_\beta(\vec{\sigma}) \tag{2.24}$$

where the sum extends over all clusters β belonging to the orbit Ω_α and $|\Omega_\alpha|$ represents the number of clusters that are symmetrically equivalent to α. The $\langle \phi_\alpha(\vec{\sigma}) \rangle$ are commonly referred to as correlation functions. Using the definition of the correlation functions and the fact that symmetrically equivalent clusters have the same ECI, we can rewrite the configurational enthalpy normalized by the number of primitive unit cells N_p (*i.e.* number of Bravais lattice points of the crystal), as

$$h_o(\vec{\sigma}) = \frac{H_o(\vec{\sigma})}{N_p} = \frac{V_O}{N_p} + \sum_\alpha m_\alpha V_\alpha \langle \phi_\alpha(\vec{\sigma}) \rangle \tag{2.25}$$

where m_α is the multiplicity of the cluster α, defined as the number of clusters per Bravais lattice point symmetrically equivalent with α (*i.e.* $m_\alpha = |\Omega_\alpha|/N_p$). The sum in (2.25) is only performed over the non-equivalent clusters.

2.3.2 Local cluster expansion

The description of the cluster expansion formalism so far has been restricted to global extensive properties such as the total energy of the crystal. Local intensive properties that depend on configuration also exist, however. Examples include the configura-

tion dependence of the size of the magnetic moments on ions or the configuration dependence of the local vibrational entropy assigned to each ion. The configuration dependence of local properties can be described with *local cluster expansions*, which were first used by Ozolins [74] and Morgan [70]. The distinction between a global cluster expansion as described in the previous sections and a local cluster expansion lies in the manner in which symmetry is implemented to simplify the expansion (2.19); The symmetry equivalence of clusters appearing in (2.19) is no longer determined by the symmetry operations of the space group of the crystal, but instead by the symmetry operations of the point group at the ionic site at which the local property is to be calculated. As with the global cluster expansion, it is essential that the local cluster expansion can be truncated for clusters beyond a certain distance from the ionic site of interest.

In this thesis, we use a local cluster expansion to describe the effect of dilute oxygen vacancies in the MO_2 host structure on the energetics of arbitrary lithium-vacancy arrangements. In principle, modeling oxygen vacancies in addition to lithium-vacancy disorder in Li_xCoO_2 would require the use of a coupled cluster expansion [75] since the solid is then characterized by configurational disorder on two sublattices that do not interchange species. In the limit of dilute oxygen vacancy concentrations, however, interactions between oxygen vacancies can be neglected. All that is required is a way to calculate the dependence of the oxygen formation enthalpy on lithium-vacancy arrangement. This can be done with a local cluster expansion.

The procedure by which the effect of oxygen vacancies on the total energy of the crystal with arbitrary lithium-vacancy configuration can be modeled within the cluster expansion formalism, is as follows. A global cluster expansion is used to describe the configurational energy of Li_xCoO_2 in the absence of oxygen vacancies. For each lithium-vacancy arrangement, the introduction of an isolated oxygen vacancy results in a change of the energy of the crystal by a specific value ΔE_{O_V}. ΔE_{O_V} depends on the lithium-vacancy arrangement and the position of the oxygen vacancy with respect to the lithium-vacancy arrangement. ΔE_{O_V} can, therefore, be characterized by a local cluster expansion. The total energy of the crystal with an oxygen vacancy is then

simply the sum of the global cluster expansion with the local cluster expansion.

Since the introduction of an oxygen vacancy primarily affects the local environment it is reasonable to expect the local cluster expansion for ΔE_{O_V} to converge for clusters beyond a certain distance away from the vacancy such that the expansion can be truncated. With a truncated local cluster expansion, we can consider more than one oxygen vacancy as long as the ranges of the truncated local cluster expansions for the different vacancies do not overlap. In the dilute limit, this is a reasonable assumption. Furthermore, the migration energy for an oxygen vacancy is almost an order of magnitude larger than that for lithium diffusion. This implies that the oxygen vacancies are relatively immobile and that many lithium-vacancy configurations are sampled for a particular random oxygen vacancy distribution in the dilute limit.

2.3.3 Determination of the ECI

According to (2.22), the ECI for the enthalpy cluster expansion are determined by the first principles ground state enthalpies for all the different configurations $\vec{\sigma}$. Explicitly calculating the ECI according to the scalar product (2.22) is intractable. Techniques, such as direct configurational averaging (DCA), though, have been devised to approximate the scalar product (2.22) [76]. In recent years, the preferred method of obtaining ECI has been with an inversion method [77, 78, 79, 55, 72]. In this approach, a set of enthalpies $h_o(\vec{\sigma}_i)$ for a set of P periodic configurations $\vec{\sigma}_i$ with $i = 1, ..., P$ are calculated from first principles and a truncated form of (2.25) is inverted such that it reproduces the $h_o(\vec{\sigma}_i)$ within a tolerable error when (2.25) is evaluated for configuration $\vec{\sigma}_i$. The simplest inversion scheme uses a least squares fit. A set of ECI, V_α, are determined by minimizing a least squares sum

$$\sum_{i=1}^{P} \left[h_o(\vec{\sigma}_i) - \sum_{\alpha}^{\alpha_{max}} m_\alpha V_\alpha \langle \phi_\alpha(\vec{\sigma}_i) \rangle \right]^2 \tag{2.26}$$

The $\langle \phi_\alpha(\vec{\sigma}_i) \rangle$ are the correlation functions evaluated for the configuration $\vec{\sigma}_i$.

The least squares method yields values for V_α that minimize a sum of the squares of the differences between the first principles enthalpies $h_o(\vec{\sigma}_i)$ and the by the cluster

expansion predicted enthalpies. In this approach, a fit is done to the absolute enthalpies $h_o(\vec{\sigma}_i)$ and no explicit constraints are imposed that ensure that the correct order of the enthalpies for different configurations $\vec{\sigma}_i$ is reproduced by the cluster expansion. Phase stability, however, depends crucially on subtle differences in energies between different ordered phases. Qualitatively incorrect results are obtained if a structure that is predicted to be metastable with a first principles method, is predicted to be stable with the cluster expansion.

Linear programming techniques are ideal in enforcing certain constraints on linear expressions such as the cluster expansion (2.25). Linear programming methods make it possible to impose a variety of inequality constraints on the enthalpies h_o [80]. These constraints typically include requirements that the enthalpies h_o are predicted by the cluster expansion within a predetermined interval of error and that first principles predicted ground states are also predicted to be ground states by the cluster expansion. ECI are then determined that satisfy all the constraints using conventional linear programming methods [80]. If the conditions cannot be met, more terms are included in the truncated cluster expansion. Throughout this thesis, we have used this linear program method [80] to determine ECI.

Other more elaborate schemes for determining ECI have been developed [81, 82, 83]. For example, to speed up convergence of the cluster expansion, contributions to the enthalpies h_o that are not well described with a short-range cluster expansion, such as an elastic strain energy due to concentration dependent volume changes, are subtracted from the h_o [81, 82]. The remainder can subsequently be described with a rapidly converged cluster expansion. In addition to this, schemes have been devised in which a smoothness criteria is imposed on the Fourier transform of the ECI corresponding to pair clusters [83]. The effect of imposing smoothness in reciprocal space is to add constraints that encourage long range pair ECI to have small values. A special feature of this method is that the smoothness constraints make it is possible to have more ECI in the cluster expansion than enthalpy values h_o used in the fit.

2.4 First principles energies

The energies of a large number of periodically ordered configurations are an essential ingredient for the determination of a cluster expansion that accurately reflects the configurational energy of a material. These energies must be calculated from first principles by solving an approximation to the many body Schrödinger equation for the solid [84, 85]. The Schrödinger equation is an eigenvalue equation

$$H\psi = E\psi \tag{2.27}$$

where H is the Hamiltonian operator for the solid, ψ is the many body wave function describing N_e electrons and E is the total energy of the solid. Within the Born-Oppenheimer approximation, the electrons are assumed to instantaneously adjust their state to any change in the positions of the nuclei. The coordinates of the nuclei $\vec{R}_n$ then serve only as parameters in the Schrödinger equation and the Hamiltonian can be written (in atomic units) as

$$H = T + V_{ee} + \sum_j v(\vec{r}_j) + \sum_n \sum_{m<n} \frac{Z_m Z_n}{|\vec{R}_m - \vec{R}_n|} \tag{2.28}$$

T is the electronic kinetic energy operator

$$T = -\frac{1}{2}\sum_j \nabla_j^2 \tag{2.29}$$

and V_{ee} describes the Coulomb interactions between the different electrons

$$V_{ee} = \sum_i \sum_{j<i} \frac{1}{|\vec{r}_j - \vec{r}_i|} \tag{2.30}$$

where the $\vec{r}_j$ refer to the positions of the electrons. The sums in (2.28), (2.29) and (2.30) are over all the electrons in the solid. The third term in (2.28) describes the Coulomb interaction between the electrons and the nuclei of the solid and the last term is the Ewald energy arising from the coulomb interaction between the nuclei

having charge Z_m. The Ewald energy is simply an additive term and does not affect the electronic wavefunction ψ. It can be dropped when solving the eigenvalue equation for the electronic ground state and only needs to be added to the electronic energy to obtain the total energy of the crystal. The electronic wave functions that satisfy the Schrödinger equation must be antisymmetric such that the electrons obey the Pauli exclusion principle.

For solids of practical interest, solving the above many body Schrödinger equation is intractable. Often variational approximations are used whereby an anzatz wave function ψ^a is proposed and the energy of the crystal

$$E = \frac{\langle \psi^a | H | \psi^a \rangle}{\langle \psi^a | \psi^a \rangle} \tag{2.31}$$

is variationally minimized with respect to the wave function. An example of this approach is the Hartree-Fock method [84, 85, 86] in which the anzats wave-function is a Slater determinant of single electron orbitals. Even this approximation is too cumbersome for most solids and in some cases has serious deficiencies.

A different approach to solving (2.27) is with density functional theory (DFT) [51, 86, 87]. As was shown by Hohenberg and Kohn (and extended by Levy) [51, 88], the ground state properties of a crystal are uniquely determined by the electron density

$$\rho(\vec{r}) = \langle \psi | \sum_j \delta(\vec{r} - \vec{r}_j) | \psi \rangle \tag{2.32}$$

The fundamental theorems of density functional theory state that the ground state energy of a solid is a functional of the electron density [51]

$$E[\rho] = F[\rho] + \int \rho(\vec{r}) v(\vec{r}) d\vec{r} \tag{2.33}$$

with

$$F[\rho] = \langle \psi | T + V_{ee} | \psi \rangle \tag{2.34}$$

a universal functional and $v(\vec{r})$ the coulomb potential due to the nuclei of the solid. The ψ in (2.34) is the electronic wave function that minimizes $\langle \psi | T + V_{ee} | \psi \rangle$ subject

to the constraint that ψ produces the density ρ as defined by (2.32) [88]. According to DFT, if the functional $F[\rho]$ were known, the ground state energy of the solid with external potential $v(\vec{r})$ is obtained by variationally minimizing the functional $E[\rho]$ with respect to ρ [51, 86]. The minimization proceeds over the set of all densities ρ that can be obtained with antisymmetric wavefunctions [88].

$F[\rho]$ is not known and approximations to it are therefore necessary. Formally, $F[\rho]$ can also be written as

$$F[\rho] = T[\rho] + V_{ee}[\rho] \tag{2.35}$$

where the kinetic energy and the electron-electron interaction energy are individually expressed as functionals of the electron density. Of the two terms in (2.35), the kinetic energy $T[\rho]$ is the most elusive to approximate with a functional of ρ [87, 86]. To side step this difficulty, Kohn and Sham [52] introduced a different separation of $F[\rho]$ by writing it as

$$F[\rho] = T_s[\rho] + J[\rho] + E_{xc}[\rho] \tag{2.36}$$

where $T_s[\rho]$ is the kinetic energy of a system of non-interacting electrons with density ρ. $J[\rho]$ is often referred to as the Hartree term and is a classical Coulomb energy given by

$$J[\rho] = \frac{1}{2}\int\int \frac{\rho(\vec{r})\rho(\vec{r'})}{|\vec{r}-\vec{r'}|} d\vec{r}d\vec{r'} \tag{2.37}$$

The last term $E_{xc}[\rho]$, called the exchange-correlation energy, can be written as

$$E_{xc}[\rho] = (T[\rho] - T_s[\rho]) + (V_{ee}[\rho] - J[\rho]) \tag{2.38}$$

E_{xc} includes the difference between the kinetic energy of a system of independent electrons with density ρ and the kinetic energy of the actual interacting system with the same density. This difference, though, is generally expected to be small [86] and E_{xc} primarily accounts for a correction to $J[\rho]$ arising from the correlations between electrons. Since the electron density corresponds to a probability distribution and not a charge density in the classical sense, $J[\rho]$ is a mean-field approximation to the electron-electron interactions. Embodied in $J[\rho]$ is the assumption that the proba-

bility of having two electrons at $\vec{r}$ and $\vec{r'}$ respectively is equal to the probability of having an electron at $\vec{r}$ times the probability of having another electron at $\vec{r'}$. Neglected are the conditional probabilities resulting from the fact that if an electron is already present at $\vec{r}$, the probability of having another electron at $\vec{r'}$ will be different than the average probability. These correlations between pairs of electrons are implicitly accounted for by $E_{xc}[\rho]$.

Correlations between electrons, which become more important as $\vec{r}$ and $\vec{r'}$ approach each other, arise from two effects. The first type of correlation results from electrostatic repulsions which ensure that electrons avoid the vicinity of other electrons. These are called *direct correlations.* The second type of correlation has its origin in the Pauli exclusion principle which forbids electrons with parallel spins from having the same spatial position coordinates. This effect does not arise from the many body Hamiltonian, but is enforced by the fact that the wave function is antisymmetric. Since the wave function is continuous, the Pauli exclusion principle implies that the probability of having electrons with the same spin approach each other is small. This correlation is referred to as an *exchange correlation.* The energy contribution of exchange correlation is typically an order of magnitude larger than that of direct correlation [87].

The advantage of introducing the non-interacting kinetic energy functional $T_s[\rho]$ is that it can be calculated exactly with a Slater determinant Ψ_D of independent electron orbitals $\psi_j(\vec{r})$. Substituting Ψ_D into (2.32) yields [86]

$$\rho(\vec{r}) = \sum_j \psi_j^*(\vec{r})\psi_j(\vec{r}) \tag{2.39}$$

while the independent electron kinetic energy functional becomes [86]

$$T_s[\rho] = \langle \Psi_D | T | \Psi_D \rangle = \sum_j^{N_e} \int \psi_j^*(\vec{r}) \left(-\frac{1}{2}\nabla^2 \right) \psi_j(\vec{r}) d\vec{r} \tag{2.40}$$

where Ψ_D, through (2.32), and likewise the ψ_j, through (2.39), produce the electron density ρ. Since it is possible that more than one Ψ_D could produce the same density,

the particular Ψ_D appearing in (2.40) is the one that minimizes $\langle\Psi_D|T|\Psi_D\rangle$ for fixed ρ.

With the Ψ_D and ρ expressed in terms of the independent orbitals ψ_j, Kohn and Sham [52] variationally minimized the energy functional

$$E[\rho] = T_s[\rho] + J[\rho] + E_{xc}[\rho] + \int \rho(\vec{r})v(\vec{r})d\vec{r} \tag{2.41}$$

and obtained what are now referred to as the *self-consistent Kohn-Sham* equations

$$\left[-\frac{1}{2}\nabla^2 + v_{eff}(\vec{r})\right]\psi_j(\vec{r}) = \epsilon_j\psi_j(\vec{r}) \tag{2.42}$$

with

$$v_{eff}(\vec{r}) = v(\vec{r}) + \int \frac{\rho(\vec{r'})}{|\vec{r} - \vec{r'}|}d\vec{r'} + v_{xc}(\vec{r}) \tag{2.43}$$

$v_{xc}(\vec{r})$ is the exchange correlation potential and is the variational derivative of the exchange correlation energy functional

$$v_{xc}(\vec{r}) = \frac{\delta E_{xc}[\rho]}{\delta\rho(\vec{r})} \tag{2.44}$$

An equation of the form (2.42), exists for each electron in the solid. The Kohn-Sham procedure replaces the many body eigenvalue equation (2.27) and (2.28) with a set of independent-electron-like eigenvalue equations. Despite their appearance, however, the Kohn-Sham equations are not independent due to the dependence of v_{eff} on the density ρ which itself is determined by all the orbitals ψ_j according to (2.43). This means that the Kohn-Sham equations are to be solved self-consistently.

2.4.1 The Local Density Approximation

The Kohn-Sham equations as represented in (2.42) are exact provided the universal functional $E_{xc}[\rho]$ (and hence its functional derivative $v_{xc}(\vec{r})$) is known. As with $F[\rho]$ of (2.33) and (2.34), $E_{xc}[\rho]$ is not known. The most common approximation to E_{xc}

is the local density approximation (LDA) [52]. Within LDA, E_{xc} is written as

$$E_{xc}[\rho] = \int \epsilon_{xc}\left(\rho(\vec{r})\right) \rho(\vec{r}) d\vec{r} \tag{2.45}$$

where ϵ_{xc} is the exchange correlation energy per electron at $\vec{r}$. $\epsilon_{xc}(\rho(\vec{r}))$ is set equal to the exchange correlation energy per electron of a homogeneous electron gas with the same density $\rho(\vec{r})$. LDA therefore assumes that ϵ_{xc} is local and neglects the effects of inhomogeneities around $\vec{r}$. There are different parameterizations of ϵ_{xc} as a function of the homogeneous electron gas density ρ. For the LDA calculations performed in this thesis, we have used a parameterization of ϵ_{xc} that was fit by Perdew and Zunger [89] to numerical Monte Carlo calculations performed by Ceperley and Alder [90].

At this point, several caveats of DFT and LDA in particular deserve attention. The orbitals ψ_j and orbital energies ϵ_j of the Kohn-Sham equations do not correspond to real electronic states and electronic energy levels. It is only the total energy and electron density that have any physical meaning. Nevertheless, the KS energy levels often do give a good characterization of the band structure of crystalline materials and are frequently compared to quasi-particle energies measured in photo-emission experiments. The kinetic energy as expressed in terms of the ψ_j by (2.40), is not the real kinetic energy of the solid, though it is a close approximation of it [86]. The local density approximation is exact for a uniform electron density and a good approximation for a slowly varying one. Furthermore, for many solids exhibiting rapidly varying electron densities, LDA has proven surprisingly accurate. Yet, for solids in which the electronic states are highly localized in space, we can expect LDA to break down since it cannot be expected to capture the strong correlations between the localized electrons.

For systems with well localized electrons, specific inadequacies of the local density approximation can be identified. One inadequacy is that the approximation to the exchange-correlation potential v_{xc} depends only on the local density and not on the specific orbital that a particular localized electron occupies. In the Hartree-Fock approximation for example, the exchange energy, which is exact within the approxi-

mation of the anzats wave function, is a non-local integral between different electron orbitals. These integrals not only depend on the local electron density, but also on the shape of the different orbitals. Similar orbital dependencies can be expected to arise from direct correlations. Methods such as LDA+U attempt to remedy this deficiency of LDA [91]. Another major inadequacy of LDA is that it has self-interaction (see *e.g.* [86]). In reality, electrons interact with other electrons. They do not interact electrostatically with themselves. In the Hartree term $J[\rho]$ defined by (2.37) of the energy functional (2.41), a coulomb interaction of each electron with itself is included. For the exact $E_{xc}[\rho]$ functional, this self-interaction component is canceled out. (In the Hartree-Fock approximation, the self-interaction in the Hartree term is explicitly canceled out by an identical term in the exchange term). When an approximation for E_{xc} is used, however, the self-interaction does not cancel. This error becomes severe for well localized electronic states. LDA calculations with self-interaction corrections were pioneered by Perdew and Zunger [89] and have been used to investigate the electronic properties of several transition metal oxides [92] and semiconductors [93]. Incorporating self-interaction corrections leads to orbital dependent effective potentials [94] which complicates the numerical solution of the energy and charge density.

2.4.2 The pseudopotential method

Many numerical techniques exist for solving the Kohn-Sham equations. For oxides, the most reliable methods have proven to be [95, 96] the Linear Augmented Plane Wave (LAPW) method [97] and the pseudopotential method [98, 99]. The LAPW method is currently considered the most accurate and hence the standard, yet it is computationally the most costly. In the pseudopotential method, the effect of the core electrons around the ions that do not participate in bonding are replaced by a pseudopotential. The pseudopotentials are designed such that the valence single electron pseudo-wave functions have the same scattering properties as the actual valence electrons would have with the core electrons. The pseudopotential approximation is valid as long as the core electrons do not participate in the bonding of the solid

- that is the changes in their wave functions and energy levels are negligible when the atom is placed in different environments. For most solids this approximation is valid. Comparisons of energy differences for the Li_xCoO_2 system has shown that the pseudopotential method used in this work and the LAPW calculations of Wolverton [100] agree to within 10 meV per Li_xCoO_2 formula unit. Modern pseudopotentials are determined from all electron calculations of atoms making the pseudopotential method a first principles approach [101, 102, 103, 104, 105, 53].

The general procedure of solving the Kohn-Sham equations is to expand the orbitals $\psi_j(\vec{r})$ in terms of a set of basis functions. For infinitely large solids (*i.e.* thermodynamic limit), there are an infinite number of ψ_j's and ϵ_j's. Accord ng to Bloch's theorem [84, 85] for periodic solids, solutions to Kohn-Sham like equations for electron j can be written as

$$\psi_j(\vec{r}) = \psi_{n,\vec{k}}(\vec{r}) = e^{i\vec{k}\vec{r}} u_{n,\vec{k}}(\vec{r}) \tag{2.46}$$

where a wave vector in reciprocal space $\vec{k}$ and a band index n specify electron j and $u_{n,\vec{k}}(\vec{r})$ is a function with the periodicity of the Bravais lattice. The usefulness of Bloch's theorem is that it enables the problem of solving for an infinite number of orbitals and energy levels to be cast into a problem of solving for a finite number of orbitals and energy levels at an infinite number of $\vec{k}$ points. At each $\vec{k}$ point, only a finite number of levels denoted by n are filled (*i.e.* the number of levels equals the number of electrons per Bravais lattice site). The orbital energy levels are continuous functions of $\vec{k}$ and can therefore be written as $\epsilon_n(\vec{k})$. This means that $\epsilon_n(\vec{k})$ can be calculated at a finite number of $\vec{k}$ points and any interpolation scheme can be used to characterize the full $\vec{k}$ dependence of the orbital energies.

In the pseudopotential method, the orbitals $\psi_j(\vec{r})$ are expanded in plane waves

$$\psi_{n,\vec{k}}(\vec{r}) = e^{i\vec{k}\vec{r}} \sum_{\vec{G}} c_{n,\vec{G}}(\vec{k}) e^{i\vec{G}\vec{r}} \tag{2.47}$$

where the $\vec{G}$ are reciprocal lattice vectors and $c_{n,\vec{G}}(\vec{k})$ are expansion coefficients to be determined. In principle, the sum is over all reciprocal lattice vectors $\vec{G}$ though in

practice, the expansion is truncated beyond some energy cutoff E_{max} with $E_{max} = (1/2)|\vec{k} + \vec{G}_{max}|^2$ (in atomic units).

Since the Kohn-Sham equations (2.42) depend on the charge density, the equations must be solved iteratively. In the first step, a trial charge density is proposed (typically a superposition of the charge densities of the free atoms). This is used to calculate $v_{eff}(\vec{r})$ given by (2.43). Then at suitably chosen $\vec{k}$ points, the coefficients $c_{n,\vec{G}}(\vec{k})$ and energy levels $\epsilon_n(\vec{k})$ are determined for the initial charge density. These coefficients and energy levels satisfy the following matrix eigenvalue equation

$$\left[H(\vec{k}) - \epsilon_n(\vec{k})S(\vec{k})\right]\vec{c}_n(\vec{k}) = \vec{0} \tag{2.48}$$

where $H(\vec{k})$ is a matrix containing $\left\langle \vec{G} + \vec{k}|H|\vec{G}' + \vec{k}\right\rangle$ as elements for all values of $\vec{G}$ in the expansion (2.47), $S(\vec{k})$ is an overlap matrix and $\vec{c}_n(\vec{k})$ is a column vector containing the coefficients $c_{n,\vec{G}}(\vec{k})$. At each $\vec{k}$, coefficients and energy levels need only be determined for n ranging the lowest occupied levels. With the set of $c_{n,\vec{G}}(\vec{k})$ a new charge density can be determined using (2.39). This charge density is mixed with the old charge density (this is done for numerical reasons) and the resultant density is used to again calculate a $v_{eff}(\vec{r})$. The above procedure is repeated until the energy and the charge density are converged. Many different efficient numerical techniques exist to solve for the coefficients $c_{n,\vec{G}}(\vec{k})$ and energy levels $\epsilon_n(\vec{k})$ at each iteration step. See for example references [106, 54, 107] and references there in.

In this thesis, we have performed the pseudopotential calculations with the Vienna *ab initio* simulation package (VASP) [54, 107]. This code implements ultra-soft Vanderbilt pseudopotentials [53], the latest development in pseudopotential theory. Ultra-soft pseudopotentials allow for plane wave expansions with significantly lower cutoffs E_{max} than traditional pseudopotentials, making it possible to investigate large and complicated systems, including transition metal oxides, compounds that were intractable with conventional pseudopotentials.

2.5 Monte Carlo simulations

In statistical mechanics, Monte Carlo simulations are used to calculate thermodynamic averages. For a lattice model, a Monte Carlo simulation samples different lithium vacancy configurations with relative frequencies given by the probability distribution function (2.9). This is achieved with a Markov chain of configurations where each configuration is derived from a previous configuration according to a suitable transition probability.

The transition probability most often implemented is due to Metropolis. The algorithm starts with an arbitrary configuration. New configurations are created by picking lattice sites either sequentially or at random and by changing the value of their occupation variable according to a pre-established rule in which a transition probability $w(i \rightarrow f)$ is compared to a random number between 0 and 1. i refers to the configuration before the transition and f corresponds to the configuration after the transition. For the lithium ions and vacancies within lithium transition metal oxides, a typical transition in the grand canonical ensemble would be a change in the value of an occupation variable of a particular lithium site from $+1(-1)$ to $-1(+1)$. A suitable transition probability is then

$$w(i \rightarrow f) = 1 \qquad \Omega(\vec{\sigma}_f) < \Omega(\vec{\sigma}_i) \tag{2.49}$$

and

$$w(i \rightarrow f) = \exp\left(\frac{-\left(\Omega(\vec{\sigma}_f) - \Omega(\vec{\sigma}_i)\right)}{kT}\right) \qquad \Omega(\vec{\sigma}_f) \geq \Omega(\vec{\sigma}_i) \tag{2.50}$$

where Ω is the grand canonical energy defined as

$$\Omega(\vec{\sigma}) = H(\vec{\sigma}) - \mu N \tag{2.51}$$

$H(\vec{\sigma})$ is the enthalpy of configuration $\vec{\sigma}$, μ is the chemical potential and N corresponds to the number of lithium ions in the simulation. If the transition probability $w(i \rightarrow j)$ is greater than a chosen random number, the new configuration $\vec{\sigma}_f$ is accepted. If $w(i \rightarrow j)$ is less than the random number, the previous configuration $\vec{\sigma}_i$ is kept.

In the canonical ensemble, candidate configurations are sampled by for example exchanging lithium between an occupied and a vacant site. The transition probability for these changes is similar to (2.49) and (2.50) with the exception that the $\Omega(\vec{\sigma}_i)$ and $\Omega(\vec{\sigma}_j)$ should be replaced by the initial and final enthalpies $H(\vec{\sigma}_i)$ and $H(\vec{\sigma}_j)$.

Once converged, the metropolis algorithm guarantees that the configurations sampled in a Monte Carlo simulation occur with a frequency given by the probability distribution function (2.9). Hence thermodynamic averages such as the average enthalpy given by (2.11) can be obtained as simple arithmetic averages over the sampled configurations. Within a Monte Carlo simulation, the positions of the lattice sites of a finite sized crystal are stored in memory with periodic boundary conditions and the enthalpy of the sampled configurations are calculated with a cluster expansion. We can distinguish between two types of simulations: (i) cooling or heating simulations at constant μ (in the grand canonical ensemble) or constant x (in the canonical ensemble); and (ii) simulations in which the chemical potential is varied at constant temperature. At fixed T and μ or T and x, a large number of configurations are sampled with the metropolis algorithm. A Monte Carlo step has passed once every lithium site in the Monte Carlo cell has been queried on average once. Typically on the order of 1000-10000 MC steps are required to obtain convergence and the first several hundred to a thousand MC steps are omitted from the averaging as these initial states are not representative of equilibrium. As the external thermodynamic variables (*i.e.* T and μ or T and x) are varied, the starting configuration of the Markov chain under the new conditions is often taken to be the final configuration at the previous external conditions.

As described in section 2.1, phase transitions are characterized by discontinuities or divergences of thermodynamic potentials. First order transformations are exposed in Monte Carlo simulations by a discontinuity in for example the enthalpy with temperature or the concentration with chemical potential. First order transformations in Monte Carlo simulations, as in reality, are accompanied by hysteresis. The hysteresis increases as the size of the Monte Carlo simulation cell increases.

Second order phase transitions are characterized by a divergence in thermody-

namic response functions such as the heat capacity or the susceptibility. These can be calculated from the fluctuations in enthalpy or concentration. It can be shown that the heat capacity is given by

$$C_P = \frac{\partial H}{\partial T} = \frac{\langle H^2 \rangle - \langle H \rangle^2}{k_B T^2} \tag{2.52}$$

Likewise, the susceptibility is given by

$$\chi_\mu = \frac{\partial x}{\partial \mu} = \frac{\langle N^2 \rangle - \langle N \rangle^2}{k_B T} \tag{2.53}$$

where N corresponds to the number of lithium ions in a grand canonical Monte Carlo simulation. Since the correlation length at a second order transition becomes infinite, the Monte Carlo results exhibit finite size effects.

Free energies can be obtained from results of Monte Carlo simulations by integrating the chemical potential as a function of concentration x as prescribed by (2.2). As starting point of the integration, it is useful to set x_o=0 or 1 since the configurational entropy at these concentrations are zero. Neglecting non-configurational sources of entropy, the free energy at x_o=0 or 1 is simply equal to the energy of the solid.

The temperature dependence of the free energy can also be obtained by integration of Monte Carlo data. From the following thermodynamic relation

$$\left[\frac{\partial\left(\frac{G_f^{host}}{T}\right)}{\partial T}\right]_{P,x} = -\frac{H_f^{host}}{T^2} \tag{2.54}$$

the difference of G_f^{host} at two different temperatures is given by

$$\frac{G_f^{host}(T_2)}{T_2} - \frac{G_f^{host}(T_1)}{T_1} = -\int_{T_1}^{T_2} \frac{H_f^{host}(T)}{T^2} dT \tag{2.55}$$

where $H_f^{host}(T)$ is a straightforward by product of the Monte Carlo simulations.

Chapter 3

Electronic structure of Li_xCoO_2

The ability of lithium transition metal oxides to undergo large variations in lithium concentration is attributable to the flexibility of the valence electronic structure of the transition metal ions. Lithium is generally completely ionized within the oxide [108], having donated its valence electron to the the host. The electronic properties of the transition metal oxide are dictated to a large extent by the interaction of the valence *d*-levels of the transition metal with the valence *p*-levels of the oxygen ions. In both the layered and spinel crystal structures, the transition metal is octahedrally coordinated by oxygen.

Fig. 3-1 illustrates the electronic charge densities of hydrogenic *d*-orbitals within an octahedral oxygen environment. Although the five *d* levels when occupied by a

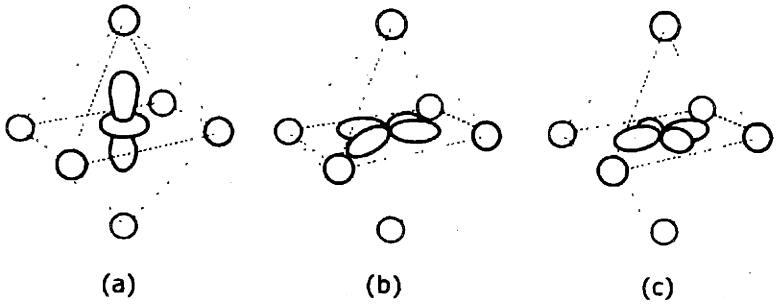

Figure 3-1: Hydrogenic *d*-orbitals within an octahedral oxygen environment. (a) The $d_{3z^2-r^2}$ and (b) the $d_{x^2-y^2}$ orbitals have lobes pointing toward the oxygen ions. (c) The d_{xy} orbital, which is symmetrically equivalent to the d_{xz} and d_{yz} orbitals, has lobes pointing between oxygen ions.

single electron outside of a closed shell core are degenerate in a free transition metal ion, in an octahedral environment, this degeneracy is broken. Crystal field theory [109, 110, 111, 112], for example, shows that the interaction of the d orbitals with the electrostatic potential due to the negatively charged oxygen ions of the octahedron produces an increase in the energy of the $d_{3z^2-r^2}$ and $d_{x^2-y^2}$ orbitals with respect to the energy of the d_{xy}, d_{xz} and d_{yz} orbitals. This occurs because the $d_{3z^2-r^2}$ and $d_{x^2-y^2}$ orbitals have lobes pointing toward the negatively charged oxygen ions while the lobes of the d_{xy}, d_{xz} and d_{yz} orbitals point between oxygen ions.

Simply considering the effect of the electrostatic field of the oxygen ions neglects the important role of covalency that can exist between the transition metal ion and the oxygen ions. A more accurate picture of the interaction between the transition metal ion with the surrounding oxygen ions arises from molecular orbital theory [109, 110, 111, 112]. The $d_{3z^2-r^2}$ and $d_{x^2-y^2}$ orbitals directly overlap with the p_x, p_y and p_z orbitals of oxygen forming bonding and antibonding σ levels referred to as e_g^b and e_g^*. These levels are illustrated schematically in Fig. 3-2. Since the energy of the p orbitals are below the energy of the d orbitals, the bonding e_g^b levels are predominantly of oxygen p character while the antibonding e_g^* levels (frequently referred to as simply e_g) consist mainly of metal d states. This dichotomy in character between the bonding and antibonding levels becomes more pronounced as the difference in the energy of the metal d-levels and the oxygen p-levels widens.

The d_{xy}, d_{xz} and d_{yz} orbitals which do not directly overlap with oxygen p orbitals to form σ bonds, are frequently said to form a set of nonbonding levels denoted by t_{2g} [109, 110, 111, 112]. A band gap Δ_o separates the t_{2g} levels from the antibonding e_g levels. In an octahedral environment, the t_{2g} levels are below the e_g levels. This band gap can be attributed to the larger electrostatic repulsion between an electron in the $d_{3z^2-r^2}$ and $d_{x^2-y^2}$ orbitals with the negatively charged oxygen ions as compared to the electrostatic repulsion between an electron in d_{xy}, d_{xz} and d_{yz} orbitals with oxygen. Although the d_{xy}, d_{xz} and d_{yz} orbitals do not form σ bonds with the oxygen ions, they do form π bonds with the p orbitals on oxygen [109]. Instead of being non-bonding levels, t_{2g} energy levels of Fig. 3-2, more accurately correspond to the

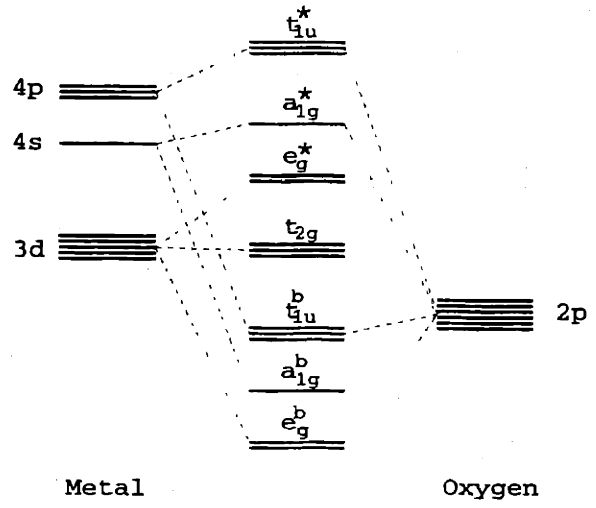

Figure 3-2: Schematic illustration of the bonding and antibonding levels that arise for a transition metal ion in an oxygen octahedral environment due to the hybridization between the valence electronic states of the transition metal ion with those of the oxygen ions.

bonding levels of the π overlap between d_{xy}, d_{xz} and d_{yz} and the oxygen p levels. Increased covalency of this π bond will result in a lowering of the energy of the t_{2g} levels and hence an increase in the band gap Δ_o [109].

Other levels arise from the overlap of oxygen p-levels with the transition metal $4s$ and $4p$ levels. These are referred to as t_{1u} and a_{1g}. Since the energy of the oxygen p levels are again below the energy of the metal $4s$ and $4p$ levels, the bonding t_{1u} and a_{1g} levels are predominantly of oxygen character.

In a crystal, the levels of Fig. 3-2 become bands. Furthermore, although the transition metal ions reside in octahedral interstitial sites, the remainder of the crystal outside of the octahedral site generally does not exhibit the symmetry of a perfect octahedron. Hence the degeneracy of the levels is further broken. Nevertheless, the schematic picture of Fig. 3-2 still persists in the band structure. Fig. 3-3 illustrates the within the local density approximation calculated electronic band structures for CoO_2 and $LiCoO_2$ [113, 114]. The lowest six bands correspond to the e_g^b, t_{1u} and a_{1g} levels of Fig. 3-2 which we will refer to as the oxygen p-levels. The next three levels are the t_{2g} levels and the highest two levels correspond to the e_g bands. In $LiCoO_2$, the Fermi level lies between the t_{2g} and the e_g levels, making the compound

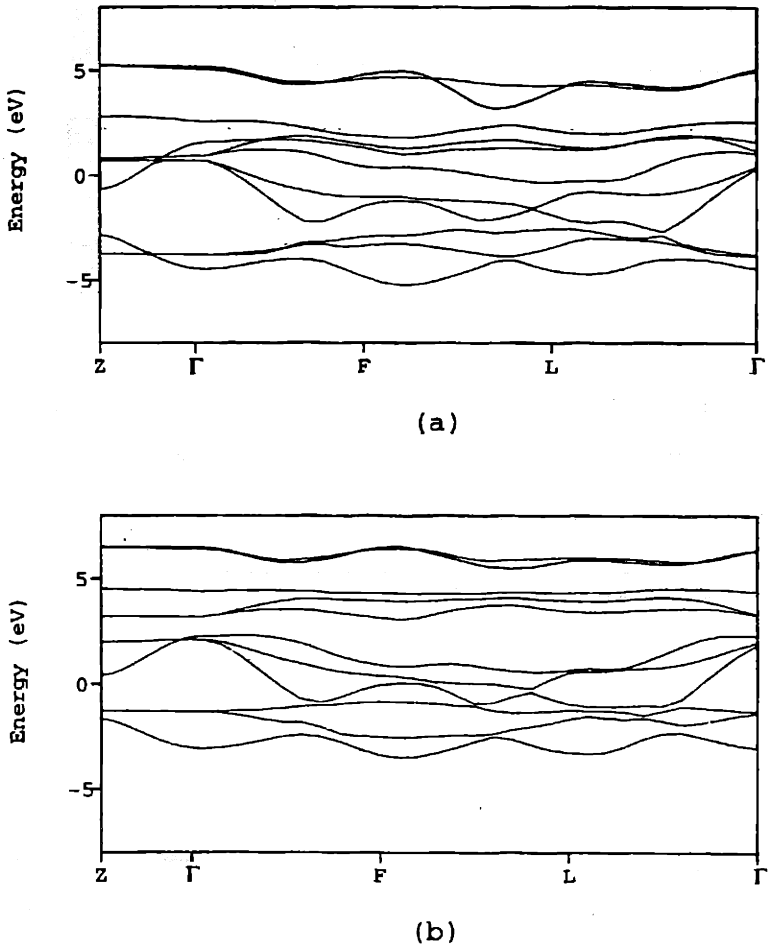

Figure 3-3: The partial band structures of (a) CoO_2 and (b) $LiCoO_2$ as calculated within the local density approximation. The dashed line shows the Fermi level.

a semiconductor. This is consistent with the experimental observations of van Elp *et. al.* [115]. When all the lithium ions are removed, the Fermi level resides in the t_{2g} bands as one electron per CoO_2 formula unit is removed.

The band structures of $LiCoO_2$ and CoO_2 are qualitatively similar. An important difference between the two band structures is the distance between the oxygen p like levels and the t_{2g} levels which is larger in $LiCoO_2$ than in CoO_2. The electron donated by Li to the CoO_2 host resides in a t_{2g} level. Through Coulombic interaction, the addition of the extra electron to the t_{2g} levels raises the energy of the other occupied t_{2g} levels thus increasing the distance between the metallic d-states and the oxygen p-states. This results in a reduction in the hybridization between the Co d-levels and the oxygen p-levels which translates into a change in the nature of bonding from a more covalent character in CoO_2 to a more ionic character in $LiCoO_2$.

To better understand this shift in bonding characteristics with Li insertion, it is useful to inspect a charge difference plot [116]. Fig. 3-4 shows a charge difference plot between Li_xCoO_2 at x=1/4 and CoO_2 both in the layered O3 structure of Fig. 1-2. Electronic charge densities were calculated with the pseudopotential method in the local density approximation for both $Li_{1/4}CoO_2$ and CoO_2. The lattice parameters and the positions of Co and O were the same in the two structures to enable a point by point subtraction of the charge density of CoO_2 from $Li_{1/4}CoO_2$. The resulting difference shows how the electron distribution changes when Li is added to the host, and in particular, where the electron of the added lithium resides. The plane illustrated in Fig. 3-4 corresponds to the shaded plane shown in Fig. 3-5. This plane cuts through Li, Co and O ions.

The charge difference plot illustrates that lithium intercalation induces a significant redistribution of charge within the CoO_2 host [116, 117]. Fig. 3-4 shows that there is an accumulation of charge density around all the Co ions in lobes pointing in directions between oxygen ions. This increase in charge results from an electron addition to the partially filled t_{2g} bands as lithium is added to the host. The charge accumulation occurs around all the cobalt ions indicating that these states are delocalized. Fig. 3-4 also shows that there is a significant depletion in electron density

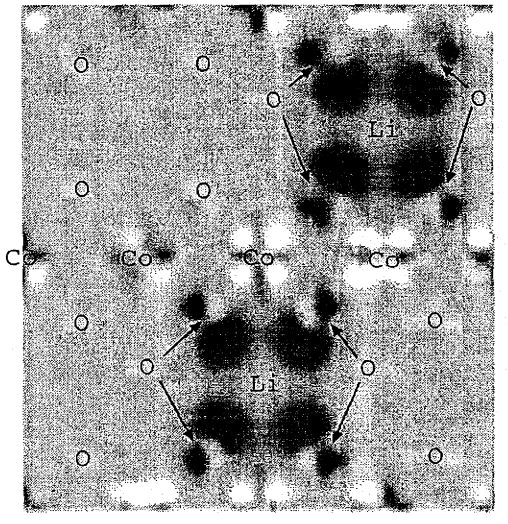

Figure 3-4: Charge difference plot between $Li_{1/4}CoO_2$ and CoO_2. Dark shade signify regions of charge accumulation and light areas correspond to regions of charge depletion.

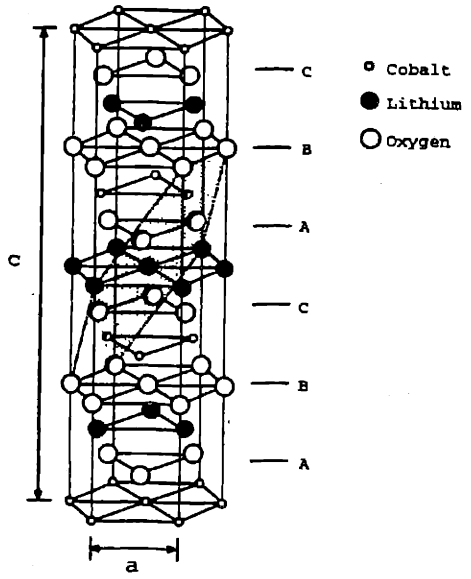

Figure 3-5: The O3 crystal of $LiCoO_2$. The crystallographic plane on which the electronic charge density difference is viewed in Fig. 3-4 corresponds to the shaded plane in this figure.

around the Co ions closest to the lithium ions. The charge depletion occurs in regions that resemble the charge density of a $d_{x^2-y^2}$ atomic orbital. The $d_{x^2-y^2}$ atomic orbital together with the oxygen p orbitals form the σ bonding e_g^b and anti-bonding e_g^* bands. The depletion around the Co ions coincides with a significant increase in charge density in atomic p-like orbitals on oxygen ions which point toward the lithium ions and also overlap with the depleted cobalt $d_{x^2-y^2}$ like lobes.

The simultaneous depletion of charge in $d_{x^2-y^2}$ like orbitals around cobalt and accumulation of charge around oxygen indicates a change in the polarization of the σ e_g bonds between oxygen and cobalt. Since the antibonding e_g^* bands are unoccupied in Li_xCoO_2, the polarization of the σ bond reflects changes in the nature of the bonding e_g^b bands. As lithium is added, the e_g^b bands obtain more of an oxygen character and less of a Co character since the added electron from lithium increases the separation between the energy of the Co d levels and the oxygen p levels. This causes the σ bond between Co and oxygen to become less covalent and more ionic with increasing x [116]. The result is a significant increase in the electron density at the oxygen sites immediately surrounding the lithium ions. The net effect is that the

electron transfer from lithium to the host is very local and occurs predominantly to the oxygen ions [108, 114].

The conventional picture of lithium transition metal oxides, is that the electron donated to the host by lithium is transferred to the transition metal where it shifts its valence state. Previous first principles work [108, 114, 117, 116] and the results of this chapter show that the electronic changes of the host with x are in fact more subtle. The addition of lithium to the CoO_2 host causes a shift in the nature of the bond between oxygen and cobalt from a covalent character at low lithium concentration to a more ionic character at high x. While the electron donated by lithium is added to the t_{2g} band, which is predominantly of Co d character, the effect of this addition is to polarize the Co-O bond such that the charge around the oxygen ions actually increases upon lithium insertion (it is important to realize that oxygen is not in its fully ionized state of -2 in CoO_2). This insight is of importance in understanding the concentration dependence of structural properties and the sequence of stable phases with x predicted in the next chapter for layered Li_xCoO_2. It is also of importance in understanding the non-negligible concentration dependence of the activation barrier for lithium diffusion (chapter 8).

Chapter 4

Phase stability in layered Li_xCoO_2

4.1 Introduction

The layered form of Li_xCoO_2 exhibits a variety of phase transformations that are typical of many intercalation compounds. It is therefore ideally suited for a detailed theoretical study. Layered $LiCoO_2$ was first discovered to be electrochemically active by Mizushima *et. al.* [3] in 1980. Since then, it has served as an archetypal cathode material for rechargeable lithium batteries. Fully lithiated (*i.e.* $LiCoO_2$), the compound has rhombohedral symmetry and its crystal structure is illustrated in Fig 1-2 and described in chapter 1.

Li_xCoO_2 undergoes only small structural changes as it is deinteracalated to a lithium concentration of x=0.3 and when variations in lithium concentration are limited between x=0.5 and 1 the intercalation/deintercalation process is almost perfectly reversible [50, 49, 45]. As the lithium concentration is varied, a series of phase transformations occur in Li_xCoO_2 ranging from ordering reactions [50], transformations of an electronic nature [9, 10] as well as structural transformations of the host [49, 45]. Reimers and Dahn [50] observed that the lithium ions order in rows at x=1/2 and measured an order-disorder transition temperature around 60^o C. At high lithium concentration, the compound undergoes a dramatic change in its electronic properties [9, 10]. $LiCoO_2$ is a semiconductor [115] while Li_xCoO_2 at concentrations below x=0.75 is metallic [9, 10], implying that a metal insulator transition occurs at in-

termediate lithium concentration. Curiously, superimposed on this metal-insulator transition is a two-phase coexistence region between crystallographically identical host structures [50, 49, 45]. At room temperature, this two-phase region is found to exist between x=0.75 and 0.95. At dilute lithium concentration, transformations of yet another type occur involving structural changes of the layered host. As the lithium concentration is brought below about x=0.2, the layered O3 crystal structure of Fig. 1-2 is observed to undergo a phase transformation in which the lattice parameters change significantly [49, 45]. The phase to which the host transforms has not been identified previously. Amatucci *et. al.* [45] have shown that Li_xCoO_2 can be completely and reversibly deintercalated to form CoO_2. They found that in the CoO_2 phase, the different O-Co-O slabs, held together by Van der Waals forces, are shuffled with respect to each other. The stacking sequence of the close-packed oxygen layers changes from the original ABCABC sequence of $LiCoO_2$ to an ABAB sequence.

In this chapter, we investigate phase stability in layered Li_xCoO_2 [118, 116]. We first consider relevant host structures that could reasonably be expected during a typical deintercalation/intercalation cycle. For each host structure, the enthalpies of a variety of ordered phases with different lithium-vacancy arrangements were calculated using the pseudopotential method within the local density approximation. These enthalpies were used to construct cluster expansions for the different host structures which were subsequently implemented in Monte Carlo simulations to obtain thermodynamic properties such as the equilibrium phase diagram.

4.2 Host Structures

The most stable phase at a particular lithium concentration will be the one with the lowest free energy at that concentration. To investigate phase stability of layered Li_xCoO_2 with lattice models, we must consider the set of host structures that are likely to be stable as a function of lithium concentration and temperature. Although, during lithium removal from and reinsertion into Li_xCoO_2, the material maintains its layered nature, the oxygen stacking sequence has been observed to change at low

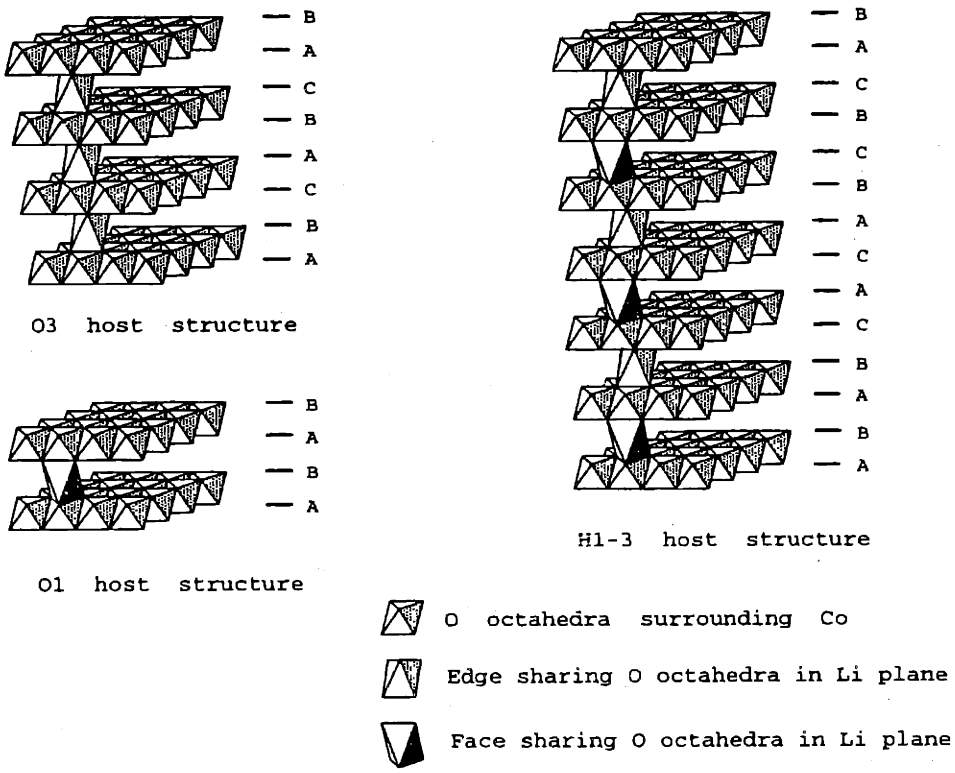

Figure 4-1: Schematic illustration of the three host structures O3, O1 and H1-3. The vertices of the octahedra correspond to oxygen ions. Uppercase letters describe the stacking sequence of the close-packed oxygen layers in each host. Representative octahedra surrounding lithium sites in lithium planes are also shown.

lithium concentration [45]. We, therefore, investigate the relative stability between three layered host structures that differ only in their oxygen stacking sequence. These are illustrated in Fig. 4-1. In this figure, the vertices of the octahedra schematically represent the oxygen sites that coordinate the Co ions at the center of the octahedra. The lithium ions reside in octahedral sites between the O-Co-O slabs. For each host, a representative oxygen octahedra surrounding a lithium site is drawn in Fig. 4-1.

The first host structure is the layered form of $LiCoO_2$, conventionally called O3 [44], which has an ABCABC oxygen stacking. This structure is observed to be stable experimentally for lithium concentrations between x=0.3 and 1.0 [50, 49, 45]. It is the same structure illustrated in Fig. 1-2(a) and described in chapter 1. The second host in Fig 4-1, referred to as O1, has an ABAB oxygen stacking. This structure is observed to be more stable than the O3 host when Li_xCoO_2 is completely deintercalated (*i.e.*

x=0) [45]. Experiment indicates that the stability of O1 seems to be restricted only to x=0 [45], suggesting that the lithium ions prefer the octahedral sites of the O3 host to those of the O1 host. In the O3 host, the oxygen octahedra surrounding the lithium sites share edges with the octahedra surrounding the cobalt sites, whereas in the O1 host, they share faces. The electrostatic repulsion between the Li and Co ions is, therefore, greater in the O1 phase. In fact a first principles LDA linear augmented plane wave (LAPW) calculation showed that the O1 form of lithiated $LiCoO_2$ is less stable than O3 by 150 meV per formula unit [119].

The experimentally observed [3, 34, 45] differences in the oxygen stacking of the host structures at x=0 and x=1 illustrates that the stable stacking sequence is sensitive to the lithium concentration. The lithium ions prefer the edge sharing octahedra of O3 to the face sharing octahedra of O1. On the other hand, in the absence of lithium, the O-Co-O sheets prefer the O1 stacking order to that of O3. Hence at x=0, O1 is stable and at x=1, O3 is stable. This is understandable in view of the results in chapter 3, which showed that the bonding among the ions of the CoO_2 host becomes more covalent as lithium is removed. Covalent bonding tends to stabilize O1 over O3 at the CoO_2 stoichiometric composition. At intermediate to low lithium concentrations, the situation is less clear. In this case, many vacancies will be present between the O-Co-O sheets, and a competition arises between the O1 stacking which minimizes the interaction energy between O-Co-O sheets around vacant patches in the lithium planes and the O3 stacking which minimizes the interaction energy between lithium and the host. One possibility is that a new host structure that embodies features of both O1 and O3 becomes more stable. A straightforward layered host of this form would be one in which the lithium ions selectively segregate to every other layer between O-Co-O sheets. This phenomenon is referred to as staging. The occupied lithium layers of the new host should have the environment of O3 while the unoccupied lithium layers should have the environment of O1. This hybrid structure is illustrated in Fig. 4-1 and can be obtained from O3 by shuffling the O-Co-O sheets adjacent to every other lithium plane in such a way that the shuffled planes have an environment identical to that in O1. In the resulting hybrid host, the lithium

ions reside only in the unshuffled planes with an O3 environment, while the shuffled planes are vacant. We refer to this hybrid host as H1-3 and its ideal stoichiometry is $Li_{1/2}CoO_2$ [118].

In addition to the experimentally identified O1 and O3 host structures, we also investigate whether the hybrid H1-3 host is thermodynamically stable with respect to O1 and O3 at intermediate lithium concentrations during deintercalation. As is the case for the O3 host, H1-3 has rhombohedral symmetry and belongs to the space group $R\bar{3}m$. In the triply primitive hexagonal unit cell setting, it has the same a lattice vector as O3 and a c lattice vector that is twice as large as that of O3. In view of the alternating distribution of lithium ions between the O-Co-O sheets, this hybrid host can be considered a stage II compound similar to that observed in graphite intercalation compounds [120]. Stage III, IV, etc. ordering in Li_xCoO_2 can also be expected. In a stage III compound for example, occupied lithium planes would be alternated by two vacant planes with a local O1 stacking between adjacent O-Co-O slabs. Such a phase we refer to as H11-3. Due to computational limitations, however, we restrict our study only to the stage II compounds, though it is possible that higher order staged compounds are thermodynamically stable.

4.3 Formation Enthalpies

The construction of a cluster expansion that reflects the configurational enthalpy of a system requires accurate first-principles total-energy calculations as input. In this work, we used the pseudopotential method within the local density approximation as implemented in the Vienna *ab initio* simulation package (VASP) to perform first-principles total energy calculations at constant pressure (see chapter 1).

We calculated the enthalpies of (i) 44 different Li-vacancy arrangements in the O3 host for concentrations ranging from x=0 to 1, including CoO_2 and $LiCoO_2$; (ii) five different Li-vacancy arrangements in the H1-3 host for concentrations ranging from x=0 to 1/2; and (iii) CoO_2 in the O1 host. We define the formation enthalpy for a

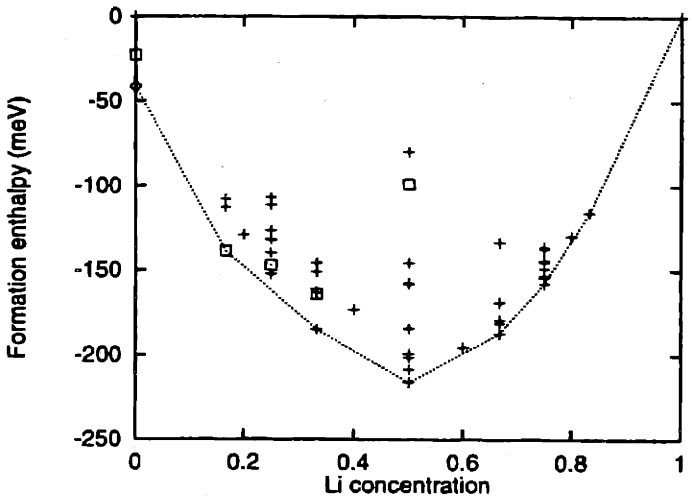

Figure 4-2: Formation enthalpies of layered Li_xCoO_2. Crosses are formation enthalpies for ordered lithium-vacancy arrangements in O3, squares are formation enthalpies for H1-3 structures and the diamond corresponds to the formation enthalpy of O1 CoO_2.

given Li-vacancy arrangement with concentration x in Li_xCoO_2 as

$$\Delta_f H = H - xH_{LiCoO_2} - (1-x)H_{CoO_2} \tag{4.1}$$

where H is the total enthalpy of the configuration per Li_xCoO_2 formula unit, H_{LiCoO_2} is the enthalpy of $LiCoO_2$ in the O3 host, and H_{CoO_2} is the enthalpy of CoO_2 in the O3 host. Formation enthalpies as opposed to total enthalpies more conveniently display relative stability between different phases. The formation enthalpy of a given structure Li_xCoO_2 as defined in (4.1) reflects the relative stability of that structure with respect to phase separation into a fraction x of $LiCoO_2$ and a fraction $(1-x)$ of CoO_2.

The formation enthalpies for Li_xCoO_2, illustrated in Fig. 4-2, are negative, indicating that Li_xCoO_2 is stable with respect to phase separation into a fraction x of Li_xCoO_2 and a fraction $(1-x)$ of CoO_2 within the O3 host. Hence for sufficiently low temperatures, we can expect that at any given lithium concentration x, the stable phase will either be a stoichiometric compound in which the lithium ions and vacancies are ordered on a superlattice, or a mixture of ordered stoichiometric compounds.

At higher temperature, these ordered compounds are expected to transform to the disordered state, assuming that the host on which the lithium ions order is still stable with respect to other host structures not considered. In Fig. 4-2, we have drawn the convex hull connecting the structures with the lowest formation enthalpies to indicate which of the structures are the most stable among those whose enthalpies were calculated with the pseudopotential method.

Several important features about Li_xCoO_2 can be deduced from the formation enthalpies of Fig. 4-2. Fig. 4-2 shows, in agreement with experiment, that at zero lithium concentration, the O1 host is more stable than the O3 host. The difference in enthalpy between O1 and O3 is 40 meV per CoO_2 formula unit. This result is in good agreement with a previous first-principles calculation using the LAPW method which found a value of 50 meV [119]. Approximately halfway between the formation enthalpies of O1 and O3 lies the formation enthalpy of the H1-3 host at x=0. This is a plausible result since every other empty plane between O-Co-O slabs in the H1-3 host has an O3 environment, while the remaining empty planes have an O1 environment. It implies that the interaction between adjacent O-Co-O slabs is fairly short ranged and that the enthalpy of H1-3 at x=0 could be approximated as the weighted average of the enthalpies of O1 and O3. In addition, the calculated equilibrium lattice parameter, c, of H1-3 (converted to the setting of the O3 host) is 12.23 $\AA$ which is roughly the average of the calculated value of c, for O3 of 12.39 $\AA$ and that for O1 (also converted to the setting of the O3 host) of 11.99 $\AA$. In Fig. 4-2, it can be seen that at x=1/6, the Li-vacancy arrangement in the H1-3 host lies on the convex hull. This structure is more stable than the two other Li-vacancy arrangements considered on the O3 host at that concentration. Furthermore, the fact that it lies on the convex hull means that it is more stable than a two-phase mixture (with overall Li concentration x=1/6) of any other ordered Li-vacancy arrangements. As will be shown in the next sections, this result indicates that the H1-3 host will appear as a stable phase in the phase diagram. Fig. 4-2 also indicates that there is a tendency for Li ordering within the O3 host at x=1/2.

Among the 44 different Li-vacancy configurations considered, the lowest-enthalpy

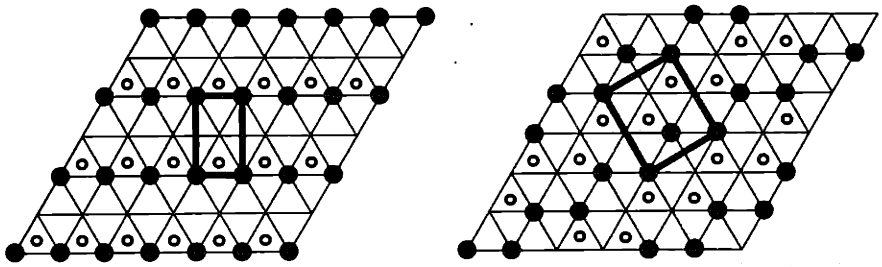

Figure 4-3: Two lithium-vacancy arrangements at x=1/2 in Li_xCoO_2 that have very low formation energies. The triangular lattice denotes the lithium sites within a Li plane of the O3 host. The filled circles correspond to Li ions ordered on the triangular lattice. A given in-plane ordered arrangement can be stacked in different ways among the different lithium planes. The empty circles indicate the projection along the c axis of the positions of the lithium ions in the adjacent lithium plane.

configuration at x=1/2 has an in-plane lithium ordering as illustrated in Fig. 4-3 (a). In this configuration, the lithium ions are ordered in rows separated by rows of vacancies. This in-plane Li ordering is the same as that proposed by Reimers and Dahn [50] based on their electrochemical and *in-situ* X-ray powder- diffraction measurements. They deduced this type of Li ordering by noticing that the (104) peak of the O3 host (which has rhombohedral symmetry) splits into two peaks with an intensity ratio of 1:2. Reimers and Dahn [50] argued that this splitting can be explained by assuming that the host changes from a rhombohedral to a monoclinic structure whereby the basal plane of the monoclinic structure (containing the a and b lattice vectors) is a two-dimensional supercell of the basal plane of the rhombohedral O3 host in the hexagonal setting. This is illustrated in Fig 4-3(a). This still leaves several crystallographically distinct ways to stack in plane Li-vacancy arrangements along the c direction. Fig. 4-3(a) also indicates the stacking with the lowest enthalpy. This is illustrated by projecting the Li-vacancy ordering in two adjacent Li planes along a direction perpendicular to the Li planes.

Almost degenerate, but slightly higher in enthalpy with the Li-vacancy ordering of Fig. 4-3(a) is another structure with the arrangement as illustrated in Fig. 4-3(b). In this configuration, the Li ions are ordered in a zigzag arrangement. The pseudopotential calculations predict that the formation enthalpy of this structure is

approximately 1 meV per formula unit higher than that of Fig. 4-3(a). This difference in enthalpy is too small to be resolved with currently available numerical methods. Therefore, we cannot unequivocally deduce from our first principles calculations which of the two Li-vacancy configurations is the ground state. Nevertheless, the calculated powder diffraction pattern of the configuration of Fig. 4-3(a) exhibits the (104) peak splitting observed experimentally while the diffraction pattern of the configuration of Fig. 4-3(b) does not exhibit this peak splitting. This suggests that the structure of Fig. 4-3(a) is indeed the stable phase at x=1/2.

4.4 Cluster Expansion and Monte Carlo simulations

To study phase stability at finite temperature, we need to construct a separate cluster expansion of the formation enthalpy for each different host structure. We did not construct a cluster expansion for the O1 host since, as described in section 4.2, it is stable only at very dilute Li concentrations. In our calculations of the Li_xCoO_2 phase diagram, O1 was therefore treated as a line compound at x=0 and its free energy was set equal to its enthalpy.

A cluster expansion for the O3 host structure was constructed by applying an inversion method based on linear programming techniques [80] to the formation enthalpies of 36 of the 44 different Li-vacancy configurations within the O3 host plotted in Fig. 4-2. The resulting cluster expansion contains 19 terms, including 12 pairs and 5 triplets. These clusters are illustrated in Fig. 4-4. The values of the ECI are plotted in Fig. 4-5(a). The ECI of Figs. 4-4 and 4-5 correspond to clusters that connect sites within the same Li plane and sites between adjacent Li planes. The root-mean-square (rms) difference between the 36 formation enthalpy values used in the inversion method and the corresponding values as calculated with the cluster expansion is less than 5 meV. For the remaining eight Li-vacancy configurations not included in the inversion, the rms difference between their enthalpies as calculated

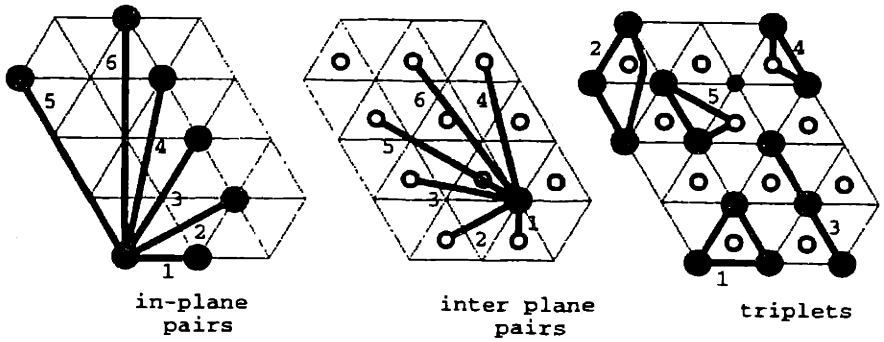

Figure 4-4: Clusters used in the cluster expansions. The triangular lattice denotes the Li sites within a single lithium plane, while the empty circles denote the projection of the lithium sites of an adjacent plane.

with the pseudopotential method and as predicted by the cluster expansion is 8 meV. As can be seen from Fig. 4-4, the values of the ECI converge to zero as the number of sites or the separation between the sites in the cluster increases. The ECI corresponding to the first nearest neighbor in plane pair cluster is the largest, its value being at least three times larger than the other ECI.

As was pointed out in the previous section, the formation enthalpies of the experimentally observed Li-vacancy ground state ordering (Fig. 4-3(a)) at x=1/2 is practically degenerate with that of the configuration of Fig. 4-3(b). The cluster expansion for the O3 host predicts that the ground-state configuration of Fig. 4-3(a) is more stable than the configuration of Fig. 4-3(b) by 5 meV. Although this difference is slightly larger than the difference calculated with the pseudopotential method, it is still smaller than the minimum numerical error expected from the pseudopotential method.

A second cluster expansion was constructed for the H1-3 host. This cluster expansion contains five terms. It was obtained by fitting the ECI to the formation enthalpies of the five different Li-vacancy configurations within H1-3 plotted in Fig. 4-2. The ECI of this cluster expansion correspond to clusters within the same Li plane. Their values are illustrated in Fig. 4-5(b). Since occupied Li planes in the H1-3 host are further apart than in the O3 host, ECI corresponding to clusters connecting different Li planes have been neglected.

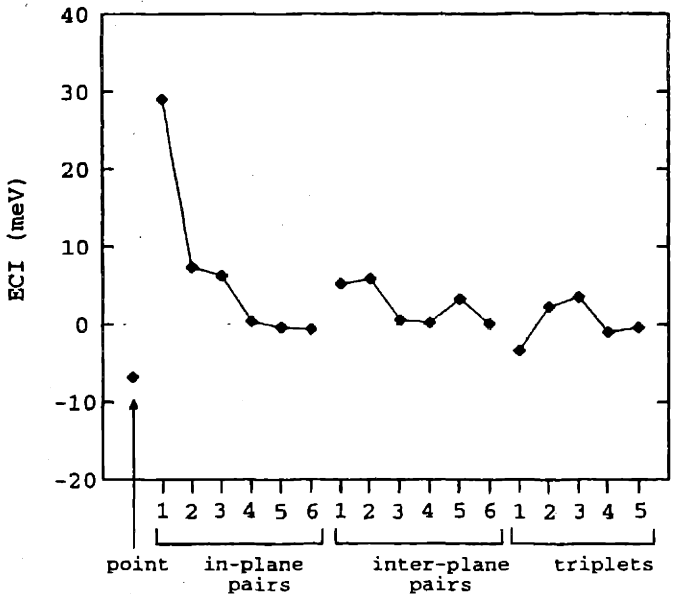

(a)

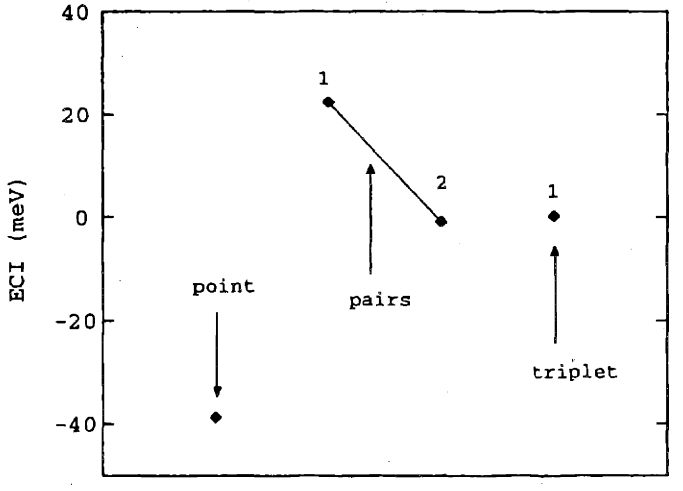

(b)

Figure 4-5: Values of the ECI for (a) the O3 host and (b) the H1-3 host. Refer to Fig. 4-4 for an identification of the cluster corresponding to each effective cluster interaction.

Both cluster expansions of the formation enthalpy of the O3 and H1-3 hosts were implemented in Monte Carlo simulations in the grand canonical ensemble. To study the thermodynamics of Li and vacancy ordering in the O3 host, we used a Monte Carlo cell containing 3888 unit cells where each primitive unit cell corresponds to a Li_xCoO_2 formula unit. For the H1-3 host, Monte Carlo simulations were performed on a two-dimensional lattice, since the cluster expansion for this host only has ECI corresponding to clusters within the occupied Li planes. The Monte Carlo cell for the H1-3 host contained 900 primitive unit cells. At each temperature and chemical potential, 2000 Monte Carlo passes per lattice site were performed after which sampling occurred over 4000 Monte Carlo passes. To investigate the relative stability between the O1 host, the O3 host and the H1-3 host, we calculated the free energies of the latter two host structures as a function of Li concentration. These free energies were calculated by integrating the chemical potential obtained from the Monte Carlo simulations. The integration bounds were from zero Li concentration (where the free energy equals the ground state enthalpy) to the desired concentration x.

For both the O3 and the H1-3 host structures, we also cluster expanded the lattice parameter, c, of the different Li-vacancy configurations. For each Li-vacancy configuration, the equilibrium lattice parameters were converted to the hexagonal setting of the O3 host. For both host structures, the cluster expansions of c contained the same clusters as used in the cluster expansion of the formation enthalpies. The root-mean-square difference between the with the pseudopotential optimized values for c and those as calculated with the cluster expansion is 0.5 % of the average value of c for the O3 host. These cluster expansions were used to determine the equilibrium lattice parameter as a function of Li concentration.

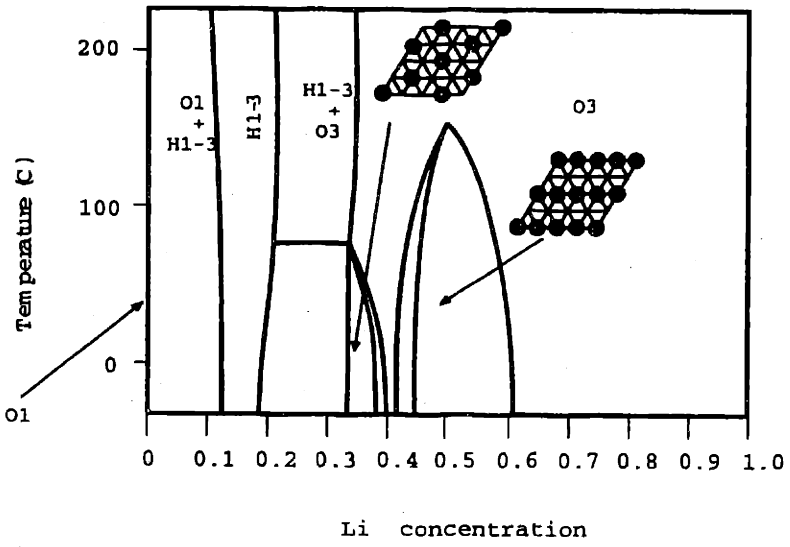

Figure 4-6: The calculated Li_xCoO_2 phase diagram. The insets show the in-plane lithium ordering predicted to be stable at x=1/3 and 1/3.

4.5 Calculated Thermodynamic Properties

4.5.1 Phase diagram

The calculated equilibrium phase diagram of Li_xCoO_2 is illustrated in Fig. 4-6. As can be seen from Fig. 4-6, O3 is predicted to be the most stable of the three hosts considered from intermediate to high lithium concentration. Within O3, the Li ions are predicted to order both at x=1/2 and x=1/3. At x=1/2, the lithium ions order in rows alternated by rows of vacancies. The stacking sequence of the in-plane ordered Li arrangement is illustrated in Fig. 4-6. At x=1/3, the Li ions order in an arrangement in which they are spaced as far apart as possible from each other. This ordered arrangement is illustrated in the inset in Fig. 4-6. At x=1/2, the order-disorder transition temperature is predicted to be around 160° C while at x=1/3, it is predicted to be approximately 80° C. Around x=0.15, H1-3 is found to be more stable than both O3 and O1. As is evident from the large two phase field separating the stability regions of O3 and H1-3 in Fig. 4-6, O3 transforms to H1-3 according to a first order transition. In-plane lithium ordering in the occupied planes of H1-3 is predicted at x=1/6. The ordered Li-vacancy arrangement is the same as that predicted at x=1/3

in the O3 host and illustrated in the inset of Fig. 4-6. The ordered Li arrangement within the H1-3 host is calculated to disorder at 130° C through a second order phase transition. However, since the cluster expansion for the H1-3 host only contains 5 terms and was constructed by fitting to only five enthalpy values the quantitative accuracy of this order-disorder transition temperature is questionable. For this reason, we have omitted the order-disorder transition within the H1-3 host from the phase diagram of Fig. 4-6. Finally, at x=0, O1 is found to be the most stable phase.

Overall, the agreement of the calculated phase diagram with experiment is good. The relative stability between O3 and O1 as a function of Li concentration agrees with experiment. Furthermore, the lithium ordering at x=1/2 agrees qualitatively with the observations of Reimers and Dahn [50] who gave convincing evidence for Li ordering at that concentration and found the ordered phase to be stable below 60° C. Note in Fig. 4-6, that the predicted order-disorder transition temperature is too high by approximately 100°. Over predictions of this order of magnitude are not uncommon in first principles phase diagram calculations. In view of this over-prediction, it is probable that the ordered phase predicted at x=1/3 will disorder in reality below room temperature explaining why it has not been observed experimentally.

The H1-3 host, as described above can be considered a stage II compound in that lithium is assumed to exclusively occupy alternating lithium planes (*i.e.* those planes with an O3 local environment). The prediction that H1-3 is stable at low Li concentration is consistent with experimental observations that the O3 host transforms to a new structure as it is deintercalated to around x=0.2. Calculated X-ray diffraction patterns of the H1-3 phase agree qualitatively with those measured *in-situ* around x=0.2 [118, 45]. Furthermore, a recent refinement of the X-ray diffraction pattern of Li_xCoO_2 at low lithium concentration has given strong evidence that the H1-3 phase (or possibly the stage III, H11-3 compound) appears in that concentration range [121].

One major disagreement between experiment and the calculated phase diagram is that a two phase region at high lithium concentration is not predicted. Between x=0.75 and 0.95, two O3 phases differing only in their lattice parameters and lithium concentration coexist [50, 49, 45, 10]. As noted in the introduction, this two phase

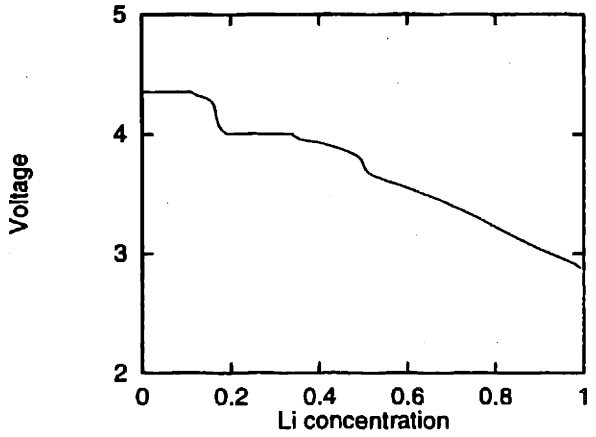

Figure 4-7: Calculated voltage curve of Li_xCoO_2 at 30°C

region cloaks a metal-insulator transition in that above x=0.95, Li_xCoO_2 is a semiconductor while below x=0.75, it is a metal. In the next section, we describe how a metal-insulator transition can simultaneously induce a first order structural phase transition of the host. We point out here, though, that experimental evidence exists exposing the causal link between the metal-insulator transition and the structural phase transition between x=0.75 and 0.95 in Li_xCoO_2. Tukamoto and West [122] found that fully lithiated $LiCoO_2$ can be made metallic without inducing any structural changes to the host by substituting a dilute fraction of Co^{3+} ions by Mg^{2+} ions. In parallel with this, they found that in the Mg doped samples, the two phase region at high Li concentration is absent [122].

4.5.2 Voltage curve

An important property for lithium transition metal oxides is the evolution of the voltage intercalation curve as a function of Li concentration. The voltage curve is related to the chemical potential according to (2.1) in chapter 2. Fig. 4-7 illustrates the voltage curve of layered Li_xCoO_2 as a function of x. The curve was calculated with Monte Carlo simulations using the cluster expansion of Fig. 4-5. Features in the voltage curve reflect the phase transformations predicted in the phase diagram of Fig. 4-6. The small steps at x=1/2 and x=1/3 are a result of the ordered phases shown in Fig. 4-6. The large step around x=0.15 is a result of the occurrence of the

H1-3 phase predicted to be stable at low x.

Experimentally, the voltage curve of layered Li_xCoO_2 exhibits a plateau between x=0.75 and 0.95 as a result of the two phase coexistence region [50, 49, 45]. This plateau is absent in the calculated voltage curve since the two phase region at high x is not predicted by the cluster expansion derived from LDA enthalpies. The step around x=1/2 in the calculated voltage curve due to lithium ordering is similar to that observed experimentally at the same composition [50]. The step in the calculated voltage curve as a result of the H1-3 phase is larger than that observed experimentally [45]. This is in part because in actual Li_xCoO_2 particles, strain energy builds up upon transforming from O3 to H1-3 (see section 4.6.1), which will destabilize H1-3 relative to O3 and O1 and hence result in a reduction of the step associated with H1-3. Typically, calculated average voltages are around 0.25 to 0.5 volt below the experimental quantities [114, 123, 124, 125, 119, 126, 127]. It is not surprising, therefore, that the calculated voltage intercalation curve for Li_xCoO_2 is systematically underestimated at all x.

4.5.3 The Lattice parameter c

Fig. 4-8 compares the calculated value for c with that determined from *in-situ* X-ray diffraction measurements of Li_xCoO_2 [45]. c was calculated in the Monte Carlo simulations using the cluster expansions of c for the O3 and H1-3 hosts. Since the calculated order-disorder transition temperatures of the ordered phases at x=1/2 and 1/3 within O3 are over predicted, we calculated c at 130^o C (calculation temperature). This temperature is between the order-disorder transition temperatures of the x=1/2 phase and the x=1/3 phase and properties calculated at this temperature will be most representative of those measured experimentally at room temperature. We have plotted values of c for both the O3 and H1-3 hosts over the range of Li concentrations for which these hosts can exist. Values of c are therefore also plotted for Li concentrations at which the hosts are predicted to be metastable. This enables us to more clearly observe trends.

The calculated values of c for the O3 host is systematically under predicted by

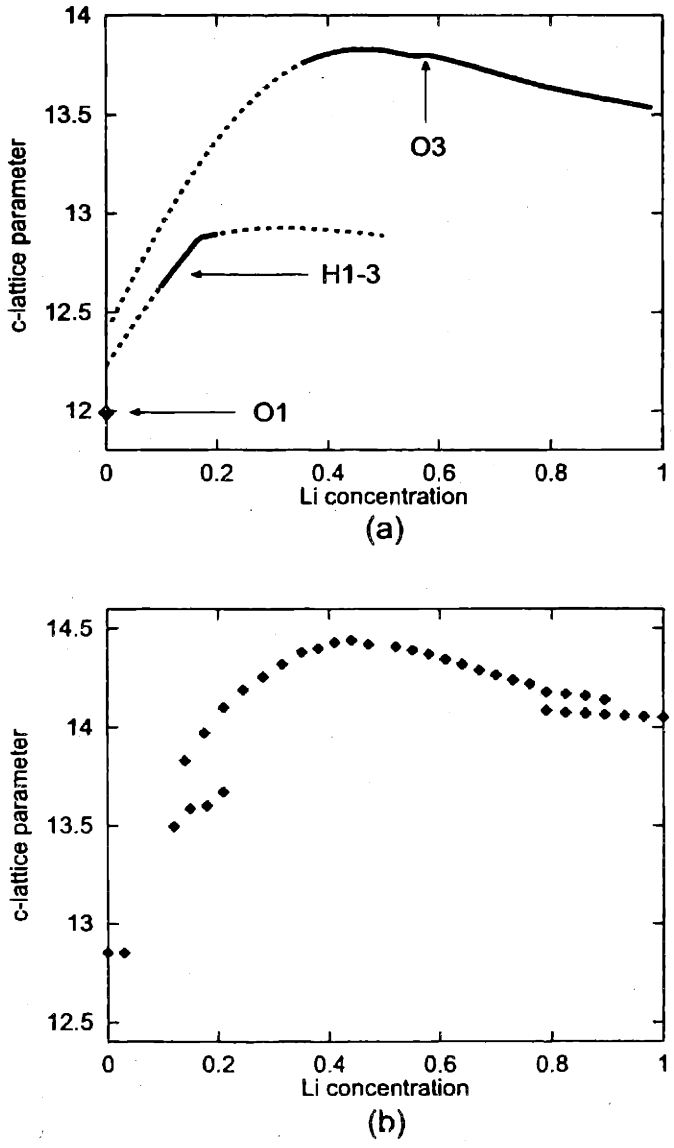

Figure 4-8: Comparison between (a) calculated and (b) experimental (taken from Ref. [45]) lattice parameter, c as a function of Li concentration. The calculated lattice parameters are also illustrated in the regions where the O3 and H1-3 hosts are metastable (dashed lines).

approximately 4%. An under prediction in lattice parameters is typical of LDA, though a value of 4% is uncharacteristically large. It suggests that the electrons in this system are highly correlated [128].

The qualitative variation of the calculated lattice parameter, c, agrees well with experiment. As Li is removed from the O3 host, c is more or less constant between x=0.5 and 1, exhibiting only a slight maximum around x=0.5. Below x=0.5, the lattice parameter decreases dramatically as the Li concentration is reduced. Part of the significant contraction of the O3 form of Li_xCoO_2 upon deintercalation can be attributed to a reduction in the number of lithium ions between the O-Co-O sheets. Another significant factor contributing to the contraction of the host is the change with x in electronic properties of Li_xCoO_2. As described in chapter 3, removal of lithium causes the cobalt-oxygen bonds to become more covalent. This results in a contraction of the cobalt-oxygen distances and, therefore, a reduction in width of the O-Co-O slabs as x is decreased. Furthermore, the increased covalency is accompanied by a reduction in the polarization of negative charge toward the oxygen ions. Hence the electrostatic repulsion between negatively charged oxygen ions of adjacent O-Co-O slabs diminishes as lithium is removed from the host.

Fig. 4-8(b) also shows that the lattice parameter, c, of the host drops abruptly upon transforming from O3 to H1-3. A similar drop in c is observed experimentally, giving further credibility to the prediction of staging at low lithium concentration. The abrupt reduction in c is a direct result of the staging process since the distance across the empty planes of H1-3 is smaller than the occupied planes.

4.6 Driving forces for phase transformations

4.6.1 The staging transformation

As noted above, the H1-3 host structure can be viewed as a staged compound in that Li only occupies every other open layer between O-Co-O sheets. Staging occurs in many layered intercalation compounds [120] and transition metal dichalcogenides

[129]. The predicted transformation from the O3 host to the H1-3 host in Li_xCoO_2 is similar to that observed in graphite in which the host undergoes small structural changes simultaneously with the staging transformation. In graphite [120], the two dimensional honeycomb sheets of carbon are stacked according to an ABAB sequence. When the guest ion uniformly intercalates between these sheets, the stacking sequence changes to AAA. At low concentrations, the guest ions selectively segregate to a subset of the open galleries between graphite sheets. The sheets surrounding occupied galleries have an AA stacking just as in the fully intercalated form of graphite whereas the sheets surrounding unoccupied galleries have an AB stacking just as in pure graphite. The results of this chapter indicate that the same phenomenon is occurring in Li_xCoO_2 at low lithium concentration. The stacking sequence of the O-Co-O sheets in the fully intercalated form of Li_xCoO_2 (stable in the O3 structure) is different from that of the completely deintercalated form (which is stable in the O1 structure). At some intermediate Li concentration (*i.e.* around x=0.15), the Li tends to segregate to a subset of the open layers between O-Co-O sheets. In this intermediate compound (*i.e.* the H1-3 host), the O-Co-O sheets surrounding the occupied Li layers are stacked as in the stable form of Li_xCoO_2, and the sheets adjacent to empty Li layers are stacked as in the stable form of CoO_2. Hence a hybrid host structure exhibiting structural features of the stable end members $LiCoO_2$ and CoO_2 is stable at these Li concentrations.

The reason for the occurrence of staging in Li_xCoO_2 can be inferred from the shapes of the free energy curves of Fig. 4-9. At dilute Li concentrations, the interactions of the Li ions with each other and with the host are similar in both O3 and H1-3. Therefore, the free energies of these two hosts at low Li concentration are more or less parallel with Li concentration as is illustrated in Fig. 4-9. At x=0, however, H1-3 has an added stability compared to O3 since H1-3 has alternating Li planes with local O1 environment. In the absence of Li ions, the O1 stacking sequence is favored. Consequently, H1-3 remains more stable than O3 for as long as the free energy curves of these hosts remain parallel with increasing x. As the lithium concentration is increased, however, the Li planes of H1-3 saturate sooner than in O3 because it

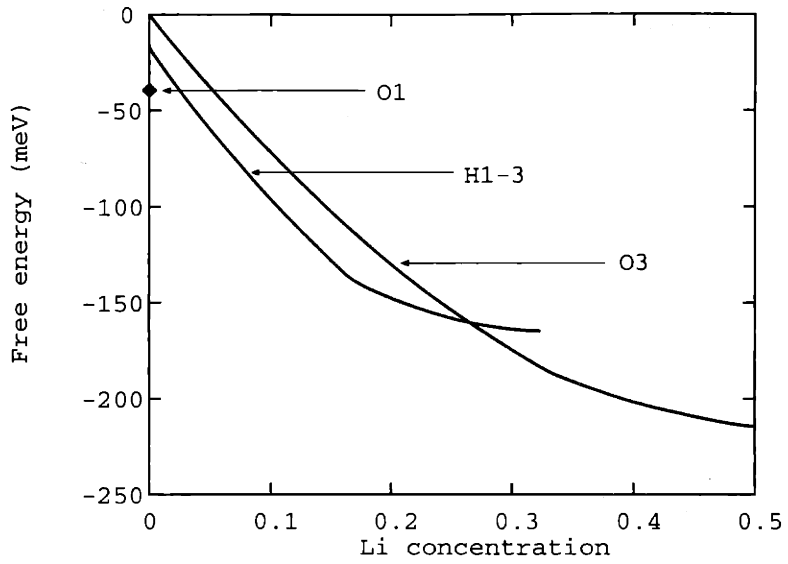

Figure 4-9: The free energies at 30°C of O3 and H1-3 as a function of lithium concentration. Also illustrated is the energy of CoO_2 in the O1 host.

has only half the available Li planes. This causes the free energy of H1-3 to increase faster with Li concentration than in O3, rendering the latter phase more stable above a critical lithium concentration.

From a kinetic point of view, it is unlikely that perfect staging will occur within a single grain since this would require that lithium is evenly removed from every other plane. Instead, as was suggested for graphite intercalation compounds by Daumas and Herold [130], staging will likely occur in domains as illustrated schematically in Fig. 4-10. This would result in a situation in which the average concentration in

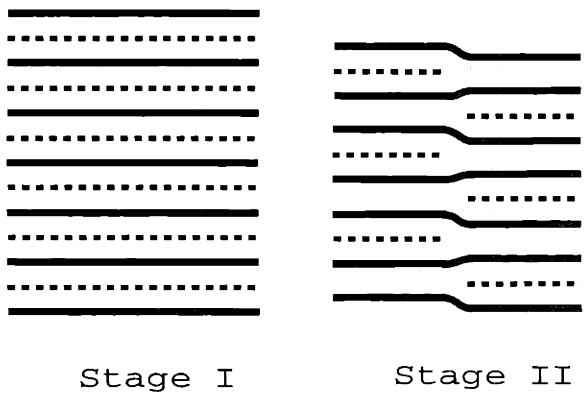

Figure 4-10: Staging according to the model of Daumas and Herold. Thick lines correspond to O-Co-O slabs, dotted lines correspond to occupied lithium planes.

each lithium plane is the same throughout the grain, however, locally the Li ions are segregated to form domains that are staged. Although this type of staging on a local level is kinetically more likely, it does have its thermodynamic costs. Since the stacking sequence of O-Co-O slabs across empty planes is different from that across occupied lithium planes in H1-3, the stacking sequence would have to change at the boundaries of the domains within the same lithium plane. This will be accompanied by elastic strain energy and possibly even plastic energy (in the form of dislocation creation) which will raise the free energy of the staged compound. Hence the stability of the staged phase with respect to the O3 and O1 hosts in actual crystals will be reduced and the measured stability region of the H1-3 will be narrower than predicted in Fig. 4-6.

4.6.2 Metal-insulator transition and the two phase region

The electronic properties of Li_xCoO_2 change dramatically upon crossing the metal-insulator transition at high lithium concentration. As was described in chapter 3, $LiCoO_2$ is a semiconductor with fully occupied t_{2g} bands. Li removal from $LiCoO_2$ simultaneously introduces an equivalent number of holes in the t_{2g} bands. In a simple band structure picture in which electrons are assumed to be delocalized, this implies that $LiCoO_2$ should become metallic once lithium is removed. Experimentally though, Li_xCoO_2 remains a semiconductor at least untill x=0.95 [9, 10]. In insulating transition metal oxides, holes in the valence bands are usually localized in space. This picture has recently been confirmed experimentally for Li_xCoO_2 by Menetrier *et. al.* [10]. While it is well recognized that changes from localized to delocalized electrons affect the transport properties, it can also have a significant effect on the thermodynamic potentials. Localized holes contribute to the free energy of the solid an additional configurational entropy associated with the different ways of distributing the holes throughout the crystal. This entropy is an order of magnitude larger than the electronic entropy associated with delocalized holes in narrow valence bands. Also there is first principles evidence that the energetics of localized holes versus delocalized holes can be significantly different. This was for example illustrated by first

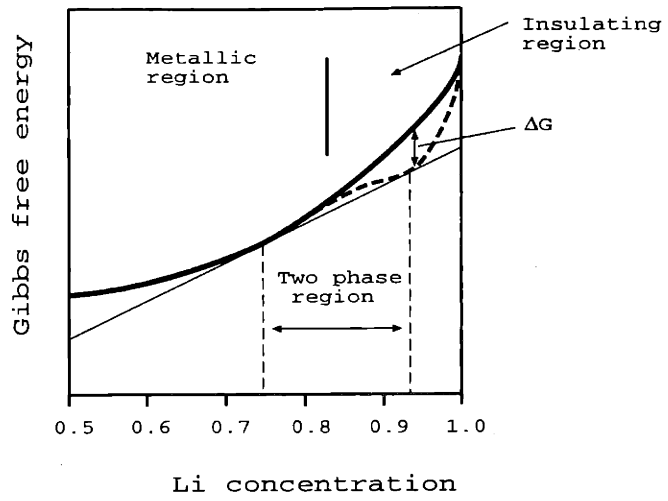

Figure 4-11: Free energy in the vicinity of the metal-insulator transition. The vertical line schematically denotes the lithium concentration at which the host crosses over from an insulator to a metal. ΔG refers to the additional free energy arising from the localized holes in the insulating regime.

principles investigations within the Hartree Fock approximation on Li doped NiO, which showed that there can be a large enthalpy gain when an electron hole goes from a delocalized state to a localized state [131].

Such changes in thermodynamic properties upon crossing the metal-insulator transition can induce non-convexity in the free energy curve of the host material and hence a first order transition. The possible effect of a metal- insulator transition on the free energy of the host is illustrated in Fig. 4-11. The solid curve corresponds to the calculated free energy of Li_xCoO_2 using the cluster expansion of section 4.4. This free energy curve neglects the role of localized holes for the insulating concentrations. The solid free energy curve is characteristic of complete solid solution over the concentration range shown. If the intercalation compound undergoes a metal-insulator transition (schematically at a concentration denoted by the vertical line in Fig. 4-11) the additional configurational entropy (and possible enthalpy lowering effect) arising from the localized holes in the insulating phase, will lower its free energy as is schematically illustrated by the dashed curve. Less change is expected for the metallic state by including electron correlation as there is no localization enthalpy for the holes and only a small electronic entropy. If the free energy contributions of the localized

holes on the insulating side are large enough to break the convexity (*i.e.* the dashed curve) of the initial free energy curve (solid curve) in Fig. 4-11, a two phase region would arise with the phase boundaries determined by the common tangent.

The measurements by Tukamoto and West [122] with Mg doped $LiCoO_2$ support the above mechanism explaining how a metal-insulator transition can induce a first-order structural phase transition. By substituting Co^{3+} ions with Mg^{2+} ions, holes are created in the t_{2g} bands of the fully lithiated compound since Mg is only able to donate 2 electrons to the host as opposed to 3. The effect of Mg doping on the electronic properties of $LiCoO_2$ is similar to lithium removal from the host. Mg doping therefore shifts the metal-insulator transition to higher lithium concentration. This in turn causes a reduction in stability of the semiconducting phase of $Li_xCo_yMg_{1-y}O_2$ for x above the metal-insulator transition of the doped compound. For a critical Mg concentration, the fully lithiated form $LiCo_yMg_{1-y}O_2$ is metallic and the two phase region then disappears completely. This was observed electrochemically by Tukamoto and West [122]. They found that as the Mg concentration is increased, the plateau in the voltage curve signifying the two phase region decreases and completely disappears when the Mg concentration exceeds approximately 8 percent.

4.7 Conclusion

In this chapter we have investigated phase stability of layered Li_xCoO_2 from first principles. We have compared the relative stability between three different host structures, namely O3, O1 and a stage II compound that is a hybrid between O3 and O1 and which we have denoted as H1-3. In agreement with experiment, the calculations predict that O3 is stable at intermediate to high lithium concentration and that O1 is stable when the compound is fully deintercalated. The calculations also predict that H1-3 is stable at low lithium concentration. This prediction sheds light on the as of yet uncharacterized phase transformation observed experimentally at low lithium concentration. Although in our calculations, we have considered only a stage II compound in addition to O1 and O3, in reality, it is possible that stage III

(H11-3) and even stage IV (H111-3) forms of Li_xCoO_2 may be stable at low lithium concentration. The qualitative evolution of the calculated lattice parameter, c, agrees well with that observed experimentally. We have argued that the large drop in c with decreasing x is in part caused by the shift in the nature of bonding between cobalt and oxygen from an ionic character to a covalent character.

At high lithium concentration, our calculations have demonstrated that the large two phase region between two crystallographically identical forms of O3 with concentrations x=0.75 and 0.95 is not a result of lithium ordering. Instead using thermodynamic considerations, we have argued that this first-order phase transformation with x is driven by a metal-insulator transition that occurs between x=0.75 and 0.95. To our knowledge, this is the first recognition that a metal-insulator transition caused by variations in concentration can induce a first-order structural phase transformation. We expect this phenomenon to be common in other oxides exhibiting metal-insulator transitions with concentration, yet, we expect sluggish kinetics to inhibit the first-order structural transformation from occurring on most reasonable time scales. The difference between Li_xCoO_2 and other oxides exhibiting a metal-insulator transition with concentration such as $La_xSr_{1-x}CoO_3$ [132, 133] is that the lithium ions in Li_xCoO_2 have a fast mobility that enables the first-order phase transformation to be kinetically realized.

The main limitations of layered Li_xCoO_2 in a lithium battery, is that it has poor cycling properties when x is decreased much below 0.5. This is in large part due to the numerous phase transformations that occur below x=0.5 and the dramatic decrease of the lattice parameter, c, of the host as x approaches zero. The phase transformations from O3 to H1-3 and from H1-3 to O1, all involve the gliding of adjacent O-Co-O sheets with respect to each other, which can cause severe damage to the macroscopic Li_xCoO_2 particles. Improvements in the cycling properties of Li_xCoO_2 will therefore require a suppression of these phase transformations. One possibility is to find dopants that reside in the lithium planes and prevent the O-Co-O slabs from gliding with respect to each other at low x. Suppression of the large drop in the parameter, c, of the O3 form of Li_xCoO_2 at low x (see Fig. 4-8) could

occur to a certain extent by replacing some cobalt with metal cations that reduce the degree with which the metal-oxygen bond becomes covalent with decreasing x.

Chapter 5

Phase diagram of spinel Li_xCoO_2

5.1 Introduction

Although $LiCoO_2$ is commonly synthesized with the layered crystal structure, low temperature synthesis routes have produced a form of $LiCoO_2$ exhibiting cubic symmetry [39, 40, 41, 42]. Controversy still exists about the exact nature of its crystal structure yet much evidence suggests that low temperature (LT) $LiCoO_2$ has a modified spinel structure [39, 40]. While the actual material is likely to contain defects, the ideal crystal structure has an ABCABC stacking sequence of close-packed oxygen planes with Co residing in a subset of the octahedral sites. For stoichiometric LT $LiCoO_2$, the Li ions reside in octahedral sites. LT $LiCoO_2$ has poor electrochemical properties, and is at present of little practical use. Nevertheless, since it has the same crystal structure as spinel $Li_yMn_2O_4$ (with $y = 2 \times x$), an important candidate cathode material for lithium batteries [4, 5, 23, 11], a first principles investigation of the thermodynamic properties of the former compound can yield important insights about the properties of the latter compound.

$Li_yMn_2O_4$ differs from many other transition metal oxide intercalation compounds in that a range of electronic phenomena play a significant role in determining its thermodynamic and structural properties: Jahn-Teller distortions [4, 5, 11, 12], charge ordering [134, 135] and magnetic ordering [13] have each been identified as producing measurable imprints on electrochemical characteristics. The presence of numerous

electronic phenomena can cloak the true microscopic origins of different phase transformations. Although layered Li_xCoO_2 undergoes a metal-insulator transition, phenomena such as Jahn-Teller distortions and magnetic ordering are either absent or insignificant in affecting phase transformations in Li_xCoO_2. A study of phase stability in spinel Li_xCoO_2 will, therefore, enable a decoupling of the roles that electronic phenomena (associated with a particular transition metal) and structural effects (resulting from the symmetry of the metal oxide host) have on the phase transformations observed in spinel compounds. The results of the present chapter will show that most of the phase transformations observed in spinel $Li_yMn_2O_4$ are determined by the host structure and only quantitatively affected by electronic phenomena [136]. (The same conclusion was drawn by a first principles investigation of spinel $Li_yMn_2O_4$ in which Jahn-Teller distortions, charge ordering and the temperature dependence of magnetic ordering were neglected [137].)

The spinel crystal structure differs from the layered crystal structure in several significant ways. In spinel Li_xCoO_2, Li can reside in both tetrahedral and octahedral sites while in the layered phase Li only occupies octahedral sites. The effect of this is that layered and spinel Li_xCoO_2 have topologically very different phase diagrams. Another difference between the two hosts is that their respective symmetry puts different constraints on how the ions of the host can relax. This affects a change in the relative stability between the two crystal structures as the lithium concentration is varied [126].

In this chapter, we investigate the phase diagram and electrochemical properties of spinel Li_xCoO_2. We use the same methodology as was used to investigate the layered form of Li_xCoO_2.

5.2 Formation enthalpies and cluster expansion

The spinel form of Li_xCoO_2 which belongs to the $Fd\bar{3}m$ space group has two crystallographically distinct sites which the Li ions can occupy: the tetrahedrally coordinated (by oxygen) 8a sites and the octahedrally coordinated 16c sites. The sublattice com-

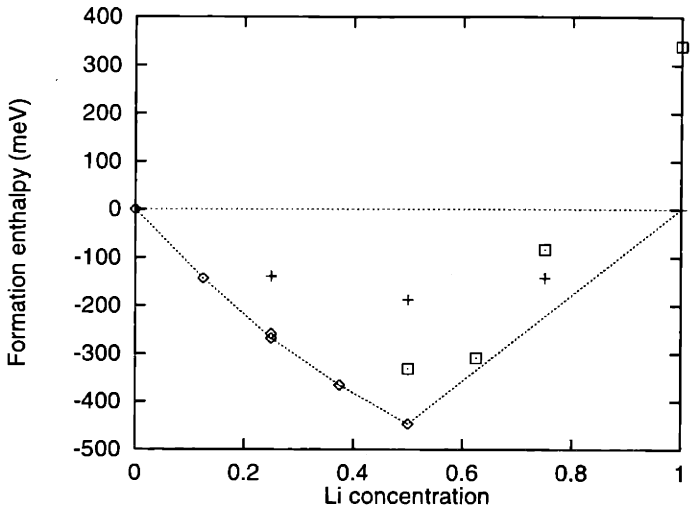

Figure 5-1: Formation enthalpies for different ordered structures in spinel Li_xCoO_2. The diamonds refer to structures in which the lithium ions occupy only tetrahedral sites, the crosses correspond to structures in which lithium ions occupy only octahedral sites and the squares correspond to structures in which the lithium ions occupy both octahedral and tetrahedral sites.

prising the 8a sites is topologically equivalent to the diamond crystal structure. The 16c sites reside in the middle of pathways connecting nearest neighbor 8a sites. Each 8a site, therefore, has four nearest neighbor 16c sites while each 16c site has two nearest neighbor 8a sites. To study the thermodynamics of this host, we constructed a cluster expansion that describes the configurational enthalpy of distributing lithium and vacancies over the collection of 8a and 16c sites. The ECI of the cluster expansion were fitted to the enthalpy values of 17 different Li-vacancy arrangements in the cubic host. We used an inversion method based on linear programming techniques [80]. The enthalpies of the 17 different Li-vacancy configurations were calculated with the pseudopotential method [99] in the local density approximation (LDA) (non-spin polarized) as implemented in VASP [54, 107]. Ultra-soft pseudopotentials [53] were used. For each structure, the cell parameters and the ionic positions were fully relaxed.

Fig. 5-1 shows the formation enthalpies of 14 of the 17 structures used in the fit (3 of the structures have a concentration greater than 1). The formation enthalpies are defined by (4.1) of chapter 4. H_{CoO_2} used in (4.1) to calculate the formation enthalpies of Fig. 5-1 corresponds to the enthalpy of the fully delithiated spinel host and H_{LiCoO_2}

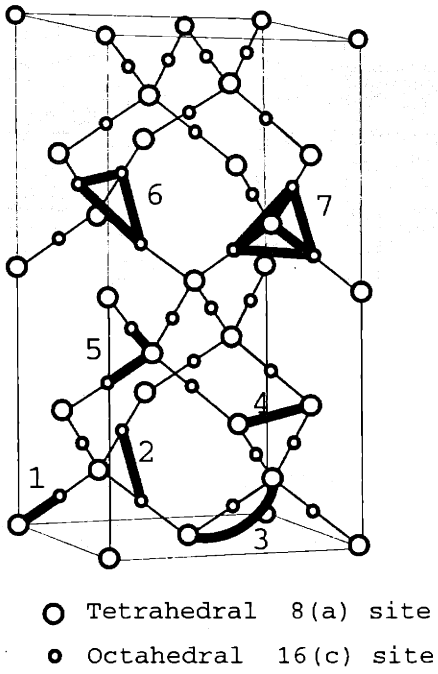

Figure 5-2: Illustration of the clusters (connected by dark lines) used in the cluster expansion for spinel Li_xCoO_2. Shown are tetrahedral 8a and octahedral 16c sites. The positions of the Co and O ions are not shown. The numbering next to each cluster refers to the ECI in table 1.

correspond to the enthalpy of spinel $LiCoO_2$ with all the lithium ions in the octahedral 16c sites. Among the 14 structures of Fig. 5-1 are configurations in which Li ions occupy only octahedral sites (crosses), tetrahedral sites (diamonds) and configurations in which both tetrahedral and octahedral sites are occupied simultaneously by Li ions (squares). We have also drawn the convex hull connecting the structures with the lowest formation enthalpies to indicate the most stable structures among those considered with the pseudopotential method.

The cluster expansion determined by fitting to these enthalpies contains 10 terms (table 1). This includes ECI corresponding to the empty cluster V_o, two point clusters (tetrahedral and octahedral sites), four pair clusters and three multi-body clusters. One type of pair cluster is between nearest neighbor octahedral and tetrahedral sites. The other pair clusters correspond to the nearest and second nearest neighbor pairs on the sublattice formed by the tetrahedral 8a sites and the nearest neighbor pair on the sublattice formed by the octahedral 16c sites. The root mean square difference

Clusters	ECI (meV)
Empty cluster	166.9
Tetrahedral point cluster	168.6
Octahedral point cluster	174.1
1	86.5
2	29.1
3	6.3
4	0.3
5	17.3
6	8.8
7	9.4

Table 5.1: Values of the ECI for the spinel cluster expansion. The numbering in the first column refers to the clusters in Fig. 5-2. The second column are the numerical values of the ECI (meV).

between the cluster expansion enthalpy values and the pseudopotential enthalpy values for the 14 structures of Fig. 5-1 is less than 5 meV. The clusters appearing in the cluster expansion are also illustrated in Fig. 5-2.

To obtain thermodynamic properties for spinel Li_xCoO_2, grand canonical Monte Carlo simulations were applied to the cluster expansion of table 1. A Monte Carlo cell containing 3072 Li sites (octahedral and tetrahedral) was used. 6000-8000 Monte Carlo passes per lattice site were performed at each temperature and chemical potential of which the last 4000 were used for averaging. Free energies were calculated by integrating the chemical potential from x=0 (where the free energy equals the ground state energy) to the desired concentration x.

5.3 Site concentrations

The essential features of the spinel Li_xCoO_2 phase diagram and voltage curve are determined by the availability to the intercalating lithium ions of the two crystallographically distinct 8a and 16c sites. There are twice as many 16c sites as 8a sites

and the energetics of the crystal are sensitive to how these sites are occupied. Fig. 5-1, for example, shows that below x=1/2, the structures in which the Li ions occupy only the tetrahedral 8a sites are energetically more stable than those in which Li ions occupy octahedral 16c sites. The cluster expansion predicts that a single Li ion in an otherwise completely delithiated spinel CoO_2 host is more stable by 130 meV in a tetrahedral site than in an octahedral site. The cluster expansion also predicts that the energy increase associated with bringing two isolated Li ions (one in a tetrahedral site and the other in an octahedral site) to adjacent tetrahedral and octahedral sites is 250 meV (in an otherwise empty host). Adjacent octahedra and tetrahedra share faces and the large energy penalty associated with a simultaneous occupation of these sites is a result of strong electrostatic repulsion between the positively charged lithium ions.

These simple energy considerations already indicate that Li ions will strive to reside in as many energetically favorable tetrahedral sites as possible while minimizing the simultaneous occupation of adjacent tetrahedral-octahedral sites. Below x=1/2 lithium ions can occupy tetrahedral sites to minimize their site enthalpy. The tetrahedral sites, though, are less numerous than the octahedral sites and can only accommodate lithium ions until x reaches 1/2. Beyond x=1/2, lithium ions must fill energetically less favorable octahedral sites which through electrostatic repulsion will tend to displace lithium ions occupying tetrahedral sites to octahedral sites.

Fig. 5-3 illustrate the concentrations in the tetrahedral and octahedral sites as a function of x in Li_xCoO_2 as determined with the Monte Carlo simulations. Fig. 5-3(a) is calculated at 300 K and Fig. 5-3(b) is calculated at 600 K. According to the Monte Carlo simulations, lithium ions added beyond x=1/2 at low temperature displace the original lithium ions occupying the tetrahedral sites to octahedral sites through a first-order phase transformation. This first-order phase transition corresponds to the crossing of a large two phase coexistance region between x=1/2 and 0.95 at constant temperature.

At 600 K, the two phase region between x=0.5 and 0.95 has disappeared, and a solid solution exists at all lithium concentration. Fig. 5-3, shows that as the

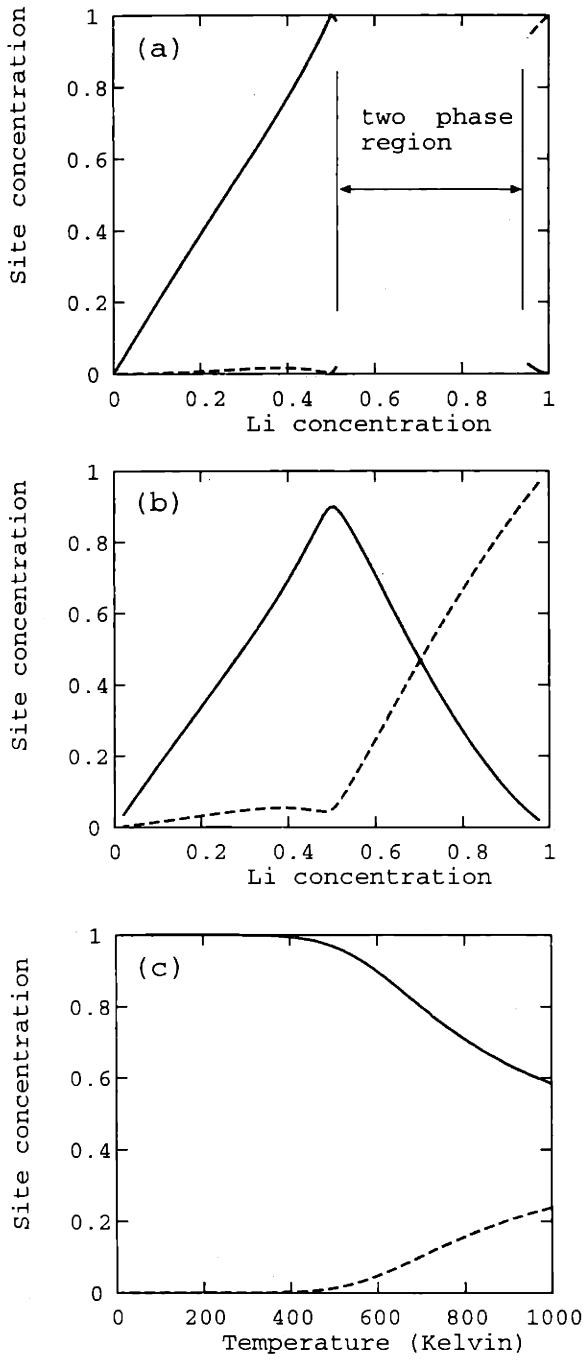

Figure 5-3: Concentrations of Li ions in the tetrahedral sites (full lines) and octahedral sites (dashed lines) as a function of the overall lithium concentration x in Li_xCoO_2 at (a) 300 K and at (b) 600 K. (c) illustrates the dependence of the tetrahedral and octahedral site concentrations as a function of temperature at x=1/2.

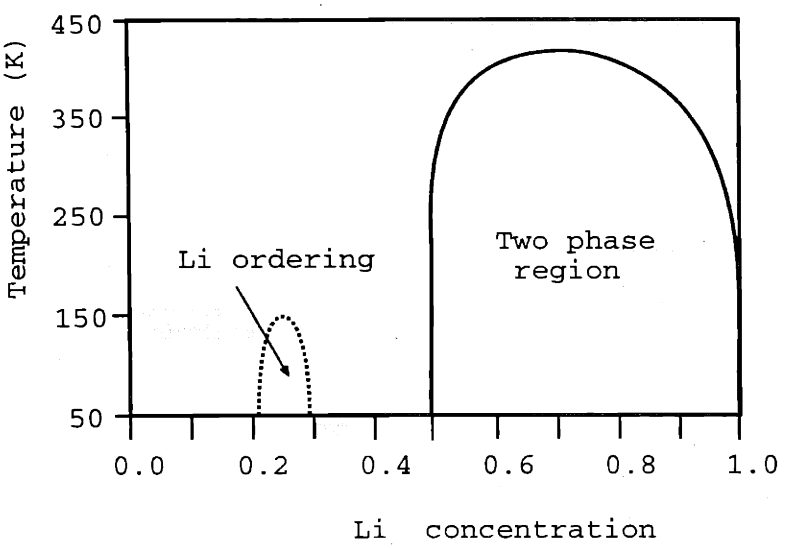

Figure 5-4: Calculated phase diagram of spinel Li_xCoO_2

overall Li concentration is increased from x=1/2 to x=1, the lithium ions initially occupying the tetrahedral sites are gradually displaced to octahedral sites. Even at high temperatures, the lithium ions avoid a simultaneous occupation of adjacent tetrahedral and octahedral sites.

Notice that below x=1/2, lithium ions also occupy octahedral sites, more so at 600 K than at 300 K. This is a result of entropy which becomes more important at high temperature; as the temperature is increased, sufficient thermal energy is available to excite lithium ions into the energetically less favorable octahedral sites. Fig. 5-3(c) illustrates the site occupancy as a function of temperature at x=1/2. At low temperature, all tetrahedral sites are occupied at x=1/2 and the concentration of the octahedral sites increases gradually as the temperature is raised. As is clear in Fig. 5-3, disordering of the lithium ions at x=1/2 proceeds without an order-disorder transition in the sense that the order parameter approaches zero very gradually.

5.4 Phase diagram

Fig. 5-4 illustrates the calculated spinel Li_xCoO_2 phase diagram. It consists of a large miscibility gap between the outer limits of x=0.5 and x=1.0. The miscibility

gap disappears above approximately 420 K and a solid solution exists in which Li ions occupy both octahedral and tetrahedral sites. The miscibility gap results from a competition between filling as many energetically favorable tetrahedral sites while at the same time keeping the occupation of adjacent tetrahedral-octahedral sites to a minimum. Below x=0.5, the Li ions predominantly occupy the tetrahedral sites and form a solid solution. Only below T=150 K do the Li ions order at x=0.25 (see Fig. 5-4) according to a second order phase transformation. In this ordered phase, the Li ions occupy every other tetrahedral site whereby the distribution of lithium and vacancies over the tetrahedral sites is similar to that of Zn and S in zinc blende ZnS.

The formation enthalpies as calculated with the pseudopotential method (Fig. 5-3) indicate that there should also be ordering at x=0.125 and x=0.375 (this is because these enthalpy values lie on the convex hull in Fig. 5-3). The cluster expansion used in this work, however, is too short ranged to predict these phases as ground states. Below x=1/2, the lithium ions occupy almost exclusively the tetrahedral sites which have the connectivity of the diamond crystal structure. A ground state enumeration on the diamond crystal structure [8] has indicated that a lattice model with nearest neighbor and next nearest neighbor pair interactions cannot simultaneously predict a ground state with the ZnS blende structure at y=1/2 (x=0.25) along with ground states at y=1/4 (x=0.125) and 3/4 (x=0.375) where y is the concentration on the diamond crystal structure. The current cluster expansion, predicts the structures at x=0.125 and 0.375 to be exactly degenerate with a phase separation of the ground states at x=0 and 0.25 and x=0.25 and x=0.5. To remove this degeneracy, it would be necessary to include pair clusters and/or multi-body clusters that extend over larger distances than are currently considered. Nevertheless, we expect the ordering at x=0.25 to be the dominant ground state between x=0 and x=0.5.

An interesting aspect of the phase diagram in Fig. 5-4 is that the perfectly ordered spinel phase at x=1/2 does not have an order-disorder phase transition. Instead, as can be seen from Fig. 5-3(c), a fraction of the Li ions which at low temperature occupy exclusively the tetrahedral sites are gradually excited into the octahedral sites over a large temperature interval. The average enthalpy as calculated with the Monte

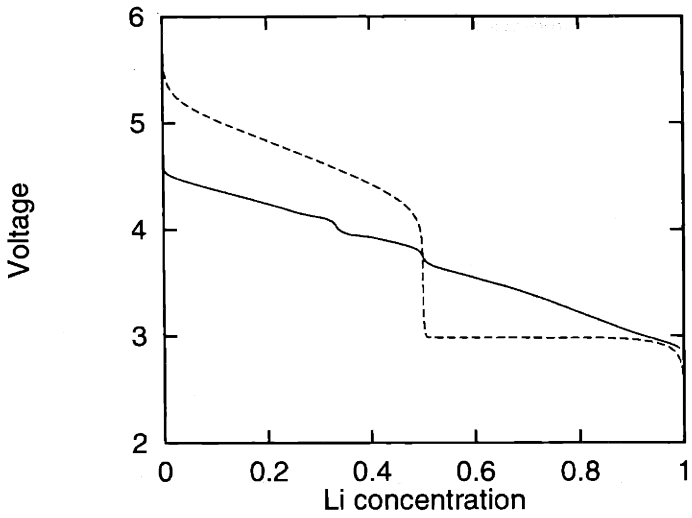

Figure 5-5: Comparison between the calculated voltage profiles of Li_xCoO_2 in the spinel (dashed lines) and O3 (full line) crystal structures.

Carlo simulations does not exhibit a discontinuity characteristic of a first-order phase transition, nor does the heat capacity exhibit a divergence at any temperature. The absence of a unique order-disorder transition temperature is presumably related to the absence of a symmetry change upon going from the completely ordered state to the disordered state. Due to the arrangement of tetrahedral and octahedral sites within the spinel host, the high temperature phase, where the Li ions are distributed over both tetrahedral and octahedral sites exhibits the same symmetry as the perfectly ordered spinel phase $Li_{1/2}CoO_2$ where the Li ions occupy only the tetrahedral sites (*i.e.* the low and high temperature phases have the same unit cell and belong to the same space group). Generally, phase transitions upon cooling occur from a phase with high symmetry to a new phase in which the symmetry is reduced. The lack of a symmetry change is not a sufficient condition for the absence of a phase transition, but it is a necessary one.

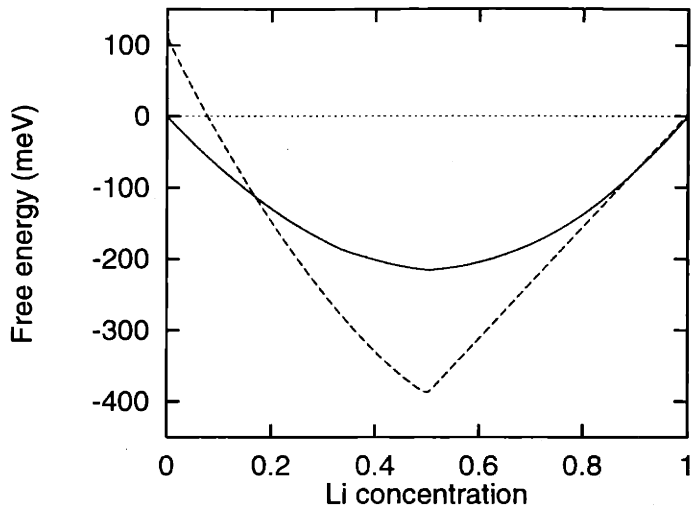

Figure 5-6: Gibbs free energy curves of Li_xCoO_2 in the spinel (dashed line) and the O3 (full line) crystal structures. The free energy of spinel Li_xCoO_2 between x=1/2 and 0.95 corresponds to the tie-line connecting the free energies of the coexisting spinel phases in the miscibility gap.

5.5 Comparison between layered and spinel Li_xCoO_2

5.5.1 voltage curves

Fig. 5-5 compares the voltage curves of Li_xCoO_2 in the spinel phase and in the layered phase. The curves were calculated with Monte Carlo simulations using the cluster expansions for the spinel and O3 phases respectively. It is clear that these curves are qualitatively very different even though the average voltage of Li_xCoO_2 in the two structures are similar. The average voltage is given by the integral under the voltage curves and is predicted with the pseudopotential method to be 3.73 V for layered and 3.84 V for spinel Li_xCoO_2.

The pronounced step in the voltage curve of the spinel host has its origin in the availability to lithium of two crystallographically distinct sites. In the layered form, in which the lithium ions occupy only the octahedral sites, a pronounced step in the voltage curve is absent. The difference in voltage curves can be understood by inspection of the free energy curves of the two hosts. The voltage is linearly related to the lithium chemical potential in the cathode and hence also to the slope of the free energy of Li_xCoO_2 with respect to x. Fig. 5-6 illustrates the free energies of both the

spinel and layered forms of Li_xCoO_2. As is clear from Fig. 5-6, the spinel phase at x=1/2 is very stable and the free energy has a sharp curvature at x=1/2. This means that the slope of the free energy, and in turn the voltage, changes rapidly as a function of lithium concentration around x=1/2. The slope change is most pronounced slightly above x=1/2 since the energetically more favorable tetrahedral sites are saturated at x=1/2 and further Li addition to the host must be accommodated by the energetically less favorable octahedral sites. This causes the free energy to rise sharply immediately above x=1/2. The free energy curve of the layered phase is in comparison smoother as the lithium ions gradually fill the crystallographically identical sites over the whole concentration range.

Voltage curves similar to that calculated for spinel Li_xCoO_2 are observed in spinel Li_xMnO_2 [4, 5, 11] and spinel Li_xTiO_2 [37]. The voltage curves of these structures all have the characteristic one volt step at x=1/2 in common. In the Mn compound, it has been argued that the step arises from a cooperative Jahn-Teller distortion of the host which is fully in place at the $LiMnO_2$ stoichiometry [11]. The theoretical study of spinel Li_xCoO_2, where the effect of Jahn-Teller distortions are absent, shows that the step at x=1/2 is not produced by a Jahn-Teller distortion, but is instead caused by structural features of the spinel host structure. In fact, a cooperative Jahn-Teller distortion of stoichiometric $LiMnO_2$ actually reduces the step at x=1/2. This can be understood by considering the effect of such a Jahn-Teller distortion on the free energy curve of Fig. 5-6. In Li_xMnO_2, the coordinated Jahn-Teller distortion occurring at high Li concentration lowers the free energy of cubic spinel $LiMnO_2$ by producing an energetically more stable tetragonally distorted spinel form of $LiMnO_2$. The Jahn-Teller distortion in this material, therefore, reduces the voltage step since it would reduce the sharpness of free energy at x=1/2.

Another way to reduce the voltage step at x=1/2 in spinel compounds is by raising the temperature. The increased thermal excitations at high temperature scramble the perfect ordering of Li ions in the tetrahedral sites and cause them to start occupying energetically less favorable octahedral sites. This is clearly evident in Fig. 5-7 where the voltage step starts to disappear at 600 K as a result of the reduction of the Li

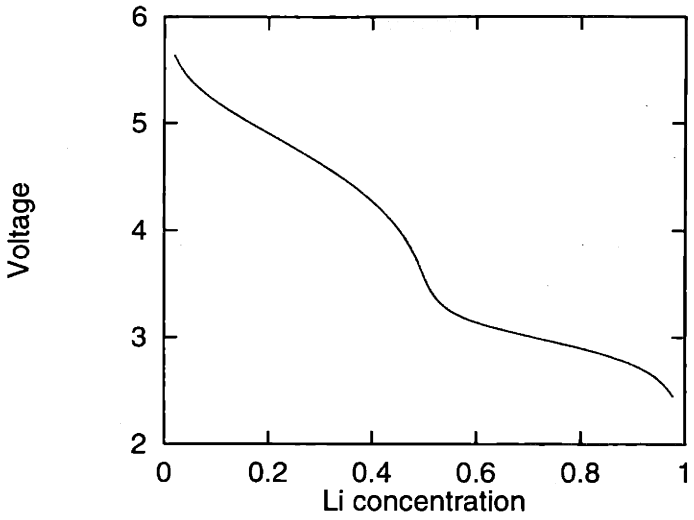

Figure 5-7: Calculated voltage curve of spinel Li_xCoO_2 at 600 K.

concentration in the tetrahedral sites (Fig. 5-3(b) and (c)) of the spinel host. Lithium disorder smears out the free energy curve around x=1/2.

5.5.2 Relative stability

While a study of the phase diagrams of layered and spinel Li_xCoO_2 are valuable for understanding phase stability during a typical charge and discharge cycle, it is also of interest to investigate the relative stability between the layered and spinel forms to understand possible causes of degradation over many charge/discharge cycles. First principles investigations by Wolverton and Zunger [126] exposed the fact that spinel Li_xCoO_2 is energetically more stable by almost 200 meV than layered Li_xCoO_2 around x=1/2. At x=1, they found that layered Li_xCoO_2 is only slightly more stable than lithiated spinel while at x=0, they found that the layered form is more stable than spinel by 100 meV [126]. Although these comparisons of stability neglected the effect of configurational entropy, the free energy curves calculated at room temperature using the cluster expansions for the spinel and O3 forms of Li_xCoO_2 convey the same qualitative trends.

The fact that there is a driving force of almost 200 meV for transformation from the layered phase to the spinel phase at x=1/2 in Li_xCoO_2 is surprising since this transformation has rarely been observed experimentally, and when it has been ob-

served, the amount of spinel phase formed has been low [138]. Nevertheless, this result exposes a potential failure mechanism for the cathodes with the layered phase, since during each charge, there exists a thermodynamic driving force to irreversibly transform to the spinel form. Due the the more favorable voltage characteristics of the layered form, there has been an intense search in recent years to fabricate other transition metal oxides, most notably Li_xMnO_2 in the layered crystal structure. In this respect, it is of interest to know the relative stability between the layered and spinel forms in different lithium transition metal oxides. First principles calculations of energies of layered and spinel forms of Li_xMO_2 compounds where M are important transition metals such as Mn and Ni also predict that around x=1/2, the spinel form is energetically more stable than the layered form [8].

Although the transformation from layered to spinel does not seem to occur readily in Li_xCoO_2, there is evidence that it does occur the other transition metal oxides. In recent years, it has been possible to synthesize $LiMnO_2$ in a layered structure [35, 36, 139, 140, 141]. Upon deintercalation in a battery, however, the layered form of $LiMnO_2$ very rapidly transform to a defective spinel crystal structure, a result which is consistent with first principles predictions for this compound [142, 8]. The same appears to be true for the layered form of Li_xNiO_2. Although stable under ambient conditions, around x=1/2, this compound has been observed to transform to spinel at 200^o C [143, 144].

Since there is a driving force in each case, the difference in behavior between the three different transition metal oxides is a clear example of the role that kinetics can play. During a transformation from the layered form to the spinel form, metal ions must diffuse from the metal layer into the lithium layer. This must occur by squeezing through a close-packed oxygen plane. One possibility is that Co diffusion is much lower than Mn diffusion within the oxygen skeletal structure. Another possibility is that in the case of cobalt, the transformation proceeds by a nucleation and growth mechanism while in the Mn compound the transformation occurs spontaneously, similar to what is observed in spinodal decomposition.

5.6 Conclusion

The significant differences in electrochemical properties between the spinel and layered forms of Li_xCoO_2 are in large part a result of the fact that spinel offers both tetrahedral and octahedral sites for lithium ions while the layered O3 phase has only octahedral sites available for lithium ions. Both the phase diagrams and the voltage curves of the two crystal structures have important qualitative differences. A significant feature about spinel lithium transition metal oxides is that the tetrahedral sites are energetically more favorable than the octahedral sites for occupation by lithium ions, yet they are not as numerous. This causes a large miscibility gap whereby two forms of spinel coexist: one form with all the tetrahedral sites occupied at x=1/2 and the other with all the octahedral sites filled at x=1. In fact, the immense stability of the tetrahedral sites results in a free energy curve with a sharp curvature at x=1/2. The sharp curvature translates into a large voltage step at x=1/2, a feature that is characteristic of all lithium transition metal oxides with the spinel crystal structure.

An interesting feature about the phase diagram of spinel Li_xCoO_2 is the absence upon heating or cooling of a well defined order-disorder transition at x=1/2. In the low temperature form of $Li_{1/2}CoO_2$ the lithium ions occupy exclusively the tetrahedral sites while at high temperature the lithium ions are disordered over both the tetrahedral and octahedral sites. The absence of a symmetry change between the low temperature ordered phase and the high temperature disordered phase makes such a smooth transition possible.

Although the spinel form of Li_xCoO_2 is technologically not very important, the first principles investigation of its properties has enabled us to isolate the effect of the crystal structure on the thermodynamic properties of a given lithium transition metal oxide. Many of the properties predicted for spinel Li_xCoO_2 are observed in the spinel form of Li_xMnO_2, even though the manganese ions induce Jahn-Teller distortions, charge ordering and magnetic ordering.

Chapter 6

Effect of oxygen vacancies on the electrochemical properties of layered Li_xCoO_2

6.1 Introduction

In the previous two chapters, we considered phase stability in Li_xCoO_2 assuming a perfect CoO_2 host structure. In reality, though, the CoO_2 host will contain defects, the most common of which are expected to be oxygen vacancies. As lithium is removed from $LiCoO_2$, the compound is oxidized whereby the effective valence of Co progressively changes from +3 to +4. As described in chapter 3, this is countered by a shift in the nature of bonding in Li_xCoO_2 whereby the Co-O bonds become more covalent as x is reduced. Another way that oxidation is accommodated is through oxygen loss to the environment. Although the formation of oxygen vacancies within Li_xCoO_2 has a large energetic cost, there is an enormous entropic gain when the oxygen ions form O_2 molecules in the gas phase. The equilibrium concentration of oxygen vacancies in Li_xCoO_2 depends sensitively on the temperature and oxygen partial pressure in the environment. The equilibrium oxygen vacancy concentration will increase as the lithium concentration is reduced since the compound becomes more

oxidized. Furthermore, the oxygen vacancy concentration increases as the temperature is raised, since entropy becomes more important at elevated temperature. We refer to the oxygen vacancy concentration as δ which is defined by $Li_xCoO_{2-\delta}$.

The mobility of oxygen vacancies within the Li_xCoO_2 host is exceedlingly low. In fact, a calculation within LDA of the activation barrier (see chapter 7) for the migration of an isolated oxygen vacancy is on the order of 3 eV. At ambient temperatures, therefore, oxygen loss to the environment is severly limited by kinetics, and the equilibrium oxygen vacancy concentration as a function of the lithium concentration x is unlikely to be obtained during typical charge and discharge cycles. Nevertheless, a certain concentration of oxygen vacancies will be present in the layered Li_xCoO_2 host since this compound is typically synthesized around 800° C where the thermodynamic driving force for oxygen vacancy formation and the mobility for oxygen vacancy diffusion is significantly higher than at room temperature.

In this chapter, we investigate the effect of a dilute and fixed oxygen vacancy concentration on the electrochemical characteristics of Li_xCoO_2 and on the predicted transition temperatures of the ordered phases at x=1/2 and 1/3. We omit an investigation of the equilibrium oxygen vacancy concentration, because the local density approximation results in significant errors when comparing enthalpies of an element in the solid and the same element in a molecule in the gas phase. Since the equilibrium oxygen vacancy concentration depends exponentially on this enthalpy difference, any serious errors will be magnified many fold in the predicted equilibrium oxygen vacancy concentration. We limit ourselves to oxygen vacancies, although more complicated defects to the host can be expected due to certain fabrication methods. Levasseur *et al* [145], for example, have fabricated lithium excess forms of Li_xCoO_2 which are believed to contain a combination of oxygen vacancies along with cobalt vacancies.

A first step in determining the effect of oxygen vacancies on the behavior of the lithium ions is an understanding of the evolution of the oxygen-vacancy formation enthalpy with the local lithium-vacancy configuration. The oxygen-vacancy formation enthalpy is the enthalpy increase associated with taking an oxygen ion out of the crystal and placing it in its atomic ground state at infinity. To understand the

dependence of the vacancy formation enthalpy on the degree of lithium disorder, we use a local cluster expansion (see chapter 2). The local cluster expansion can then be implemented in Monte Carlo simulations to investigate the effect of oxygen vacancies on the thermodynamic properties.

6.2 Oxygen-vacancy formation enthalpies

Oxygen-vacancy formation enthalpies were calculated using a supercell of Li_xCoO_2 containing different lithium-vacancy arrangements. The supercell contained 12 Li_xCoO_2 formula units. Oxygen-vacancy formation enthalpies are defined as

$$\Delta H_{O_V} = H_{Li_{12x}Co_{12}O_{23}} + H_O - H_{Li_{12x}Co_{12}O_{24}} \tag{6.1}$$

where $H_{Li_{12x}Co_{12}O_{24}}$ is the enthalpy of the supercell with a particular lithium-vacancy arrangement at concentration x and a defect free CoO_2 host structure. $H_{Li_{12x}Co_{12}O_{23}}$ is the enthalpy of the supercell with the same lithium-vacancy arrangement, but with an oxygen vacancy in the CoO_2 host and H_O is the enthalpy of an isolated oxygen atom in its ground state electronic configuration. The enthalpy $H_{Li_{12x}Co_{12}O_{24}}$ was calculated within LDA by relaxing both the volume and the internal ion coordinates. $H_{Li_{12x}Co_{12}O_{23}}$ was calculated at the same equilibrium volume as the structure without the oxygen vacancy but internal ion coordinates were allowed to relax.

Fig. 6-1 illustrates twelve different oxygen-vacancy formation enthalpies as calculated with the pseudopotential method in the local density approximation. The formation enthalpies at x=1 and x=0 correspond to oxygen-vacancy formation enthalpies for fully lithiated and fully delithiated cases. At other lithium concentrations, E_{O_V} is not uniquely specified by a particular lithium-vacancy arrangement but also depends on the relative position of the oxygen vacancy with respect to the lithium-vacancy configuration. Hence at a particular lithium concentration, different oxygen-vacancy formation enthalpies are possible. This is illustrated in Fig. 6-1 for example at x=11/12 where three oxygen-vacancy formation enthalpies are illustrated.

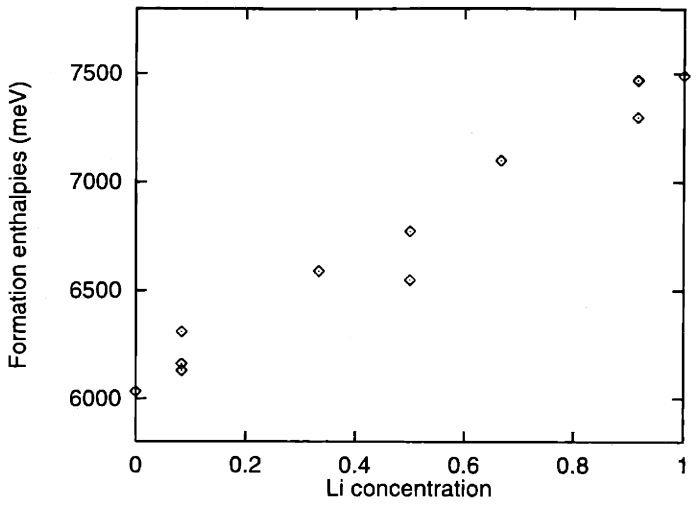

Figure 6-1: Oxygen-vacancy formation enthalpies for the O3 form of Li_xCoO_2 as a function of lithium concentration and arrangement.

At x=11/12, only one lithium vacancy is present in the supercell. The lowest oxygen-vacancy formation enthalpy occurs when the oxygen vacancy is as close as possible to the lithium vacancy. The oxygen-vacancy formation enthalpy progressively increases as the lithium vacancy is placed further away from the oxygen vacancy. In Fig. 6-1 the two oxygen-vacancy formation enthalpies at x=11/12 that are almost degenerate and have values around 7500 meV correspond to the enthalpies for a lithium vacancy within the second nearest neighbor shell and the third nearest neighbor shell away from the oxygen vacancy. Notice that when a lithium vacancy is in the second or third nearest neighbor shell away from the oxygen vacancy, the oxygen-vacancy formation enthalpy approximates the formation enthalpy at x=1 where lithium vacancies are completely absent. This shows that the configuration dependence of the oxygen-vacancy formation enthalpy is short range. It suggests that an oxygen vacancy does not see an isolated lithium vacancy beyond the second nearest neighbor distance from the oxygen vacancy.

At x=1/12, three oxygen-vacancy formation enthalpies are shown again, each corresponding to an isolated lithium ion at different distances away from the oxygen vacancy. The oxygen-vacancy formation enthalpy is the highest when the isolated lithium ion is directly adjacent to the oxygen vacancy. The oxygen-vacancy formation enthalpy decreases as the lithium ion is placed further away from the oxygen vacancy.

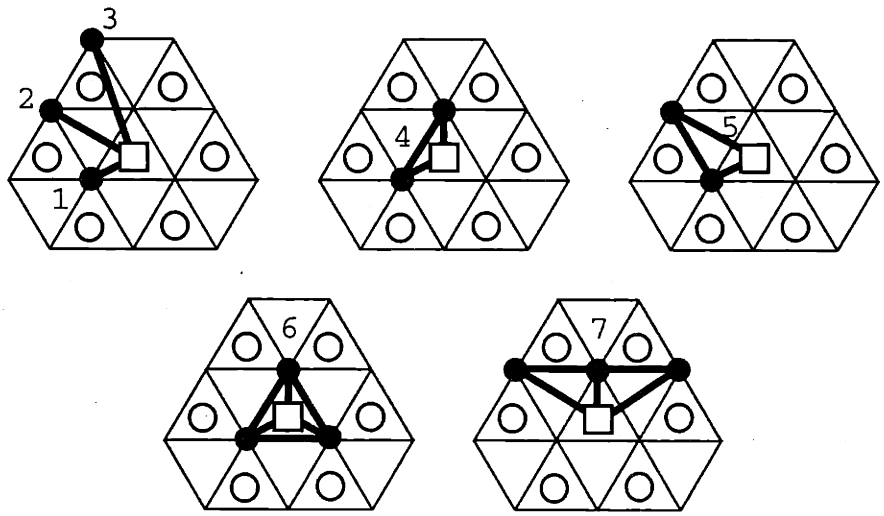

Figure 6-2: Clusters used in the local cluster expansion for the oxygen-vacancy formation enthalpy of the O3 form of Li_xCoO_2. The triangular lattice corresponds to the lithium sites and the circles correspond to oxygen ions adjacent to the lithium plane. The square signifies an oxygen vacancy.

These results illustrate that in the dilute concentration limits, *a lithium ion is repelled by an oxygen vacancy.* In effect, an oxygen ion raises the site enthalpy for lithium occupation of the lithium sites in the immediate vicinity of the oxygen vacancy. An oxygen vacancy can be considered as have an effective positive charge (due to the absence of a negatively charged oxygen ion) while a vacancy in the lithium plane has an effective negative charge. Oxygen vacancies therefore attract lithium vacancies.

Notice in Fig. 6-1 that as the Li concentration is decreased, the oxygen-vacancy formation enthalpy reduces. This means that with decreasing x, it becomes energetically less costly to remove an oxygen ion from an otherwise perfect CoO_2 host.

6.3 Local cluster expansion

An inspection of the oxygen-vacancy formation enthalpies at the dilute extremes indicates that an oxygen vacancy attracts isolated lithium vacancies at high lithium concentration and repels isolated lithium ions at low lithium concentration. At intermediate lithium concentrations, many possible lithium-vacancies arrangements around

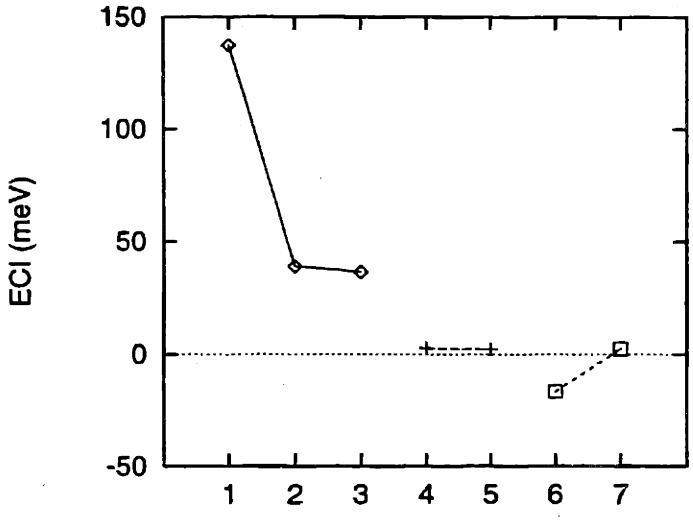

Figure 6-3: ECI for the local cluster expansion of the oxygen-vacancy formation enthalpy. See Fig. 6-2 for the numbering of the clusters.

an oxygen vacancy can exist and these will alter with concentration and temperature. To approximate the enthalpy of arbitrary lithium-vacancy arrangements around an oxygen vacancy we used the twelve oxygen-vacancy formation enthalpies of Fig. 6-1 to parameterize a local cluster expansion. This local cluster expansion contains clusters extending up to the third nearest neighbor shell from the oxygen vacancy. The clusters of the expansion are illustrated in Fig. 6-2 and their values are plotted in Fig. 6-3. The root mean square error between the first principles oxygen-vacancy formation enthalpies and those calculated with the local cluster expansion is 57 meV, or roughly 1 percent of the oxygen-vacancy formation enthalpies.

The local cluster expansion was implemented in Monte Carlo simulations together with the cluster expansion for the configurational enthalpy for the O3 host. Oxygen vacancies were randomly distributed throughout the Monte Carlo cell in such a way that the interaction range of any oxygen vacancy does not overlap with the interaction ranges of the other oxygen vacancies. The enthalpy of the crystal was calculated by first using the cluster expansion for the lithium-vacancy configurational enthalpy and then calculating the oxygen-vacancy formation enthalpies for each oxygen vacancy in the Monte Carlo cell using the local cluster expansion. Simply adding the two components yields the total enthalpy of the crystal.

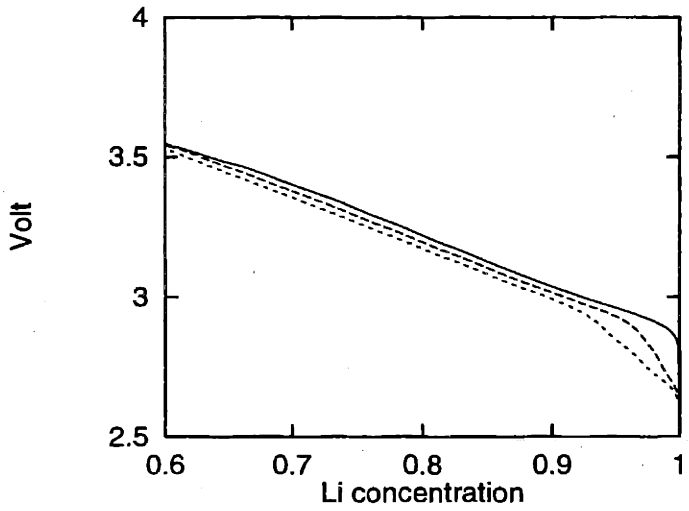

Figure 6-4: Voltage curves for $Li_xCoO_{2-\delta}$ for δ=0 (solid line), 0.015 (middle dashed line) and 0.03 (lowest dashed line).

6.4 Oxygen vacancies and electrochemical properties

With the Monte Carlo simulations, it is possible to probe the effect of oxygen vacancies on the voltage curve. Fig. 6-4 illustrates the calculated voltage of Li_xCoO_2 in the absence of any oxygen vacancies and with δ= 0.015 and 0.03 in $Li_xCoO_{2-\delta}$. Oxygen vacancies leave a clear imprint at the initial stages of deintercalation by producing a small kink in the voltage profile.

The kink can be understood by inspection of the concentration of lithium ions in the immediate vicinity of the oxygen vacancies. Fig. 6-5 illustrates the average concentrations around oxygen vacancies within the first, second and third nearest neighbor shells. As can be seen, in the initial stages of deinteracalation, on average, two of the three lithium ions within the first nearest neighbor shell around the oxygen vacancies are almost instantaneously removed. (The nearest neighbor shell of an oxygen vacancy has three lithium sites.) It is no coincidence that exactly two lithium ions immediately adjacent to an oxygen vacancy are instantaneously removed since the effective charge of an oxygen ion is -2 while that of a lithium ion is +1. Oxygen vacancies repel the lithium ions occupying the sites within the first nearest neighbor

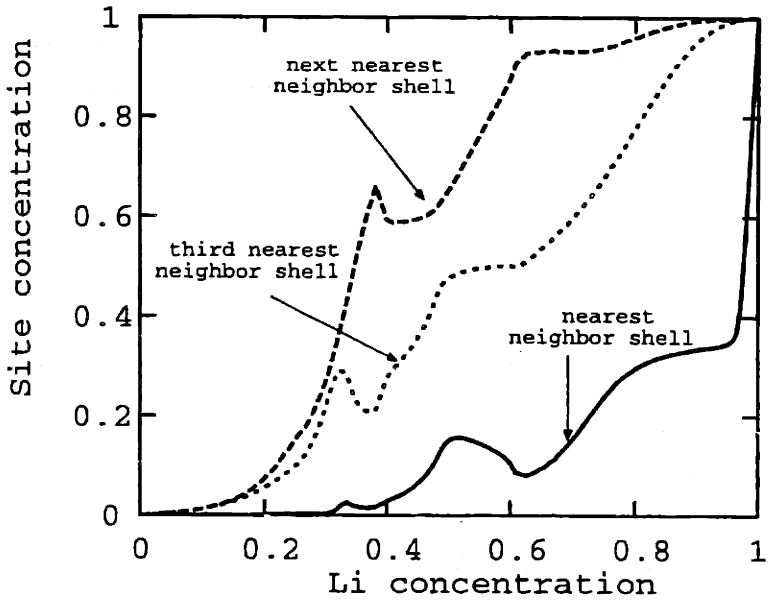

Figure 6-5: Average lithium concentration in different neighboring shells from oxygen vacancies in $Li_xCoO_{2-\delta}$ with δ=0.015.

shell the most, causing them to be vacated at a lower voltage than the other sites in the crystal. One lithium ion remains within the first nearest neighbor shell around an oxygen vacancy, though, since the energetic penalty of having a triplet of vacancies at high lithium concentration is high as a result of the charge imbalance this would produce. The width of the kink in the voltage profile is directly related to the number of lithium ions repelled by the oxygen vacancies. The kink spans a lithium concentration interval that is approximately twice the number of oxygen vacancies δ in $Li_xCoO_{2-\delta}$ since each oxygen vacancy repels two lithium ions.

Oxygen vacancies also affect the phase boundaries of the ordered lithium-vacancy phases. The local lithium-vacancy arrangements that are energetically preferred around an oxygen vacancy are not necessarily compatible with the lithium-vacancy arrangement in the ordered phases. This will destabilize the ordered phase with respect to the disordered phase where the preferred local lithium-vacancy environment around an oxygen vacancy can be more easily accommodated. Furthermore, a random distribution of oxygen vacancies can produce incommensurabilities that will further destabilize the ordered phase. Fig. 6-6 illustrates the effect of oxygen vacancies on the

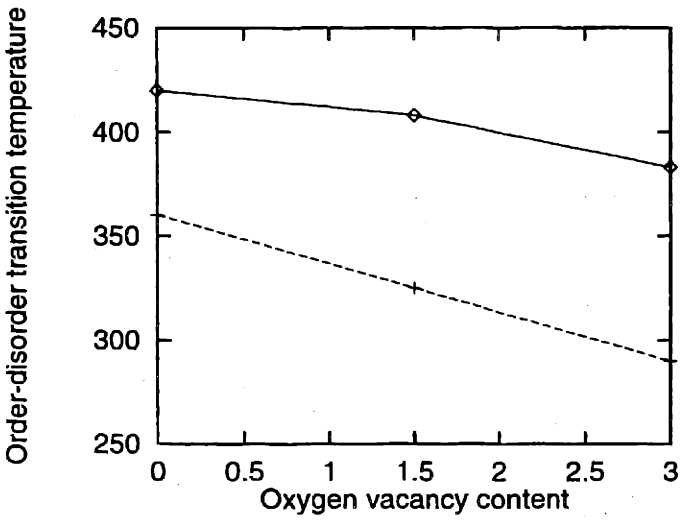

Figure 6-6: Dependence of the order-disorder transition temperatures of the ordered phases at x=1/2 and x=1/3 in the O3 form of $Li_xCoO_{2-\delta}$ (see Fig. 4-6). The order-disorder transition temperature as a function of the oxygen vacancy concentration δ at x=1/2 is plotted with the solid line and at x=1/3 it is plotted with the dashed line.

order-disorder transition temperatures of the lithium ordering at x=1/2 and 1/3. The order-disorder transition temperatures decrease as the oxygen vacancy concentration increases.

6.5 Conclusion

The results of this chapter show that the effect of a dilute concentration of oxygen vacancies in Li_xCoO_2 is to create a kink in the voltage curve at the initial stages of charge. The pseudopotential calculations within LDA show that oxygen vacancies repel neighboring lithium ions. Hence the lithium ions adjacent to oxygen vacancies are removed at a lower voltage than the other lithium ions that are not effected by the oxygen vacancies. The Monte Carlo simulations predict that on average, two lithium ions per oxygen vacancy are initially removed from sites within the first nearest neighbor shell of each oxygen vacancy.

A similar effect can be expected in lithium transition metal oxides having the spinel crystal structure. The voltage curve of the spinel crystal structure is characterized

by a large step at x=1/2 in Li_xMO_2 where M is a transition metal. As was shown in chapter 5, lithium ions occupy tetrahedral sites below x=1/2 and predominantly occupy octahedral sites around x=1. In the spinel structure, we can expect oxygen vacancies to produce a kink around x=1 and again in the voltage step at x=1/2. An oxygen vacancy will repel neighboring lithium ions residing on octahedral sites when x=1 and it will repel neighboring lithium ions on tetrahedral sites when x=1/2.

The Monte Carlo simulations also predict that oxygen vacancies reduce the order-disorder transition temperatures of ordered phases. The preferred lithium-vacancy arrangement around an oxygen vacancy is not always compatible with different long-range ordered lithium-vacancy configurations. The disordered phase can more easily accommodate the preferred lithium-vacancy arrangement around an oxygen vacancy. Hence oxygen vacancies stabilize the disordered phase over the ordered phase. This is an important result, since order-disorder transition temperatures in oxides are often significantly over-predicted from first principles [146]. The presence of oxygen vacancies could explain some of this discrepancy.

Chapter 7

Diffusion from first principles

The rate at which an electrochemical cell containing a Li_xMO_2 cathode material can be charged and discharged depends on the lithium mobility within the MO_2 host. The process of removing and inserting lithium into Li_xCoO_2 is a kinetic process and is associated with irreversibility. In order for lithium ions to leave the cathode, the cathode must be in a state that is out of equilibrium. This can be done by inducing a concentration gradient by for example changing the lithium chemical potential at the surface of the cathode particle. Kinetic parameters such as diffusivity D or mobility M relate a driving force such as a concentration gradient or a chemical potential gradient to a resultant net flux of lithium ions within the host. Although D and M describe irreversible processes, the theory of irreversible thermodynamics shows that kinetic parameters such as these can be calculated by a consideration of the thermodynamic fluctuations that occur in a system at equilibrium [147, 148, 149, 150, 151, 152]. In this chapter, we briefly describe the phenomenological theory of diffusion and review how kinetic parameters can be determined from an investigation of thermodynamic fluctuations of a solid at equilibrium. We then present a procedure that enables the calculation of the diffusion coefficient from first principles. We restrict our discussion to the diffusion of a single type of particle on a lattice within a host.

7.1 Phenomenological equations for diffusion

According to the theory of irreversible thermodynamics [147, 148], the natural driving force for diffusion is the gradient in lithium chemical potential $\vec{\nabla}\mu_{Li}$. Such a gradient produces a diffusive flux $\vec{J}$ which is related to the driving force according to

$$\vec{J} = -L\vec{\nabla}\mu_{Li} \tag{7.1}$$

L is a kinetic parameter that is determined by the mobility of lithium. μ_{Li}, the lithium chemical potential expressed per Li_xMO_2 formula unit, is a function of the Li concentration x. The gradient of μ_{Li} can therefore also be written as

$$\vec{\nabla}\mu_{Li} = V_\Omega \frac{\partial \mu_{Li}}{\partial x}\vec{\nabla}c \tag{7.2}$$

where V_Ω is the volume per Li_xMO_2 formula unit and c is defined as x/V_Ω. (7.2) is valid for small enough gradients in concentration such that the concentration dependence of V_Ω can be neglected. Another way of writing (7.2) is

$$\vec{\nabla}\mu_{Li} = k_B T V_\Omega \frac{\partial\left(\mu_{Li}/k_BT\right)}{\partial \ln x}\frac{d\ln x}{dx}\vec{\nabla}c = \frac{k_BT}{c}\frac{\partial\left(\mu_{Li}/k_BT\right)}{\partial \ln x}\vec{\nabla}c \tag{7.3}$$

Using (7.3), we can rewrite (7.1) as

$$\vec{J} = -L\left(\frac{k_BT}{c}\right)\frac{\partial(\mu_{Li}/k_BT)}{\partial \ln x}\vec{\nabla}c \tag{7.4}$$

By defining the diffusion coefficient D as

$$D = L\left(\frac{k_BT}{c}\right)\frac{\partial(\mu_{Li}/k_BT)}{\partial \ln x} \tag{7.5}$$

we obtain Fick's law

$$\vec{J} = -D\vec{\nabla}c \tag{7.6}$$

D and L are tensors which for diffusion of a single type of particle in a host can be represented by a 3×3 matrix. Symmetry determines which elements of these matrices

are non-zero. For lithium diffusion in the cubic spinel host, diffusion is isotropic and the tensor for D has only diagonal elements that are all equal. For lithium diffusion in the layered host, diffusion along the c-axis can be neglected due to the almost impenetrable O-Co-O slabs, while diffusion within the lithium planes is isotropic as a result of the high symmetry of the two-dimensional triangular lattice.

It is convenient to introduce the thermodynamic factor Θ defined as

$$\Theta = \frac{\partial(\mu_{Li}/k_BT)}{\partial \ln x} \tag{7.7}$$

The thermodynamic factor expresses the deviation of the solid solution from ideality. In an ideal solution, the chemical potential can be written as

$$\mu = \mu^o + k_BT \ln x \tag{7.8}$$

where μ^o is independent of x and is the chemical potential in the standard state (*i.e.* x=1). For an ideal solution, Θ=1 and (7.5) reduces to the familiar Nernst-Einstein relation

$$\frac{D}{k_BT} = \frac{L}{c} = M \tag{7.9}$$

where the ratio L/c is referred to as the lithium mobility M. Around an ordered phase, the chemical potential deviates strongly from ideality and the thermodynamic factor becomes much larger than unity. Hence in an ordered phase, there is a large thermodynamic enhancement of the diffusivity. This arises simply from the fact that in an ordered phase, a small gradient in concentration produces a large gradient in chemical potential.

7.2 D and thermodynamic fluctuations

The validity of irreversible thermodynamics is restricted to systems that are *not too far removed from equilibrium* [147, 148]. To quantify this, it is useful to mentally divide the solid into small subregions each with volume V_s. If the subregions can be

made microscopically large enough for thermodynamic variables to be meaningful yet macroscopically small enough such that the same thermodynamic variables can be considered constant within each subregion, the solid is said to be in *local equilibrium* or equivalently *not too far removed from equilibrium.* Hence, although the solid itself is removed from equilibrium, each subregion with volume V_s can be considered locally in equilibrium. The local equilibrium assumption is valid as long as gradients in quantities as concentration and temperature are not too large, a requirement that is generally satisfied in most cases of practical interest.

Within this framework, the kinetic parameters D and L can be derived by a consideration of relevant fluctuations at thermodynamic equilibrium. Crucial in this derivation, is the assumption made by Onsager in his proof of the reciprocity relations of kinetic parameters [153, 154], that the regression of a fluctuation of a particular extensive property around its equilibrium value occurs according to the same phenomenological laws as those governing the regression of artificially induced fluxes of the same extensive property. It is now recognized that this regression hypothesis is a consequence of an important fluctuation-dissipation theorem of non-equilibrium statistical mechanics [155].

Onsager's regression hypothesis is valid strictly within the local equilibrium approximation. This means that it is restricted to fluctuations of extensive properties averaged over the microscopically large (i.e. thermodynamic limit) subregions. Mathematically this is expressed as a limit $k \to 0$ where k is the wave vector of the Fourier components of the fluctuation. The regression hypothesis is also typically only justified on time scales of macroscopic measurements. These conditions are often referred to as the *hydrodynamic limit* [155, 57].

Since the number of lithium ions are conserved, the following continuity equation must hold

$$\frac{\partial c(\vec{r},t)}{\partial t} = -\vec{\nabla}\vec{J}(\vec{r},t) \tag{7.10}$$

where the variables $\vec{r}$ and t emphasize the position and time dependence of the con-

centration c and flux $\vec{J}$. With Fick's law, (7.6), the continuity equation becomes

$$\frac{\partial c(\vec{r},t)}{\partial t} = \vec{\nabla} D \vec{\nabla} c(\vec{r},t) \tag{7.11}$$

This equation dictates how an initial concentration profile $c(\vec{r}, t = 0)$ removed from equilibrium evolves with time.

A measure of fluctuations in the concentration profile are time correlation functions defined as

$$S(\vec{r} - \vec{r'}, t) = \left\langle \delta c(\vec{r},t) \delta c(\vec{r'}, 0) \right\rangle \tag{7.12}$$

where $\delta c(\vec{r},t) = c(\vec{r},t) - c_o$ with c_o the equilibrium concentration. For large wave length fluctuations at equilibrium, S can be assumed to depend on $\vec{r} - \vec{r'}$ instead of $\vec{r}$ and $\vec{r'}$ separately. The brackets in (7.12) denote an ensemble average with the initial probability distribution at t=0. The mathematical formulation of the regression hypothesis of Onsager, states that the correlation function S in the hydrodynamic limit should satisfy the continuity equation (7.11) which incorporates Fick's law (7.6)

$$\frac{\partial S(\vec{r} - \vec{r'}, t)}{\partial t} = D \vec{\nabla}^2 S(\vec{r} - \vec{r'}, t) \tag{7.13}$$

where the concentration dependence of D has been neglected since concentration fluctuations at equilibrium are typically small. After a series of mathematical manipulations applied to the above equation (see appendix) and after taking the hydrodynamic limit, the following expression for the diffusion coefficient [151, 156, 157] is obtained

$$D = \frac{1}{\langle (\delta c)^2 \rangle \, d} \int_0^\infty \left\langle \vec{J}(0) \vec{J}(t) \right\rangle dt \tag{7.14}$$

where d is the dimension of the space in which diffusion occurs. In spinel Li_xCoO_2 for example, d is equal to 3 while in layered Li_xCoO_2, d is equal to 2. (7.14) can be written explicitly in terms of particle velocities as

$$D = \left(\frac{\langle N \rangle}{\langle (\delta N)^2 \rangle} \right) \frac{1}{\langle N \rangle \, d} \int_0^\infty \left\langle \sum_{i=1}^{N} \vec{v}_i(0) \sum_{j=1}^{N} \vec{v}_j(t) \right\rangle dt \tag{7.15}$$

where N refers to the number of lithium ions and δN is the fluctuation of the number of lithium ions within a reference volume, that we denote by V_s . $\langle N \rangle$ is the average number of lithium ions in the reference volume V_s. Equations (7.14) and (7.15) are often referred to as Kubo-Green type of equations in that a kinetic parameter is related to a correlation function of the relevant currents at equilibrium. D in (7.15) corresponds to the diffusion coefficient appearing in Fick's law (7.6).

The prefactor in parenthesis in (7.15) is a thermodynamic quantity, and can be shown to be identical to the thermodynamic factor Θ defined in the previous section [156]

$$\Theta = \frac{\partial(\mu_{Li}/k_BT)}{\partial \ln x} = \frac{\langle N \rangle}{\langle (\delta N)^2 \rangle} \tag{7.16}$$

With this observation, the kinetic parameter L defined by (7.1) and related to D according to (7.5) , becomes

$$L = \frac{D}{\Theta}\frac{c}{k_BT} = \frac{1}{k_BTV_sd}\int_0^\infty \left\langle \sum_{i=1}^{N} \vec{v}_i(0) \sum_{j=1}^{N} \vec{v}_j(t) \right\rangle dt \tag{7.17}$$

V_s corresponds to the reference volume containing on average $\langle N \rangle$ lithium ions. By defining D_J as

$$D_J = L\frac{k_BT}{c} = \frac{1}{\langle N \rangle d}\int_0^\infty \left\langle \sum_{i=1}^{N} \vec{v}_i(0) \sum_{j=1}^{N} \vec{v}_j(t) \right\rangle dt \tag{7.18}$$

we can write

$$D = \Theta D_J \tag{7.19}$$

which is a product of a thermodynamic term Θ and a kinetic term D_J.

Although D describes macroscopic diffusion in the presence of a concentration gradient, frequently much attention is also paid to a self diffusion coefficient D^* which is determined by the velocity self correlations of individual particles [152, 156] according to

$$D^* = \frac{1}{2N}\sum_{i=1}^{N}\int_0^\infty \langle \vec{v}_i(0)\vec{v}_i(t) \rangle \, dt \tag{7.20}$$

In (7.20), the correlation is that of the velocity of each lithium ion at $t = 0$ with the

velocity of the same lithium ion at time t. Apart from the thermodynamic factor Θ, D^* also neglects the cross velocity correlations between different diffusing particles. Hence

$$\frac{D}{D^*} = \Theta \left(1 + \frac{\int_0^\infty \left\langle \sum_{i \neq j} \vec{v}_i(0) \vec{v}_j(t) \right\rangle dt}{\int_0^\infty \langle \sum_i \vec{v}_i(0) \vec{v}_i(t) \rangle \, dt} \right) \tag{7.21}$$

In situations where cross velocity correlations between different lithium ions are negligible D is related to the self diffusion coefficient D^* according

$$D = \Theta D^* \tag{7.22}$$

This equation is the familiar Darken approximation. It has the same form as the more rigorous expression for D given by (7.19). This similarity shows that D_J introduced in (7.18) can be viewed as a tracer diffusion coefficient which includes the correlations between the velocities of the other diffusing lithium ions.

7.3 Diffusion for a lattice model

The lithium ions within Li_xMO_2 spend most of their time at well defined equilibrium sites and only a very small fraction of the time along paths connecting adjacent sites. Diffusion arises from the migration of lithium from one site to a neighboring vacant site. After a lithium hop, the solid typically undergoes a large number of vibrations before the same ion hops again. Between hops, there is therefore enough time for the lithium ion to thermalize whereby the momentum that the ion had during the hop is anharmonically dissipated to the rest of the crystal. This means that correlations between successive hops are negligibly small and diffusion can be modeled stochastically. A good approximation for the frequency with which lithium ions hop between adjacent sites is transition state theory [158] to be described in the next section.

As was demonstrated in previous chapters, the thermodynamic properties of Li_xCoO_2 are well characterized with a lattice model. Furthermore, the fact that diffusion can be viewed as discrete hops between adjacent equilibrium sites, with

hopping frequencies given by transition state theory, suggests that a lattice model is an appropriate tool to investigate lithium diffusion in Li_xCoO_2. Since diffusion in these systems is the result of a succession of discrete hops, it is useful to rewrite the expressions for D and D^* of the previous sections in terms of position $\vec{r}_i(t)$ as opposed to the velocities $\vec{v}_i(t)$. For D, this results in

$$D = \Theta D_J \tag{7.23}$$

where Θ is the thermodynamic factor of (7.7) and D_J, commonly referred to as the jump diffusion coefficient [159], is given by

$$D_J = \lim_{t\to\infty}\left[\frac{1}{2dt}\left\langle\frac{1}{N}\left(\sum_{i=1}^{N}\vec{r}_i(t)\right)^2\right\rangle\right] \tag{7.24}$$

$\vec{r}_i(t)$ is the displacement of the i^{th} lithium ion after time t and d is the dimension of the lattice on which diffusion takes place. For lithium diffusion in the layered form of Li_xCoO_2, d=2.

In a similar way, the self-diffusion coefficient becomes

$$D^* = \lim_{t\to\infty}\left[\frac{1}{2dt}\left(\frac{1}{N}\sum_{i=1}^{N}\left\langle[\vec{r}_i(t)]^2\right\rangle\right)\right] \tag{7.25}$$

D^* differs from D_J in that it measures the square of the displacement of individual particles while the jump diffusion coefficient D_J is a measure of the displacement of the center of mass of all the diffusing lithium ions.

7.4 Transition state theory

The $\vec{r}_i(t)$ appearing in equations (7.24) and (7.25) for the i^{th} lithium ion are the result of individual hops between adjacent lithium sites in the MO_2 host. Along the migration path between these sites, the migrating ion passes through an activated state. The activated state is located at the maximum energy point along the minimum energy path between the end-points of the hop. The activation barrier ΔH_B is defined

as

$$\Delta H_B = H_A - H_i \tag{7.26}$$

where H_i is the enthalpy of the crystal in the initial state and H_A is the enthalpy of the crystal with lithium in the activated state. The frequency, Γ, with which a hop occurs is given within transition state theory [158, 160] as

$$\Gamma = \nu \exp\left(\frac{\Delta S}{k}\right) \exp\left(\frac{-\Delta H_B}{kT}\right) \tag{7.27}$$

ν is an effective frequency also called an *attempt frequency* and is given by

$$\nu = \sqrt{\frac{k_B T}{2\pi}} \left(\frac{L}{A}\right) \tag{7.28}$$

L and A are integration volumes around the saddle point and the initial equilibrium state. ΔS in (7.27) is the activation entropy and is related to the ratio of states at the activated state to that of the equilibrium state. It can be calculated as the logarithm of the ratio of two Boltzmann integrals [161]

$$\frac{\Delta S}{k_B} = \ln\left[\left(\frac{A}{L}\right) \frac{\int_L e^{-(H-H_B)/k_B T} dL}{\int_A e^{-H/k_B T} dA}\right] \tag{7.29}$$

In its most rigorous form, the enthalpy H in the above equation is a surface that depends on $3Q$ degrees of freedom where Q corresponds to the number of ions in the solid. The $3Q$ coordinates in phase space correspond to the position coordinates of the ions of the solid, normalized by the square root of their mass. The integration region L is a $3Q-1$ dimensional dividing 'surface' between the initial and final states of the hop and passes through the saddle point along the migration path. A is a $3Q$ dimensional 'volume' around the initial equilibrium state of the hop.

In the derivation of (7.27), several assumptions are made. As a first approximation, it is assumed that once a migrating ion originating from the initial state has reached the dividing surface L, it will continue to migrate to the final state. In reality, a fraction of the migrating ions that pass the dividing surface L will abort their

hop and return back to the initial state. Nevertheless, theoretical studies analyzing this have found that neglecting the aborted hops leads to only minor quantitative errors of several percent [162]. Within this approximation, the hopping rate Γ is then set proportional to the fraction of the total time that a migrating ion resides on the dividing surface multiplied by the rate at which the ion crosses the dividing surface L in the direction of the final state. Both the fractional probability of being at the dividing surface L and the rate of crossing the surface are calculated within classical statistical mechanics [158]. At high temperature, this latter approximation is sufficiently accurate, though it breaks down when quantum tunneling becomes important as can be the case for hydrogen diffusion.

Within the harmonic approximation, (7.27) can be written as [158]

$$\Gamma = \frac{\prod_i^{3Q} \nu_i}{\prod_j^{3Q-1} \nu_j'} \exp\left(\frac{-\Delta H_B}{kT}\right) \tag{7.30}$$

The prefactor of the exponential is a ratio of the products of the 3Q normal mode frequencies of the equilibrium initial state to the 3Q-1 normal modes of the activated state. Absent in the product of the denominator is the mode in the direction of the hop. (7.30) clearly shows that the prefactor of the exponential containing the activation barrier has the dimensions of a frequency. Furthermore, it suggests that this prefactor has a numerical value on the order of a vibrational frequency. Typically, the prefactor is taken to be of the order of 10^{13} Hz. Nevertheless, examples exist, such as the two dimensional diffusion on a Ge surface, where the prefactor was found from first principles to be around 10^{11} Hz [163].

7.5 Environment dependent activation barriers

In lithium transition metal oxides, Li_xMO_2, a large variety of lithium-vacancy arrangements occur. Both the H_A and H_i that determine the activation barrier according to (7.26) depend on the lithium vacancy configuration present at the time of a hop. In general, the enthalpies of the endpoints of a hop are not equal and the activation

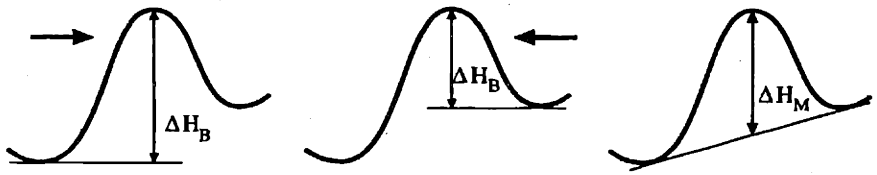

Figure 7-1: The activation barrier ΔH_B depends on the direction of the hop (indicated by the arrow). ΔH_M, however, is independent of the direction of the hop.

barrier seen from one endpoint will often differ from that seen from another endpoint (see Fig. 7-1). To enable comparison between activation barriers in different local environments, it is useful to introduce a mean activation barrier ΔH_M. A hop is characterized by at least two endpoints but could have $n > 2$ endpoints. We define the endpoints of a hop to be the sites around the activated state that must be vacant when a hopping ion is at the activated state and that are at the same time possible destination points for the hopping ion at the activated state. Defining H_{e_j} as the enthalpy of the crystal when the lithium ion is at endpoint j of the hop, we can formulate a mean activation barrier ΔH_M as

$$\Delta H_M = H_A - \frac{1}{n}\sum_{j=1}^{n} H_{e_j} \tag{7.31}$$

The enthalpy barrier that the migrating lithium ion experiences when hopping from one of the endpoints, say j=1, is then

$$\Delta H_B = \Delta H_M + \frac{1}{n}\sum_{j=1}^{n} H_{e_j} - H_{e_1} \tag{7.32}$$

ΔH_M is equal to ΔH_B when the enthalpies of the n-endpoints are all the same. When the enthalpies of the endpoints are not equal, ΔH_M reduces to the average of all the ΔH_B seen from each of the n endpoints of the hop.

Since the mean activation barrier ΔH_M are environment dependent, depending on the local lithium-vacancy environment around the activated state, it can be cluster

expanded. Such a cluster expansion should have the form

$$\Delta H_M = K_o + \sum_\alpha K_\alpha \phi_\alpha, \tag{7.33}$$

where ϕ_α are polynomials of occupation variables, and K_α are ECI describing the variation of the mean activation barrier with configuration. When a lithium ion is at the activated state, the n-endpoints of the hop are unoccupied. For a crystal with m lithium sites, the cluster expansion (7.33), therefore, extends over the $m-n$ lithium sites that do not overlap with the n-endpoints of the hop. It is reasonable to assume that (7.33) can be truncated after a cluster that extends beyond a maximal distance away from the hopping lithium ion, since the activation barrier is a local property. With a cluster expansion for the mean activation barrier ΔH_M in combination with a cluster expansion for the configurational enthalpy of the crystal (to calculate the end point enthalpies of the hop H_{e_j}), it is straightforward to calculate the activation barrier ΔH_B for any lithium-vacancy environment using (7.32).

The property ΔH_M being cluster expanded with (7.33) is different from the lithium-vacancy configurational enthalpy. ΔH_M is a local property while the enthalpy of the crystal is a global property of the whole solid. The relevance of this distinction manifests itself in how symmetry is used in simplifying the cluster expansion. Instead of using the space group symmetry operations of the crystal (as is done for a global cluster expansion , see chapter 2), the local cluster expansion (7.33) is to be simplified using the point group symmetry operations that simultaneously belong to the space group of the crystal and which map the figure of n-endpoints on itself. To our knowledge, this is the first time that a local cluster expansion has been proposed to parameterize the configuration dependence of the activation barrier.

The exponential prefactor of (7.27) also depends on the local environment. This quantity can, therefore, also be characterized with a combination of global and local cluster expansions. Nevertheless, the prefactor is expected to be less sensitive to variations in local environment than the exponential of the activation barrier. In this thesis, we neglect the configuration dependence of the prefactor.

Several methods exist for finding the activated state and its enthalpy H_A from first principles. These typically make use of a large supercell such that conventional first principles methods for periodic systems can be implemented. In this thesis, we have used two approaches to obtain information about the activation barriers in Li_xCoO_2. The first is called the elastic band method which enables the determination of the minimum enthalpy path between two energetically stable endpoints [164]. In this method, a discretized path of on the order of 8 replicas of the system is generated by linear interpolation between the initial and final states of the path. A global minimization is then performed with respect to ionic positions in each replica whereby the coordinates of each replica are connected to those of its neighboring replicas in the interpolation sequence by a spring. The working of the algorithm can be compared to the tightening of an elastic band across a saddle point between two minima of the enthalpy landscape.

The elastic band method is useful to identify the migration path and the location of the activated state. Nevertheless, to obtain an accurate approximation of the enthalpy at the activated state, a large number of replicas are needed. In many cases, the activated state is located at a high symmetry point between the endpoints and a calculation of the activation barrier can be performed with the hopping lithium ion initially placed at the high symmetry point. During minimization of the enthalpy of the supercell, the lithium ion will remain at the high symmetry position and the resulting minimum enthalpy will give the best approximation of the activation barrier within the supercell approach.

Calculating the prefactor in either (7.27) or (7.30) from first principles is considerably more complicated than a calculation of H_A. The prefactor in (7.27) depends on the detailed structure of the enthalpy surface around both the initial equilibrium site of the hop and the activated site. The prefactor in the harmonic approximation (7.30) requires a knowledge of the vibrational frequencies both at the equilibrium and activated states. First principles calculations of prefactors have been performed in ref [161, 165, 166, 163].

7.6 Kinetic Monte Carlo simulations

The kinetic Monte Carlo method enables an explicit simulation of the migration of a collection of lithium ions within the CoO_2 host. Individual hops occur with relative probabilities given by the jump frequency of (7.27). Using first principles cluster expansions to parameterize first principles activation barriers ΔH_B of (7.27), this approach can be expected to yield an accurate description of lithium diffusion in Li_xCoO_2.

The basic algorithm implemented in this work can be summarized as follows [167]. At fixed lithium concentration and temperature, the simulation starts with a typical lithium-vacancy arrangement exhibiting the equilibrium state of short-range or long-range order. These initial configurations are typically obtained with standard equilibrium Monte Carlo techniques in the canonical or grand canonical ensemble using the cluster expansion for the configurational enthalpy. The kinetic Monte Carlo simulation then consists of the repetition of three steps [167]. (i) First, all possible migration probabilities Γ_m are determined where m scans the collection of migration paths available to the different lithium ions. Γ_m is zero if the endpoints of migration path m are simultaneously occupied by lithium. When this is not the case, Γ_m is calculated with the hop frequency of (7.27). (ii) In the second step, a random number ρ of the interval (0,1) is sampled. The migration event k is chosen such that

$$\frac{1}{\Gamma_{tot}} \sum_{m=1}^{k-1} \Gamma_m < \rho \leq \frac{1}{\Gamma_{tot}} \sum_{m=1}^{k} \Gamma_m \tag{7.34}$$

where Γ_{tot} is the sum of all individual probabilities Γ_m. This ensures that each event m occurs with probability Γ_m/Γ_{tot}. The third step (iii) consists of an update of the time Δt leading up to the hop of step (ii). This time is given by

$$\Delta t = -\frac{1}{\Gamma_{tot}} \log \zeta \tag{7.35}$$

with ζ a random number from (0,1).

We define a kinetic Monte Carlo step as the repetition of steps (i)-(iii) as many

times as there are lithium ions in the simulation. To obtain adequate averages for D_J and D^*, of the order of 25-50 initial equilibrium states should be considered at each temperature and concentration. Time averages of the different diffusion coefficients can be performed as described in ref[168].

Bulnes *et. al.* [167] demonstrated theoretically as well as with a numerical comparison, that the above kinetic Monte Carlo algorithm is equivalent with the dynamic Monte Carlo algorithm commonly implemented in diffusion studies of lattice models [169, 159, 170]. The advantage of the above algorithm is that a lithium hop occurs during every sequence of steps (i)-(iii). This is especially advantageous for systems with strongly varying activation barriers.

7.7 Summary

In this chapter, we have reviewed the foundations of the Kubo-Green equations for diffusion. Kubo-Green like equations rest on the dissipation-fluctuation theorem. They relate kinetic coefficients describing macroscopic dissipative processes such as diffusion to microscopic fluctuations at thermodynamic equilibrium.

We have also presented a computational scheme that enables the first principles calculation of the diffusion coefficient in a system with configurational disorder. This approach approximates individual hops with transition state theory and describes the configuration dependence of the activation barrier ΔH_B with a combination of a total enthalpy cluster expansion and a local cluster expansion for the mean activation barrier ΔH_M defined by (7.31). The cluster expansions are parameterized with first principles total energy calculations of the relevant quantities. The macroscopic diffusion coefficients are then determined by calculating the Kubo-Green equations with kinetic Monte Carlo simulations.

Chapter 8

Theory of Li diffusion in Li_xCoO_2

The power density of a battery is in part determined by the diffusivity of the lithium ions within the metal oxide host structure. To optimize power density, therefore, a clear understanding of the lithium diffusion mechanisms within the MO_2 host is necessary. In this chapter, we implement the formalism of the previous chapter to investigate lithium diffusion in the O3 form of Li_xCoO_2 from first principles [171]. The results of this study are also of value to elucidate the lithium diffusion mechanisms in other layered compounds such as Li_xNiO_2 or Li_xMnO_2 since the symmetry of the host structure plays a dominant role in determining the lithium migration mechanisms.

As a first step to studying diffusion, we focus on the possible migration paths for lithium diffusion with LDA pseudopotential calculations (section 8.1). These calculations indicate that the migration path as well as the activation barrier has a strong dependence on the local lithium-vacancy arrangement around the migrating lithium ion. In section 8.2 a local cluster expansion is constructed to parameterize the configuration dependence of the activation barriers. In section 8.3, the local cluster expansion is implemented in kinetic Monte Carlo simulations from which diffusion mechanisms are determined and kinetic parameters such as the diffusion coefficient are calculated. The results are interpreted and compared with experiment in section 8.4.

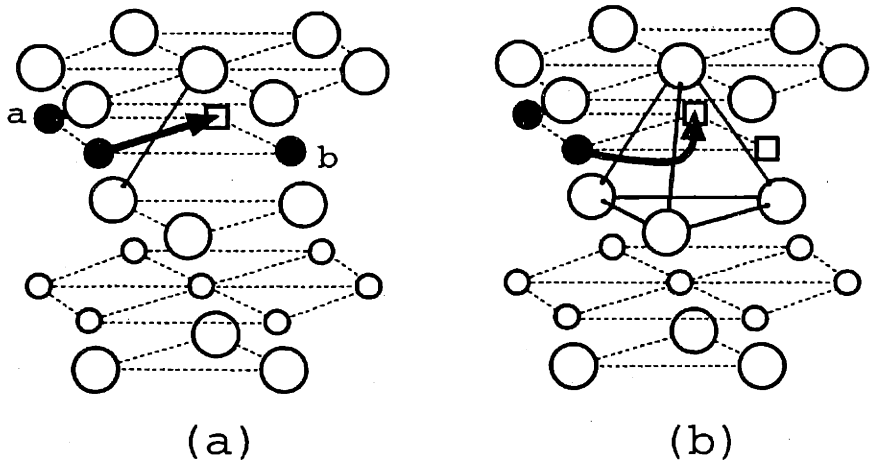

Figure 8-1: Two different migration paths for lithium exist in Li_xCoO_2 depending on the local environment. (a) The oxygen dumbbell hop (ODH) occurs when sites a and b are occupied. (b) The tetrahedral site hop (TSH) occurs when at least one site adjacent to the endpoint of the hop is vacant. Large circles are oxygen, filled circles are lithium, squares are lithium vacancies and small empty circles are cobalt.

8.1 First principles activation barriers

In this section, we present the results of an investigation of the dependence of the activation barrier on the lithium-vacancy arrangement. We find that two qualitatively different hopping mechanisms exist depending on the immediate local environment around the endpoints of the hop. These are illustrated in Fig. 8-1 (a) and (b). The first hopping mechanism occurs when the two lithium sites (sites a and b in Fig. 8-1(a)) immediately adjacent to the endpoints of the hop are simultaneously occupied by lithium ions. The diffusing lithium ion then migrates along a path that closely follows the shortest path connecting the initial site of the hop and the vacancy. This shortest path, denoted by the arrow in Fig. 8-1(a), passes through a dumbbell of oxygen ions. We refer to this migration path as an oxygen dumbbell hop (ODH). This is the mechanism by which isolated vacancies exchange with lithium. When either one or both of the sites immediately adjacent to the endpoints of the hop are vacant, lithium migrates along a curved path which passes through a tetrahedral site as illustrated in Fig. 8-1(b). Notice that for this migration mechanism to occur, the destination of the hopping lithium ion must be part of a divacancy (it could also be

$\vec{A}$	4.0	2.0	0.0
$\vec{B}$	-2.0	2.0	0.0
$\vec{C}$	0.333	1.666	0.333

Table 8.1: The $\vec{A}$,$\vec{B}$ and $\vec{C}$ cell vectors of the supercell in which the activation barriers were calculated. The vectors are expressed in terms of the conventional hexagonal setting of the O3 layered crystal structure

part of a cluster of vacancies containing more than two vacancies). We refer to this migration mechanism as a tetrahedral site hop (TSH).

In the following sections 8.1.1-8.1.4, we describe first principles elastic band calculations that form the basis of the above picture of lithium migration in Li_xCoO_2. Energies of activated states were calculated in supercells of Li_xCoO_2 containing 12 Li_xCoO_2 formula units. The number of ions in this supercell ranges between 47 to 37 depending on the lithium concentration (which was varied between x=11/12 to x=1/12). The $\vec{A}$ and $\vec{B}$ axes of the supercell form a $2\sqrt{3} \times 2\sqrt{3}$ two dimensional superlattice in terms of the basal plane vectors $\vec{a}$ and $\vec{b}$ of the hexagonal unit cell of Li_xCoO_2. The $\vec{C}$ axis of the supercell connects adjacent lithium planes and was chosen to be as shallow as possible to maximize the distance between the periodic images of the hopping lithium ions in adjacent lithium planes. The coordinates of the supercell vectors in terms of the hexagonal unit cell vectors of Li_xCoO_2 are listed in table 8.1. Calculations of activation barriers were also performed in a 16 Li_xCoO_2 formula unit supercell to test the degree of convergence of the results obtained with the 12 formula unit supercell. In all supercell calculations, we used a $2 \times 2 \times 2$ k-point mesh which is equivalent to 8 irreducible k-points.

8.1.1 Migration of a vacancy in $LiCoO_2$

Insight about hopping mechanisms can be obtained by investigating lithium migration in the dilute extremes of lithium concentration. One dilute extreme is migration of a single vacancy in an otherwise fully lithiated Li_xCoO_2 host. Fig. 8-2(a) illustrates a projection of a lithium plane. With the pseudopotential method in combination with the elastic band method, we find that a lowest energy migration path between

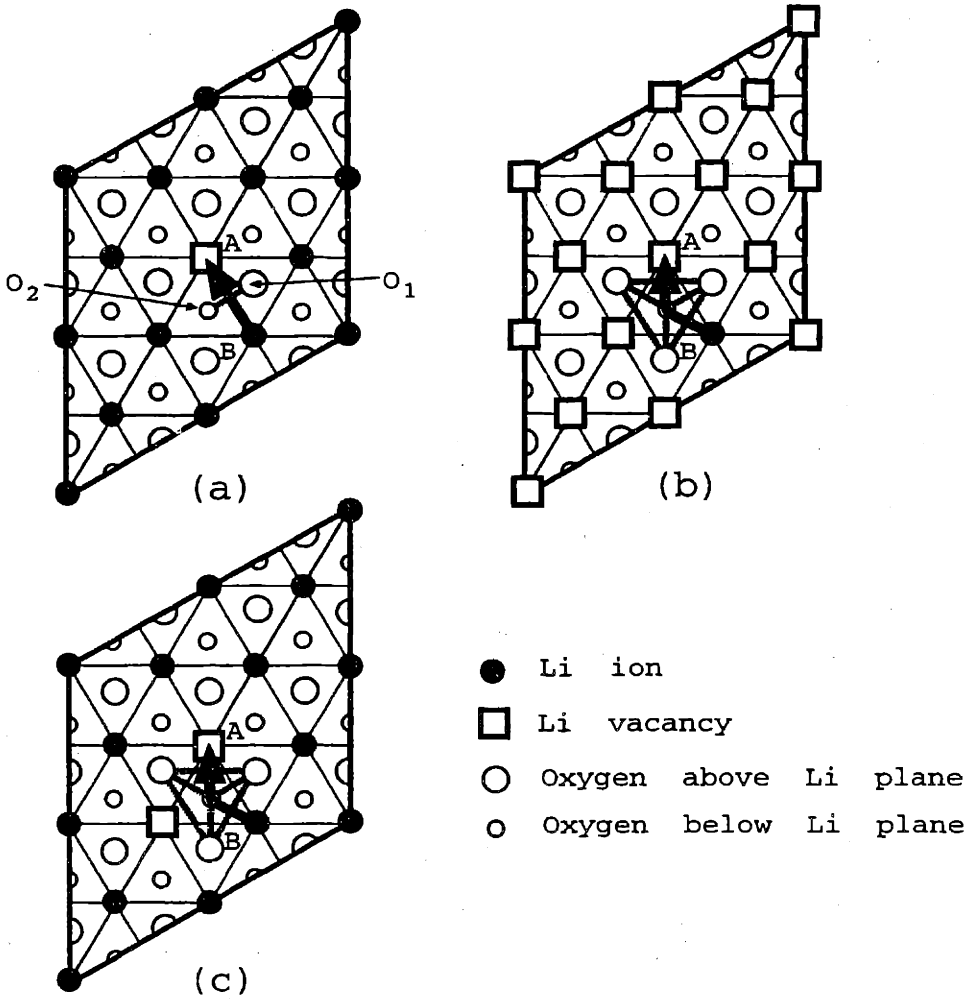

Figure 8-2: Lithium migration paths in Li_xCoO_2 determined with the elastic band method. The triangular lattice corresponds to the lithium sites and the filled circles are lithium ions. The large empty circles are oxygen ions above the lithium plane and the small empty circles are oxygen ions below the lithium plane. See text for discussion.

adjacent octahedral sites closely follows the arrow A-B of Fig. 8-2(a). Although the arrow A-B of Fig. 8-2(a) forms a straight line connecting adjacent octahedral sites, the actual migration path is slightly curved, but passes very close to the center of the oxygen dumbbell formed by the oxygen ions O_1 and O_2. In fact, we find that the saddle point for dilute vacancy migration is predicted to be 0.25 Å away from the center of the oxygen dumbbell (directed towards either one of the adjacent tetrahedral sites) and 0.8 Å away from the closest adjacent tetrahedral site. Because of this, we will refer to this migration path as an Oxygen Dumbbell Hop (ODH). The activation barrier for the ODH is predicted to be 830 meV and the enthalpy along this path is illustrated in Fig. 8-3(a).

The enthalpy of the migrating lithium ion placed exactly at the center of the oxygen dumbbell (between O_1 and O_2 of Fig. 8-2) is only 10 meV higher than at the true activated state which is slightly shifted towards an adjacent tetrahedral site. This suggests that a reasonable approximation for the activation barrier for the ODH can be obtained by assuming the activated state to be exactly at the center of the oxygen dumbbell hop.

8.1.2 Migration of isolated lithium in dilute Li_xCoO_2

Another dilute extreme is the migration of an isolated lithium ion between two octahedral sites in an otherwise vacant lithium plane of CoO_2. A calculation with the elastic band method shows that the lowest energy path between adjacent octahedral sites is along the arrow with endpoints A-B of Fig. 8-2(b). As is evident from Fig. 8-2(b), this migration path passes through an adjacent tetrahedral site making this a tetrahedral site hop (TSH). The energy along the TSH is illustrated in Fig. 8-3(b). The plot clearly shows that the activation barrier for migration of an isolated lithium ion is exactly at the tetrahedral site. The value of the activation barrier is 600 meV.

It is striking that the maximum along the TSH occurs at the center of the tetrahedral site, a relatively open space, instead of at the centers of the oxygen triangles forming the faces of the tetrahedral site. The explanation is electrostatic in origin. The tetrahedral site shares a face with an oxygen octahedra surrounding a Co ion.

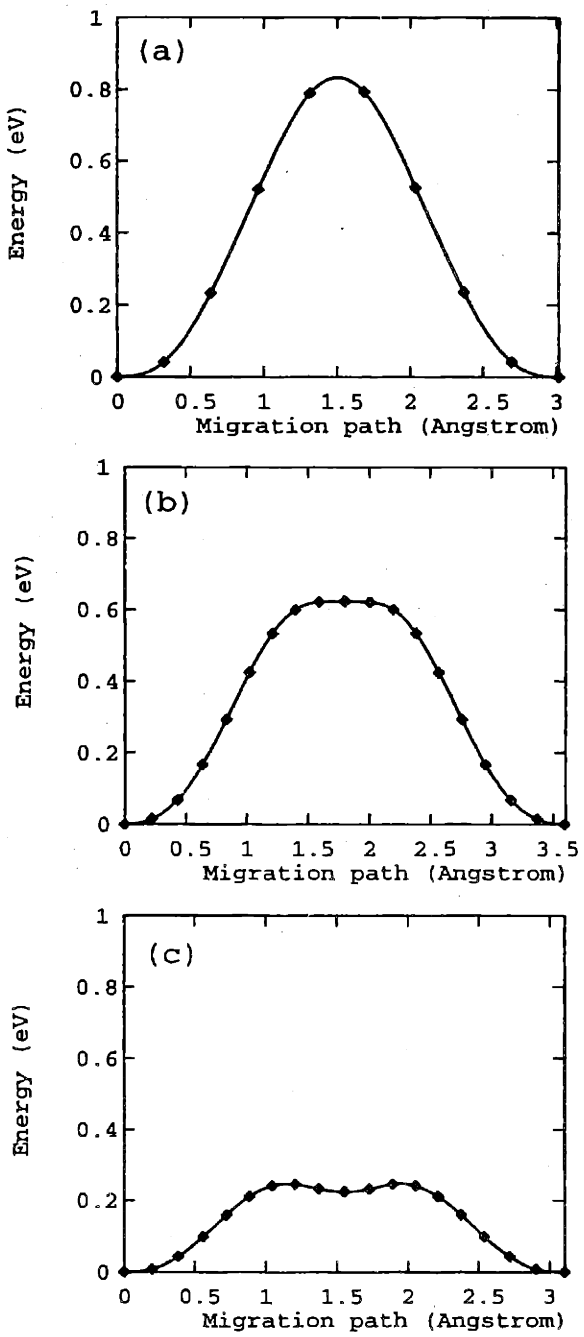

Figure 8-3: Energy along the migration path in different lithium-vacancy environments determined with the elastic band method. Refer to Fig. 8-2 for the corresponding lithium-vacancy environments. (a) Migration of an isolated vacancy at x=11/12. (b) Migration of an isolated lithium according to a TSH at x=1/12 (c) Migration of a lithium ion into a divacancy according to a TSH at x=10/12.

The large electrostatic repulsion between lithium and the positively charged Co ion energetically penalizes the position at the center of the tetrahedron. This is manifested by the prediction that the saddle point at the tetrahedral site is displaced 0.4 Å from the ideal position of the tetrahedral site in a direction away from the cobalt ion and towards one of the oxygen ions forming the tetrahedron. As a result, three lithium-oxygen bonds have a distance of 1.85 Å while the fourth lithium-oxygen bond has a distance of 1.53 Å.

The qualitative difference between the TSH and the ODH can be attributed to the absence or presence of lithium ions simultaneously neighboring both endpoints of the hop. In the latter case, the electrostatic repulsions due to the lithium ions adjacent to the endpoints of the hop displace the saddle point away from the tetrahedral site towards a position almost at the center of the oxygen dumbbell.

8.1.3 Migration in an intermediate environment

At non-dilute lithium concentrations, local arrangements will occur that are intermediate to those of the two dilute extremes. Fig. 8-2(c), illustrates a particular arrangement around a hopping lithium ion that has features of the two dilute cases treated in sections 8.1.1 and 8.1.2: one lithium site that simultaneously neighbors both endpoints of the hop is occupied, while the other lithium site is empty. Applying the elastic band method to this intermediate arrangement, we find that the migration path follows the arrow A-B of Fig. 8-2(c). This path passes through the tetrahedral site and can therefore be called a TSH.

Despite also passing through a tetrahedral site, the energetics of this migration path exhibits a subtle difference with the TSH for an isolated lithium ion in an empty CoO_2 host (section 8.1.2). The energy along the path A-B of Fig. 8-2(c) is illustrated in Fig. 8-3(c). The tetrahedral site is no longer a maximum along the migration path, but a weak minimum. The activated state has shifted to a position closer to the center of the triangle of oxygen ions that form the face between the tetrahedral site and octahedral site. The barrier, however, is only about 25 meV higher than the energy of lithium at the tetrahedral site.

The difference between the energetics of the TSH of Fig. 8-2(b) and Fig. 8-2(c), is a result of a difference in the overall lithium concentration. The TSH of Fig. 8-2(c) occurs at high Li concentration (within the supercell, x=0.8333) while that of Fig. 8-2(b) occurs at very low lithium concentration. As was shown in chapter 3, as more lithium is added to the CoO_2 host, the charge donated by lithium to the host is transferred to the oxygen ions. The increased negative charge on the oxygen ions at high lithium concentration screens the electrostatic repulsion between the cobalt and the lithium at the tetrahedral site. This is qualitatively equivalent to saying that the effective charge on cobalt at high lithium concentration is +3 while at low x it is closer to +4. The electrostatic repulsion between cobalt and a lithium in a tetrahedral site therefore increases with decreasing lithium concentration.

8.1.4 General configuration dependence of Activation barrier

The above results allow us to distinguish between two different migration mechanisms, the TSH and the ODH. Whether or not a TSH or ODH mechanism can occur depends on the lithium-vacancy arrangement in the immediate environment of the hopping lithium. If the two lithium sites that simultaneously neighbor the endpoints of the hop are occupied, lithium migration will occur according to an ODH mechanism. If both lithium sites adjacent to the hop are vacant, lithium will then migrate along one of the two TSH paths. And finally, if only one of the adjacent lithium sites are occupied, lithium migration will occur along the TSH passing by the empty lithium site.

Not only does the hopping mechanism depend on the local environment, but the value of the activation barrier for a given hopping mechanism will also depend on the surrounding lithium-vacancy arrangement. To determine this dependence, we have calculated the activation barriers at several lithium concentrations and in different local lithium-vacancy arrangements. Fig. 8-4 illustrates the mean activation barriers ΔE_M as defined by (7.31) at different lithium concentrations and local environments. The squares correspond to TSH activation barriers and the filled circles correspond to ODH activation barriers. Note that for the TSH, the number of endpoints n of the

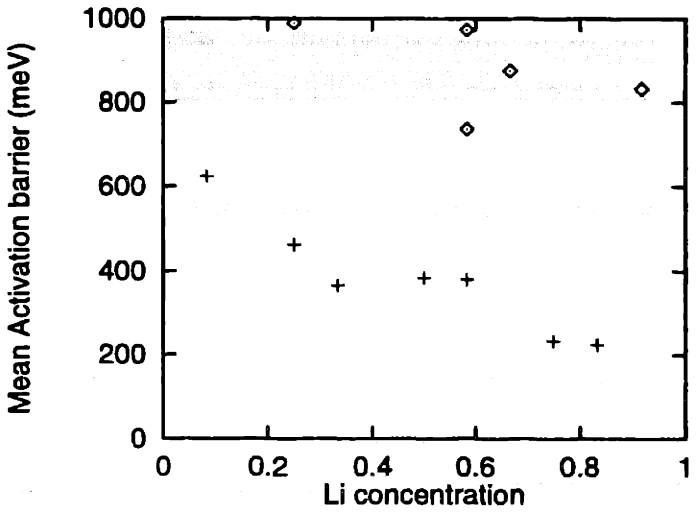

Figure 8-4: Values for ΔH_M at different lithium concentrations and arrangements in the O3 form of Li_xCoO_2. Crosses correspond to TSH's and the diamonds correspond to ODH's.

hop appearing in (7.31) is 3 and for the ODH n is equal to 2.

In the calculation of the mean activation barriers ΔE_M for the TSH's, E_A of (7.31) was set equal to the energy of lithium in the tetrahedral site along the TSH path. While for low lithium concentration, this approach yields the exact activation barrier (within the limit of the supercell method), for higher lithium concentrations, it leads to an approximation since the activated state is slightly shifted away from the tetrahedral site at high x (see section 8.1.3). Nevertheless, as is clear in Fig. 8-3(c), the error is at most of the order of 25 meV or 10% for the TSH activation barrier at x=0.8333. For the ODH's, E_A of (7.31) was set equal to the energy of the hopping lithium ion placed exactly at the center of the oxygen dumbbell. Although the actual saddle points for the ODH are slightly shifted away from the center of the oxygen dumbbell in a direction perpendicular to the hop direction, we found that the error of this approximation is of the order of 10 meV.

The calculated activation barriers of Fig. 8-4 convey two major trends. First, the activation barriers for the ODH are almost twice as large as those of the TSH. This is not surprising, since the activated state of the ODH is sterically more constricted than that of the TSH. Furthermore, the ODH mechanism only occurs when the two lithium sites simultaneously neighboring the endpoints of the hop are occupied. The

electrostatic repulsion between these adjacent lithium ions and the hopping lithium ion constitutes an additional energetic penalty to the activated state which is absent in the TSH mechanism.

The second trend in Fig. 8-4 is the increase in the activation barrier for the TSH as the lithium concentration is reduced. The activation barriers for the TSH vary relatively little at intermediate lithium concentration, however, at low lithium concentration, the TSH activation barrier increases by a significant amount. This increase is caused by the large contraction of the lattice parameter, c, of the CoO_2 host frame work below x=0.3, a phenomenon that has both been measured experimentally [49, 45] as well as been predicted from first principles [116] (see chapter 4). The contraction is accompanied by a reduction in the distance between the oxygen planes adjacent to the lithium planes which in turn causes a contraction of the tetrahedral site. To expose the role of the lattice paramter, c, on the activation barrier, we artificially constrained the c for the structure at x=0.0833 to have a value typical of that in the concentration range of x=0.3 and 0.6 and recalculated the activation barrier. The activation barrier decreases to approximately 450 meV which is of the order of the activation barriers obtained at intermediate lithium concentration.

The general decrease in activation barrier with increasing x above x=0.5 cannot be attributed to a variation in c since it is more or less constant in this concentration range. Instead it can be traced to an improvement with increasing x in the screening of the electrostatic repulsion between the lithium in the tetrahedral site and a cobalt ion in an adjacent face sharing octahedral site as a result of the charge transfer to oxygen. This tends to make the energy of a lithium ion at the tetrahedral site energetically less unfavorable than at low lithium concentration.

To obtain an estimate of the supercell convergence error for the activation barriers, we calculated the activation barriers for the TSH at x=1/2 and the ODH at infinite vacancy dilution in a supercell containing 16 Li_xCoO_2 formula units. For the TSH, we found that the activation barrier changes by approximately 50 meV. For the ODH at infinite vacancy dilution, we found that the activation barrier changes by approximately 100 meV. This suggests that the accuracy of the TSH activation

barriers is better than that of the ODH.

8.2 Local cluster expansion of activation barriers

Many more possible local arrangements around a migrating lithium ion exist than were considered in the previous section. With the above activation barriers, we can parameterize a local cluster expansion that will enable us to approximate the activation barriers for other local environments.

The TSH and ODH mechanisms, which occur in different environments are characterized by distinct features; the two mechanisms have a different number of endpoints and the values of their respective activation barriers differ by a factor of two. It is therefore natural that the activation barriers of both mechanisms cannot be parameterized with the same cluster expansion.

In the present study, we constructed a cluster expansion for the activation barriers of the TSH. Since the activation barriers of the ODH are much larger than those of the TSH, the former mechanism will only prevail when the number of available TSH's are negligible. This, as is borne out by kinetic Monte Carlo simulations presented in the next section, only occurs at very dilute vacancy concentrations, where the divacancy concentration becomes negligible. In this regime, there is essentially one local configuration in the immediate vicinity of the the ion undergoing an ODH, namely all lithium sites occupied. The activation barrier for the ODH can then be approximated by a single value, *i.e.* that calculated in the limit of dilute vacancy concentration.

A local cluster expansion containing five ECI was constructed for the mean activation barriers of the TSH. The ECI were determined by performing a least squares fit to the seven TSH activation barriers illustrated in Fig. 8-4. The root mean square error between the seven activation barriers calculated with the cluster expansion and the values obtained with the pseudopotential method is 25 meV, a value which is of the order of 3 to 10% of the activation barriers. The clusters used in the expansion are illustrated in Fig. 8-5 and consist of the empty cluster, the nearest and next

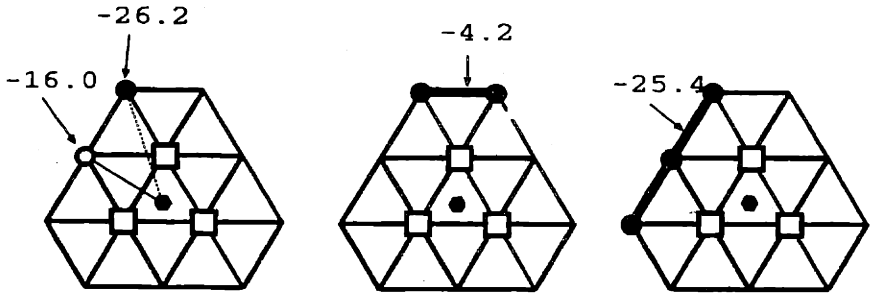

Figure 8-5: Local cluster expansion of the mean activation barrier ΔH_M for the TSH mechanism. The triangular lattice corresponds to lithium sites, and the squares correspond to the endpoints of the hop which are vacant when lithium is at the activated state.

nearest neighbor point clusters, a pair cluster and a triplet cluster.

8.3 Calculated diffusion coefficients and related properties

Although knowledge of the different hopping mechanisms and their corresponding activation barriers is an essential ingredient in the calculation of the lithium diffusion coefficient, it is not sufficient. The diffusion coefficient also reflects the degree of correlation between the hopping lithium ions. This correlation is both thermodynamic, as manifested by the degree of short or long range order, as well as dynamic and can be captured simultaneously with Kinetic Monte Carlo simulations.

In the kinetic Monte Carlo simulations, the activation barriers ΔH_B appearing in the hop frequencies Γ_j (7.27) were calculated with first principles cluster expansions. The cluster expansion for the O3 host was used to calculate H_{e_j} of (7.32), which represent the configurational energies of the endpoints of the hop. For the TSH mechanism, ΔH_M was calculated with the local cluster expansion discussed in the previous section. For the ODH, ΔH_M was set equal to 830 meV, the calculated activation barrier for the ODH in the dilute vacancy concentration limit. The true activation barriers for each hop ΔH_B were then calculated using the H_{e_j} and ΔH_M with (7.32).

The prefactor in the expression for Γ (7.27),

$$\nu^* = \nu \exp(\Delta S/k) \tag{8.1}$$

sets the time scale in the kinetic Monte Carlo simulations. Although the prefactor has a configurational dependence, this dependence is likely to be negligible in comparison with the configurational dependence of the exponent of the activation barrier $\exp(-\Delta H_B/kT)$. Therefore, for all hops in the kinetic Monte Carlo simulations simulations, we assumed a constant prefactor. Typically, the prefactor ν^* is on the order of 10^{13} sec^{-1}, however, a first principles investigation of two-dimensional diffusion on germanium surfaces [166] has indicated that ν^* can be on the order of 10^{11} sec^{-1}. Since in this work, no attempt has been made to quantitatively determine prefactors for lithium diffusion in Li_xCoO_2, we plot $\frac{10^{13}}{\nu^*}D$. This quantity should correspond to the true values for D within one to two orders of magnitude.

8.3.1 Diffusion coefficients

Fig. 8-6 (a) and (b) show calculated values for the diffusion coefficients D_J and D^* at 300 K and 400 K as determined from kinetic Monte Carlo simulations. It is clear that the diffusion coefficients vary within several orders of magnitude with lithium concentration. At high lithium concentration, the diffusion coefficients are very low, increasing by more than two orders of magnitude as the lithium concentration x is reduced to approximately 0.6. For small x, the diffusion coefficients are again very low. The significant dips in D_J and D^* around x=1/3 and x=1/2 at 300 K and around x=1/2 at 400 K are the result of lithium ordering appearing in the calculated phase diagram for the O3 form of Li_xCoO_2 (see chapter 4). Notice that D_J and D^* have the same order of magnitude yet they do not equal each other.

The chemical diffusion coefficient D which determines macroscopic diffusion as defined by Fick's law (7.5) and (7.6) is equal to the product of D_J with the thermodynamic factor Θ given by (7.7). Fig. 8-7 illustrates the thermodynamic factor for the O3 form of Li_xCoO_2 at 300 K. The thermodynamic factor becomes large around or-

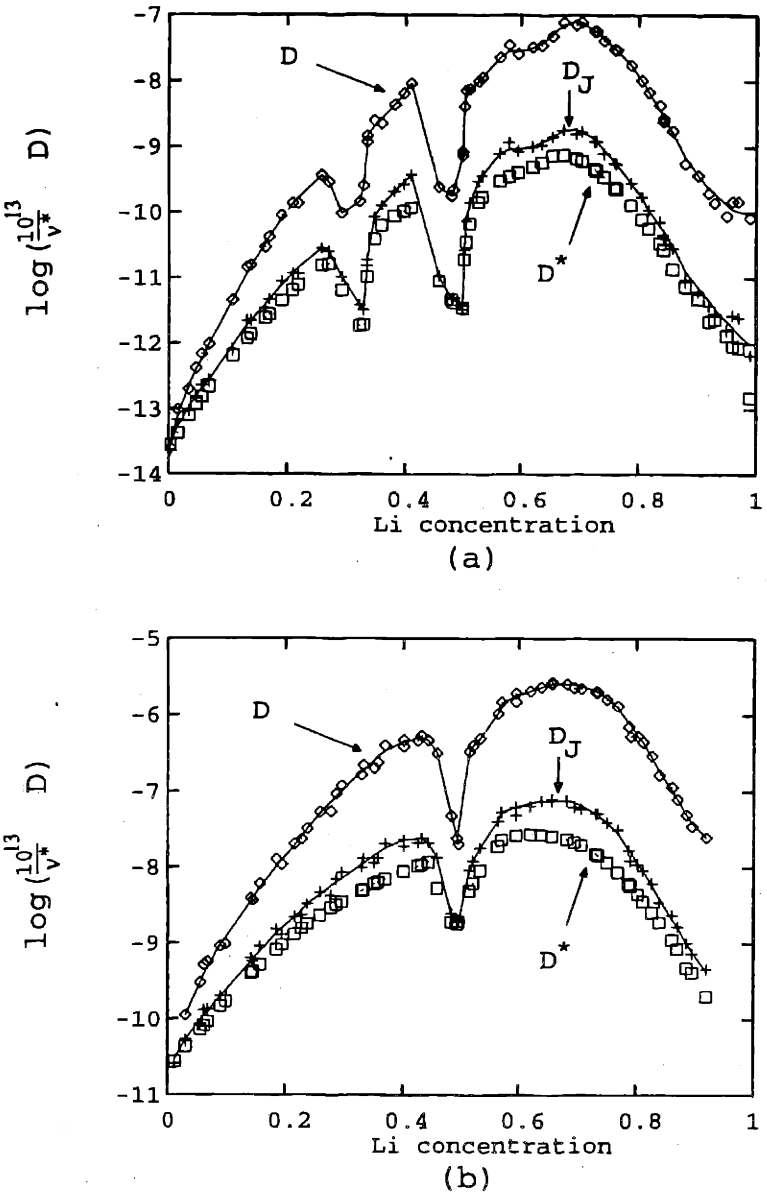

Figure 8-6: Calculated lithium diffusion coefficients for Li_xCoO_2 at (a) 300 K and (b) 400 K. Because of the uncertainty in ν^* of eqn. (8.1) we plot $(10^{13}/\nu^*)D$ where D is either D, D_J or D^* and is expressed in cm^2/s.

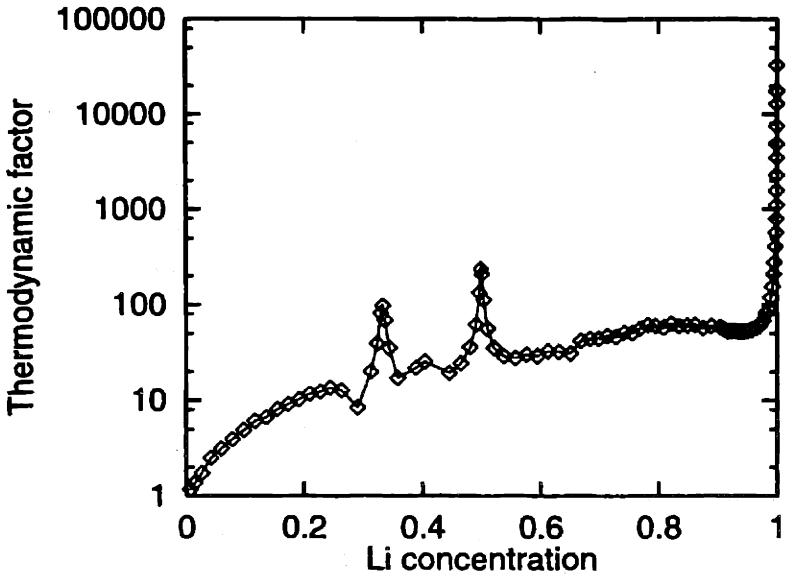

Figure 8-7: The calculated thermodynamic factor Θ at 300 K. Θ measures the deviation from ideality of the system and is given by eqn. 7.7.

dered phases and at the stoichiometric composition of Li_xCoO_2. Multiplying D_J with the thermodynamic factor Θ yields the chemical diffusion coefficient D illustrated in Fig. 8-6.

8.3.2 Microscopic hopping behavior

In the kinetic Monte Carlo simulations, both the TSH and ODH mechanisms are considered. The frequency with which either hop mechanism occurs is proportional to the availability of the particular mechanism multiplied by the exponent of the activation barrier divided by kT. Fig. 8-8 illustrates the average availability of TSH and ODH mechanisms per lithium ion as a function of lithium concentration. Also illustrated is the average number of vacancies adjacent to lithium ions normalized per lithium ion. At low x, the availability of TSH's is high while that of ODH's is very low. Above about x=0.65, however, the number of candidate ODH paths accessible to each lithium increases and exceeds the availability of TSH paths. The TSH mechanism requires at least a divacancy adjacent to the hopping lithium ion and at high lithium concentration, the concentration of divacancies is less than the concentration of single vacancies. In fact, if the lithium ions and vacancies are randomly distributed,

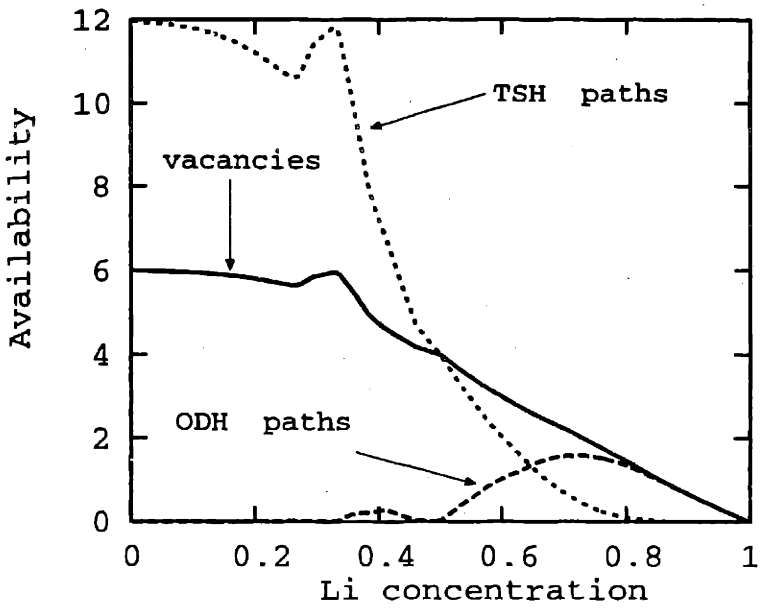

Figure 8-8: The average availability of TSH pathways, ODH pathways and vacancies per lithium ion as a function of lithium concentration.

the concentration of divacancies scales as $(1-x)^2$ while that of single vacancies as $(1-x)$. Since vacancies repel each other as x approaches 1, the concentration of divacancies is even lower than $(1-x)^2$ in Li_xCoO_2. The cross-over in the availability of TSH paths versus ODH paths suggests that at low lithium concentration, the TSH mechanism should dominate and at sufficiently high lithium concentration the ODH mechanism should dominate. Nevertheless, since the typical activation barrier for the TSH mechanism is significantly lower than the ODH activation barriers, the Monte Carlo simulations predict that for $0 < x < 1$ the TSH mechanism dominates and that the ODH mechanism becomes important only at almost infinite vacancy dilution.

The average activation barrier $\langle \Delta H_B \rangle$ as experienced by hopping lithium ions in the kinetic Monte Carlo simulations is illustrated in Fig. 8-9. Since lithium ions hop according to the TSH mechanism between x=0 and 1, $\langle \Delta H_B \rangle$ naturally follows the same trend of the first principles values of ΔH_M of Fig. 8-4, *i.e.* increasing $\langle \Delta H_B \rangle$ with decreasing x.

The large variations in D with x (Fig. 8-6) are closely linked to the variation in activation barrier (Fig. 8-9) and availability (Fig. 8-8) of the TSH mechanism with

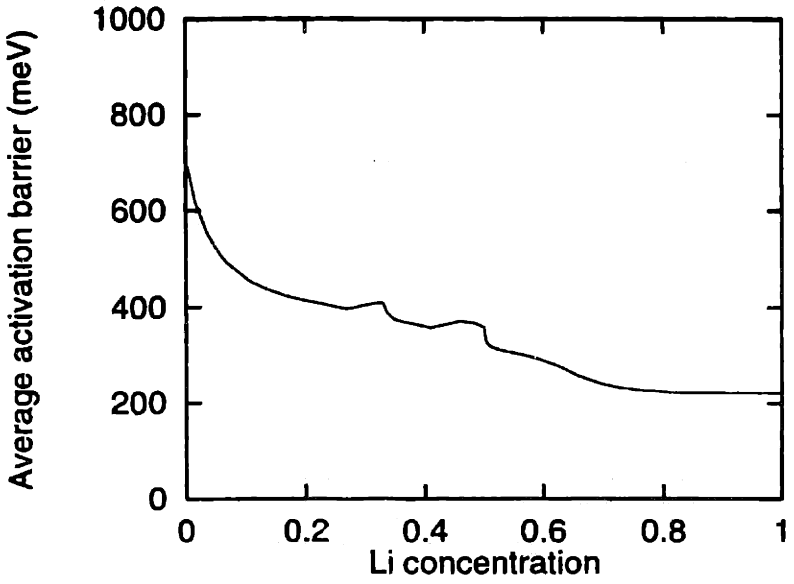

Figure 8-9: Variation with x of the average activation barrier overcome by hopping lithium ions in the kinetic Monte Carlo simulations.

x. At dilute x, the activation barrier is high resulting in a small diffusion coefficient. As x increases, the activation barrier progressively decreases producing an increase in the diffusion coefficient. The dips in diffusivity around x=1/3 and x=1/2 are a result of lithium ordering which from an energetic point of view tends to lock the lithium ions in their sublattice sites. Further increase of x above 1/2 results in a decrease in the diffusion coefficient, even though the average activation barrier levels off. This reduction of D is a result of a decline in the number of available vacancies to hop to in combination with an even more rapid decline in the average number of available TSH paths to enable lithium hops to neighboring vacancies.

8.3.3 Correlation factor

The prevalence of the TSH mechanism for most values of x has interesting implications concerning the correlated motion of the lithium ions. The above results indicate that reasonable diffusion rates in layered Li_xCoO_2 are mediated through clusters of divacancies since they enable lithium ions to hop according to the TSH mechanism. While at low lithium concentrations, divacancies are sufficiently abundent, at high x, clusters of vacancies are energetically and entropically less favored than a uniform

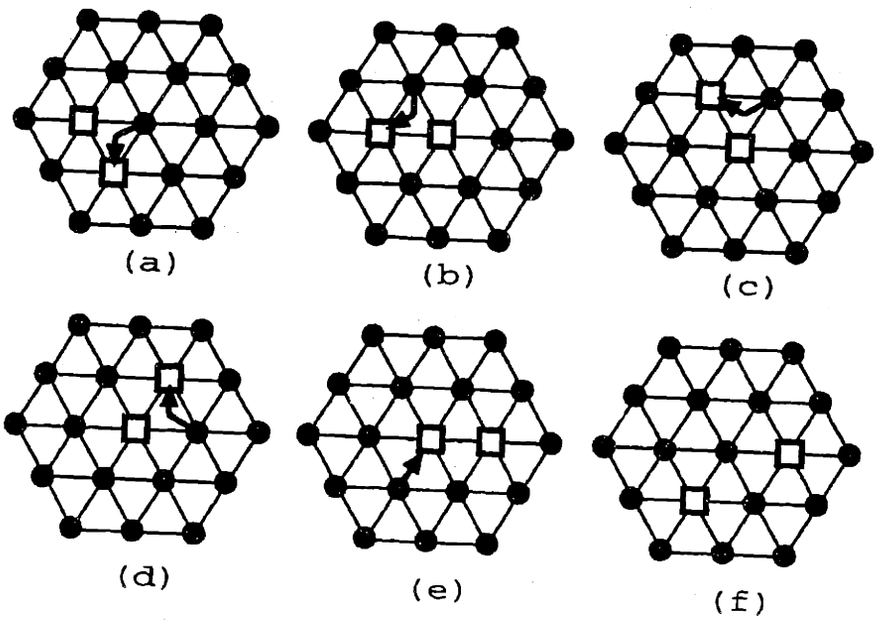

Figure 8-10: At high lithium concentration, lithium migration according to the TSH mechanism occurs through the cartwheel motion of a divacancy.

distribution of vacancies. Nevertheless, even for high x an overwhelming majority of lithium hops occur through divacancies.

To better understand the implications of divacancy diffusion, it is useful to consider the motion of an isolated divacancy. Fig. 8-10(a) illustrates a cluster of two vacancies surrounded by lithium ions in the immediate environment. Figs. 8-10(a)-(e) shows that the effect of lithium diffusion according to the TSH mechanism (as illustrated by the curved arrows), is to rotate the divacancy similar to the movement of a cartwheel. Only on rare occasions after the occurrence of an ODH do the vacancies of the divacancy cluster separate. The latter case is illustrated in Fig. 8-10(e)-(f) and has a very low probability of occurrence due to the high activation barrier associated with the ODH mechanism.

A measure of correlated motion is the correlation factor which is defined as

$$f = \frac{\langle \vec{r}(t)^2 \rangle}{\langle n(t) \rangle a^2} \tag{8.2}$$

where $\langle \vec{r}(t)^2 \rangle$ is the average distance squared that a lithium ion has travelled after time t, $\langle n(t) \rangle$ is the average number of hops that a lithium ion has performed in time

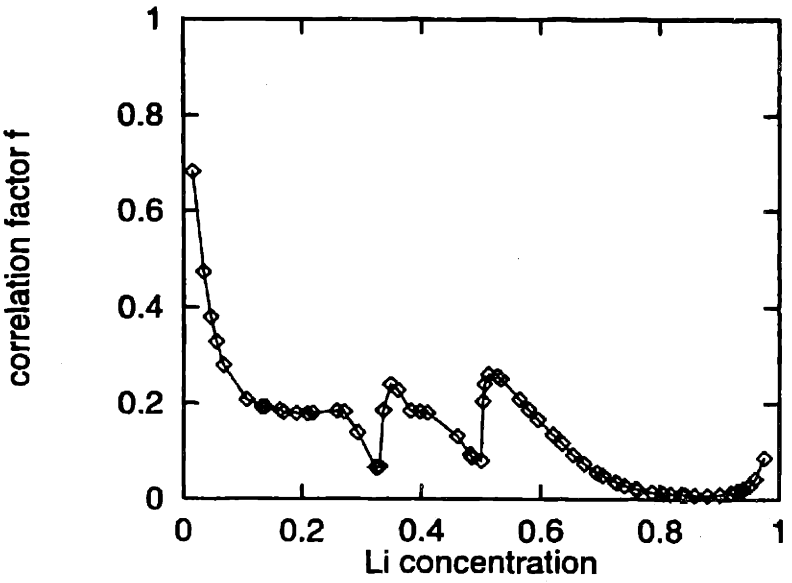

Figure 8-11: Calculated correlation factor as a function of lithium concentration.

t, and a is the distance between the endpoints of the hop. The correlation factor f measures the deviation of the lithium intrinsic diffusion coefficient D^* from that of an equal number of random walkers on a triangular lattice. When lithium migration is uncorrelated, the correlation factor equals one. This occurs as x approaches zero since the interactions among different lithium ions disappear and migration of isolated lithium ions becomes that of a random walk. As x approaches one, the motion of the isolated vacancies becomes that of a random walk, however, migration of the lithium ions does not. The theoretical value of f as x approaches one on a triangular lattice is around 2/3.

Fig. 8-11 illustrates the correlation factor for lithium diffusion in Li_xCoO_2 as a function of x at 300 K. Although f approaches the theoretical value in the dilute limit of x=0, at intermediate x, it deviates strongly from a linear interpolation between f=1 at x=0 and f=2/3 at x=1. In fact, as x approaches 1, f remains very low. Only once the ODH mechanism dominates at inifinite vacancy dilution whereby lithium exchanges with isolated vacancies will f approach the value of 2/3. Fig. 8-11 clearly illustrates that the TSH hop mechanism results in significant correlated motion of the lithium ions.

8.4 Discussion

The investigation of lithium diffusion with a combination of first principles LDA calculations and kinetic Monte Carlo simulations is made possible with the cluster expansion formalism. Although cluster expansions have been used extensively to describe the configurational energy of substitutional alloys, to our knowledge, this is the first example in which a local cluster expansion has been used to parameterize the configuration dependence of the activation barrier for migration.

The first principles pseudopotential calculations within the local density approximation have shown that two distinct hopping mechanisms exist for lithium migration in Li_xCoO_2. We have called these the oxygen dumbbell hop (ODH) and tetrahedral site hop (TSH) mechanisms. Whether a lithium ion hops according to the ODH or TSH mechanism depends on the local environment around the migrating ion. If the two lithium sites adjacent to the endpoints of the hop (sites a and b of Fig. 8-1 (a)) are occupied by lithium ions, the lithium ion migrates along the ODH path which approximates the shortest path between the endpoints of the hop. If at least one of the two lithium sites adjacent to the endpoints of the hop are vacant, lithium will migrate along the TSH path which passes through a tetrahedral site as illustrated in Fig. 8-1(b). This means that for the TSH mechanism to be possible, the lithium ion must migrate into a divacancy.

The ODH path is more constricted than the TSH path making the latter a sterically more attractive route. Nevertheless, when lithium ions occupy the two sites adjacent to the endpoints of the hop (sites a and b of Fig. 8-1(a)), their positive charge electrostatically repels the migrating lithium ion along a path that passes very close to the center of the oxygen dumbbell giving rise to the ODH mechanism. Consequently, the activation barrier for the ODH mechanism is more than twice as large as that for the TSH mechanism. The first principles calculations show that the activation barrier for the TSH mechanism has a strong dependence on concentration, increasing with decreasing x. As was explained in section 8.1.4, this increase is related to the sharp drop of the lattice parameter, c, below x=0.3 along with an increase in

the effective valence charge of cobalt with decreasing x.

Since the activation barrier for the TSH mechanism is significantly below that of the ODH, the kinetic Monte Carlo simulations predict that the TSH mechanism dominates over the whole concentration range x=0 and 1. This result is especially significant at high lithium concentration, as it requires that diffusion is mediated by the motion divacancies. It means that the decrease of the different diffusion coefficients at high x is more rapid than if diffusion occurred by exchanges with single vacancies with the same and constant activation barrier. Due to the large variation in activation barrier with x, the calculated diffusion coefficients vary within several orders of magnitude.

A hopping mechanism involving an adjacent tetrahedral site had already been conjectured from molecular dynamics simulations using empirical potentials [172]. The present systematic study of the environment dependence of the activation barriers using more realistic first principles calculations has shown that in fact two migration paths exist depending on the immediate environment. More importantly, the present study has shown that the migration path through the tetrahedral site will only occur if the end-point belongs to a divacancy. This is a significant constraint on the TSH mechanism, especially at high lithium concentration where the number of divacancies are severly limited, since, as was shown with kinetic Monte Carlo simulations, diffusion mediated by divacancies is very inefficient. The use of a first principles energy method for a system such as Li_xCoO_2 is essential as the subtle, but important, changes in electronic properties with lithium concentration and environment are extremely difficult, if not impossible to capture within an empirical potential frame-work typically used in Molecular Dynamics simulations.

Several sources of inaccuracies in the calculated activation barriers of this work can be identified that originate either from numerical errors or from approximations. Potential numerical inaccuracies arise from an inadequate k-point convergence and the use of a supercell in the calculation of the activation barriers. We estimate these errors to be of the order of 50 meV for the most important activation barriers (*i.e.* those for the TSH mechanism). Nevertheless, since the same supercell and k-point

mesh was used in the calculation of all activation barriers we expect this to be a systematic error. Another inaccuracy occurs at high lithium concentration. At large x, the activation barrier for the TSH is not at the tetrahedral site as was assumed in our calculations, but is slightly shifted away from the tetrahedral site as illustrated in section 8.1.3. The error of this approximation is at most 25 meV and diminishes to zero as x is reduced. Finally an error that is more difficult to quantify, arises from the use of the local density approximation of density functional theory. Since hopping rates depend exponentially on the activation barrier, calculated diffusion coefficients are very sensitive to relatively small errors in activation barriers. A systematic error in the calculated activation barrier of 100 meV, a value that is not uncommon for first principles calculations, produces an error of two orders of magnitude in the diffusion coefficient at 300 K.

Due to computational limitations. we have not attempted to calculate a value for the prefactor ν^* given by (8.1) which appears in the hop frequency Γ of equation (7.27). Instead we have assumed a constant value for ν^* and have plotted calculated diffusion coefficients as $(10^{13}/\nu^*)D$, where $10^{13}sec^{-1}$ is a reasonable estimate for ν^*. We expect, however, that the concentration dependence of the prefactor is not negligible. The prefactor depends on the local entropy of a lithium in an octahedral site and a lithium in the activated state. The latter value will be sensitive to concentration since the shape of the energy surface around the tetrahedral site varies qualitatively with lithium concentration. Future studies should address the accurate calculation of the prefactor for diffusion in Li_xCoO_2 to clarify its importance in affecting the diffusion coefficients.

Several experimental studies of the lithium diffusion coefficient in Li_xCoO_2 have been performed in recent years. The different measurements of D qualitatively exhibit a similar concentration dependence. Although, in ref. [173, 174], D is expressed as a function of voltage. the concentration dependence can be inferred by comparison with accurately calibrated voltage versus concentration curves. In ref. [175], D is expressed as a function of concentration, however, comparison of their voltage versus concentration curves with those typically shown in the literature [50, 49] suggest

that the concentration scale in ref [175] is slightly expanded. Typically the lithium concentration attributed to 4.15 V is measured to be 0.5, while that reported in ref [175] is around 0.3, suggesting that the amount of lithium assumed to have been removed from the Li_xCoO_2 during charging is overestimated in ref [175]. After either making the conversions from voltage to concentration for the data of ref [173, 174], or the necessary adjustments in concentration in ref [175], the basic trend in D can be summarized as follows. D drops by almost two orders of magnitude as x is increased between x=0.5 and 0.75 and increases by one to two orders of magnitude as x is increased from x=0.95 to 1. Between x=0.75 and 0.95, a two phase region exists experimentally and a value for D cannot be defined.

As is clear in Fig. 8-6, the calculated D drops by an order of magnitude at x=1/2, a concentration at which the lithium ions order. The stability of the ordered phase at x=1/2 at room temperature is predicted to be much stronger than observed experimentally (see chapter 4). In fact, the order-disorder transition temperature of this phase is over-predicted by 100° C [116]. Furthermore, as the results of chapter 6 illustrated, the stability of the ordered phase at x=1/2 is reduced by the presence of defects such as oxygen vacancies, suggesting that in some samples of Li_xCoO_2, the lithium ordering at x=1/2 may be suppressed altogether. This means that a comparison between the experimental and calculated D cannot be made around x=1/2. Nevertheless, above x=0.65 at 300 K and x=0.6 at 400 K, D exhibits a decreasing trend spanning several orders of magnitude. The comparison with experiment is qualitatively better at 400 K, where the predicted width of the ordered phase at x=1/2 closely approximates the experimentally measured width at room temperature.

The calculated values for D do not exhibit the sharp rise observed experimentally at high x (above x=0.95). We attribute this discrepancy to a difference between the experimental and calculated thermodynamic factors Θ. At x=1, the thermodynamic factor becomes very large, since this concentration corresponds to a stoichiometric compound where the chemical potential deviates strongly from ideality. This is true both experimentally [171] and theoretically (Fig. 8-7). Experimentally, however, there is a two phase region between x=0.75 and x=0.95 which our first principles

cluster expansion fails to predict (see chapter 4). In a two phase region, the thermodynamic factor is zero. Hence the experimental thermodynamic factor, which starts from zero at x=0.95 spans a significantly larger interval than the calculated thermodynamic factor which is not zero at x=0.95. This dramatic increase in the experimental Θ is likely to more than compensate the downward trend of D_J with x to produce a chemical diffusion coefficient D that increases with x. As is clear from D in Fig. 8-6, the calculated Θ, does not increase sufficiently rapidly at high x to compensate the decrease in D_J.

8.5 Conclusion

Our first principles investigation of lithium diffusion in the layered O3 form of Li_xCoO_2 has shown that lithium ions can hop according to two migration paths depending on the local environment around the hopping ion. If lithium migrates to an isolated vacancy, the migration path approximates the shortest distance between the endpoints of the hop. If the end point of the lithium hop is part of a divacancy, the migration path passes through an adjacent tetrahedral site. The activation barrier associated with the divacancy hop mechanism is significantly lower than that associated with the single vacancy hop mechanism. As a result, kinetic Monte Carlo simulations predict that lithium diffusion is mediated by divacancies even at high lithium concentrations where the concentration of divacancies is low.

The activation barrier for the divacancy hop mechanism increases with decreasing lithium concentration. This is caused by the contraction of the O3 host along the c axis at low lithium concentration as well as the increase in the effective valence of the cobalt ions as x is reduced. The strong concentration dependence of the activation barrier results in a diffusion coefficient that varies within several orders of magnitude with lithium concentration.

Although the current investigation of lithium diffusion focussed on layered Li_xCoO_2, similar conclusions are likely to hold for other layered materials with the O3 structure such as Li_xNiO_2 and layered Li_xMnO_2. The understanding that the concentration of

divacancies, the variation of lattice parameter, c, and the change in valence of the transition metal with x are factors that affect lithium transport may lead to strategies to improve the diffusivity in these materials.

Chapter 9

Conclusion

In this thesis, we have performed a comprehensive first principles investigation of the electronic, thermodynamic and kinetic properties of Li_xCoO_2. This transition metal oxide exhibits both technologically important and scientifically interesting properties. Currently, it is the most successful cathode material for rechargeable lithium batteries.

We have focussed on four aspects of Li_xCoO_2.

(i) As a first step, we investigated the changes in electronic properties of Li_xCoO_2 as the lithium concentration is varied (chapter 3). We used density functional theory (DFT) within the local density approximation (LDA) (reviewed in chapter 2) to shed light on the changes in the nature of bonding between cobalt and oxygen as x is varied. This study builds on and further clarifies the work of Aydinol, Ceder and Kohan [108, 114] which had already shown that intercalation of lithium into MO_2 does not result in a shift in the transition metal valence state, as is commonly maintained, but produces an important change in the electron density in the immediate vicinity of the oxygen ions. By performing calculations at intermediate lithium concentrations, we showed that the bonding between cobalt and oxygen progresses from a covalent character to a more ionic character as lithium is added to the CoO_2 host.

(ii) We performed an extensive investigation of phase stability in the Li_xCoO_2 system as a function of lithium concentration x and temperature. We focussed on both the layered and spinel forms of Li_xCoO_2. Since Li_xCoO_2 is characterized by configurational disorder, we implemented the cluster expansion formalism in combi-

nation with density functional first principles calculations (both reviewed in chapter 2), to calculate concentration versus temperature phase diagrams.

For layered Li_xCoO_2 (chapter 4), our calculations predict staging transformations at low lithium concentration. This result clarifies the poorly characterized phase transformations that occur as layered Li_xCoO_2 is deintercalated below x=0.5. The calculations also predict, in agreement with experiment, that the lattice parameter, c, contracts significantly as the lithium concentration approaches x=0. The volumetric changes as well as the sequence of phase stability at low x can be rationalized by the increased covalency of the crystal as x is reduced. A better understanding of the phase transformation and structural properties below x=0.5 is of great value for the efficient and intelligent optimization of this important cathode material.

In our investigation of layered Li_xCoO_2, we have proposed a mechanism by which a metal-insulator transition with concentration can induce a first-order structural phase transformation. We have argued that this mechanism is active in layered Li_xCoO_2 and acts as the driving force for the large two phase coexistence region observed experimentally between x=0.75 and 0.93.

Our study of phase stability of Li_xCoO_2 with a spinel-like crystal structure (chapter 5), has illustrated that many properties exhibited by spinel lithium transition metal oxides such as Li_xMnO_2 [23] and Li_xTiO_2 [37] are determined more by the host crystal structure than by the particular transition metal. The availability to lithium of both tetrahedral and octahedral sites is an important feature of the spinel crystal structure that sets it apart from the layered variants. The fact that the tetrahedral sites are energetically more favorable yet less numerous than the octahedral sites produces a large miscibility gap between x=0.5 and 1.0 in the spinel form. It also results in a large step in the voltage curve at x=1/2 which is a defining characteristic of spinel lithium transition metal oxides.

(iii) As was shown in chapter 5, the host crystal structure has a significant influence on the electrochemical characteristics of a given lithium transition metal oxide. In chapter 6, we demonstrated that defects in the host structure, such as dilute concentrations of oxygen vacancies, also affect the electrochemical properties of a

compound. To perform this study, we have applied for the first time, a local cluster expansion to characterize the effect of dilute defect concentrations on a binary system with configurational disorder. The results of chapter 6 show that oxygen vacancies repel lithium ions and thereby cause a kink in the voltage profile at the initial stages of charge. Furthermore, oxygen vacancies tend to stabilize the disordered phase over ordered phases, resulting in a reduction of order-disorder transition temperatures.

(iv) Since a lithium battery involves significant transport of lithium ions, the lithium mobility within the cathode is an important property. Investigating diffusion in intercalation compounds has several challenges as a result of significant lithium-vacancy disorder. In chapter 7, we introduced a scheme to calculate diffusion coefficients in non-dilute systems from first principles. This procedure makes use of a local cluster expansion to parameterize the environment dependence of the activation barrier.

In chapter 8, we implemented the procedure described in chapter 7 to calculate the lithium diffusion coefficient in layered Li_xCoO_2 as a function of lithium concentration. A first principles investigation of the lithium migration paths between adjacent equilibrium sites showed that two qualitatively different hopping mechanisms are available for lithium ions depending on the lithium-vacancy arrangement surrounding the activated state of the hop. The first migration mechanism, which we have referred to as ODH (see Fig. 8-1(a)), involves an exchange with an isolated vacancy while the second migration mechanism, termed TSH (see Fig. 8-1(b)), requires the presence of a divacancy. The activation barrier associated with the TSH mechanism is predicted to be significantly lower than that of the ODH mechanism. Kinetic Monte Carlo simulations, which rigorously account for the configurational enthalpy and the environment dependent activation barriers with the cluster expansions, predict that the TSH mechanism dominates between x=0 and 1. Diffusion in layered Li_xCoO_2 is, therefore, mediated through a divacancy mechanism.

The activation barrier for the TSH mechanism exhibits an important concentration dependence. As x is reduced, the activation barrier increases due to the contraction of the lattice parameter, c, at low x and the increased effective valence of the Co

Appendix A

Derivation of Kubo-Green equation

In this appendix, we show the mathematical steps that lead from the regression hypothesis Eq. (7.13), to the Kubo-Green equation for the diffusion coefficient (7.14) of chapter 7. The steps in this derivation are purely mathematical and in this appendix, we follow the approach given in ref. [157]. The mathematical manipulations are preformed in Fourier-Laplace space. In the first section of the appendix, we present the Fourier and Laplace transforms of relevant quantities and equations. In the next section, these equations are then manipulated and considered within the hydrodynamic limit to yield the Kubo-Green equation for the diffusion coefficient.

A.1 Fourier-Laplace Transforms

To analyse the continuity equation it is usefull to view it in Fourier space. The spacial Fourier transform of the fluctuation in concentration profile $\delta c(\vec{r},t)$ is defined as

$$\delta c_k(t) = \frac{1}{V}\int_V \delta c(\vec{r},t)e^{-i\vec{k}\vec{r}}d\vec{r} \tag{A.1}$$

where V is the volume of the region under consideration. An analogous equation holds for the Fourier transform of the flux $\vec{J}$. The Fourier components $c_k(t)$ and $\vec{J}_k(t)$

ions with decreasing x. The variation in activation barrier produces a diffusion coefficient that varies within several orders of magnitude with concentration. At high lithium concentration, the mobility of lithium ions is significantly reduced due to the inefficiency of lithium migration through isolated divacancies.

In (k, ω) space, the continuity equation becomes

$$-i\omega\delta\tilde{c}_k(\omega) + k^2 D\delta\tilde{c}_k(\omega) = \delta c_k(0) \tag{A.9}$$

which can be rewritten as

$$\delta\tilde{c}_k(\omega) = \frac{1}{k^2 D - i\omega}\delta c_k(0) \tag{A.10}$$

A.2 Application of the regression hypothesis

To determine the Kubo-Green equation for diffusion, it is necessary to start with the regression hypothesis. In $(\vec{k}, \omega)$ space, the regression hypothesis of Eq. (7.13) takes the form

$$\langle\delta\tilde{c}_k(\omega)\delta c_{-k}\rangle = \frac{1}{\Delta}\langle\delta c_k\delta c_{-k}\rangle \tag{A.11}$$

where δc_{-k} refers to $\delta c_{-k}(0)$ and Δ denotes

$$\Delta = k^2 D - i\omega \tag{A.12}$$

Eq. (A.11) is valid in the hydrodynamic limit. Isolating Δ

$$\frac{1}{\Delta} = \frac{\left\langle\delta\tilde{c}_k(\omega)\delta c_{-k}\right\rangle}{\langle\delta c_k\delta c_{-k}\rangle} \tag{A.13}$$

and taking the inverse laplace transform of both sides yields

$$L^{-1}\left(\frac{1}{\Delta}\right) = \frac{\langle\delta c_k(t)\delta c_{-k}\rangle}{\langle\delta c_k\delta c_{-k}\rangle} \tag{A.14}$$

Taking the time derivative of both sides

$$\frac{d}{dt}L^{-1}\left(\frac{1}{\Delta}\right) = \frac{1}{\langle\delta c_k\delta c_{-k}\rangle}\frac{d}{dt}\langle\delta c_k(t)\delta c_{-k}\rangle \tag{A.15}$$

then satisfy the continuity equation (7.10) expressed in k-space

$$\frac{d\delta c_k(t)}{dt} + i\vec{k}\vec{J}_k(t) = 0 \tag{A.2}$$

The correlation function $S(\vec{r} - \vec{r'}, t)$ as defined by equation (7.12) can be written in k-space according to

$$S_k(t) = \langle \delta c_k(t) \delta c_{-k}(t) \rangle \tag{A.3}$$

This can be seen as follows. We start by explicitly writing out $\delta c_{-k}(t)$ as

$$\delta c_{-k}(t) = \frac{1}{V} \int_V \delta c(\vec{r}, t) e^{i\vec{k}\vec{r}} d\vec{r}. \tag{A.4}$$

If we set $\vec{r'} = \vec{r} + \vec{\tau}$, where $\vec{r}$ appears in the Fourier transform of $\delta c_{-k}(t)$ given by Eq. (A.4), the Fourier transform of $\delta c_k(t)$ becomes

$$\delta c_k(t) = \frac{1}{V} \int_V \delta c(\vec{r'}, t) e^{i\vec{k}\vec{r'}} d\vec{r'} = \frac{1}{V} \int_V \delta c(\vec{r} + \vec{\tau}, t) e^{-i\vec{k}(\vec{r}+\vec{\tau})} d\vec{\tau}. \tag{A.5}$$

and the product of $c_k(t)$ with $c_{-k}(t)$ takes the form

$$S_k(t) = \langle \delta c_k(t) \delta c_{-k}(t) \rangle = \frac{1}{V} \int_V d\vec{\tau} e^{-i\vec{k}\vec{\tau}} \left\langle \frac{1}{V} \int_V \delta c(\vec{r}, t) \delta c(\vec{r} + \vec{\tau}, t) d\vec{\tau} \right\rangle \tag{A.6}$$

which is equivalent to

$$S_k(t) = \frac{1}{V} \int_V d\vec{\tau} e^{i\vec{k}\vec{\tau}} S(\vec{\tau}, t) \tag{A.7}$$

since the term between the brackets in Eq. (A.6) is both an ensemble as well as a spatial average of the correlation function. Eq. (A.7) is by definition the Fourier transform of $S(\vec{\tau}, t)$, showing the validity of Eq. (A.3).

It is also useful to analyse the time evolution of δc and $\vec{J}$ with a Laplace transform defined as

$$\delta \tilde{c}_k(\omega) = \int_0^\infty \delta c_k(t) e^{i\omega t} dt \tag{A.8}$$

followed by a second laplace transform gives

$$L\left(\frac{d}{dt}L^{-1}\left(\frac{1}{\Delta}\right)\right) = \frac{1}{\langle \delta c_k \delta c_{-k}\rangle}\int_0^\infty e^{i\omega t}\frac{d}{dt}\langle \delta c_k(t)\delta c_{-k}\rangle\, dt \tag{A.16}$$

The term on the left hand side can be written as

$$L\left(\frac{d}{dt}L^{-1}\left(\frac{1}{\Delta}\right)\right) = -i\omega\left(\frac{1}{\Delta}\right) - L^{-1}\left(\frac{1}{\Delta}\right)_{t=0} \tag{A.17}$$

and since

$$L^{-1}\left(\frac{1}{\Delta}\right) = e^{-k^2Dt} \tag{A.18}$$

Eq. (A.16) in the long wave length limit becomes

$$\lim_{k\to 0}\left[-i\omega\left(\frac{1}{\Delta}\right) - 1\right] = \lim_{k\to 0}\frac{1}{\langle \delta c_k \delta c_{-k}\rangle}\int_0^\infty e^{i\omega t}\frac{d}{dt}\langle \delta c_k(t)\delta c_{-k}\rangle\, dt \tag{A.19}$$

By Taylor expanding the $1/\Delta$ in k around $k = 0$ up to second order, the left hand side of Eq. (A.19) becomes

$$\lim_{k\to 0}\left[-i\omega\left(\frac{1}{-i\omega} - \frac{k^2D}{(i\omega)^2}\right) - 1\right] = \lim_{k\to 0}\frac{k^2D}{i\omega} \tag{A.20}$$

such that in the hydrodynamic limit ($\omega \to 0$ and $k \to 0$) Eq. (A.19) can be written as

$$D = \lim_{\omega\to 0}\lim_{k\to 0}\frac{i\omega}{k^2}\frac{1}{\langle \delta c_k \delta c_{-k}\rangle}\int_0^\infty e^{i\omega t}\frac{d}{dt}\langle \delta c_k(t)\delta c_{-k}\rangle\, dt \tag{A.21}$$

The time derivative of the correlation in the integrand of Eq. (A.21) can be expressed in terms of the flux using Eq. (A.2) as

$$\frac{d}{dt}\langle \delta c_k(t)\delta c_{-k}\rangle = -i\vec{k}\left\langle \vec{J}_k(t)\delta c_{-k}\right\rangle \tag{A.22}$$

which due to time invariance and the principle of time reversal symmetry at equilibrium is equivalent to [147]

$$= -i\vec{k}\left\langle \vec{J}_k(0)\delta c_{-k}(-t)\right\rangle = i\vec{k}\left\langle \vec{J}_k(0)\delta c_{-k}(t)\right\rangle \tag{A.23}$$

Eq. (A.21) then becomes

$$D = \lim_{\omega \to 0} \lim_{k \to 0} -\frac{\omega}{k^2} \frac{1}{\langle \delta c_k \delta c_{-k} \rangle} \int_0^\infty e^{i\omega t} \vec{k} \left\langle \vec{J}_k(0) \delta c_{-k}(t) \right\rangle dt \tag{A.24}$$

Note that the term $\left\langle \vec{J}_k(0)\delta c_{-k}(t) \right\rangle$ is a vector in a d-dimensional space and the product between $\vec{k}$ and $\left\langle \vec{J}_k(0)\delta c_{-k}(t) \right\rangle$ is a scalar product.

Integrating by parts and using Eq. (A.2), Eq. (A.24) can be written as

$$D = \lim_{\omega \to 0} \lim_{k \to 0} \frac{1}{\langle \delta c_k \delta c_{-k} \rangle} \left[\frac{i\vec{k}}{k^2} \left\langle \vec{J}_k(0) \delta c_{-k}(t) \right\rangle e^{i\omega t}|_0^\infty + \frac{1}{k^2} \int_0^\infty \vec{k} \left\langle \vec{J}_k(0) \vec{J}_{-k}(t) \right\rangle \vec{k} e^{i\omega t} dt \right] \tag{A.25}$$

The first term in Eq. (A.25) vanishes since the time correlation between $\vec{J}_k(0)$ and $\delta c_{-k}(t)$ as $t \to \infty$ vanishes and since $\left\langle \vec{J}_k(0)\delta c_{-k}(0) \right\rangle$ which is a correlation between an odd and an even function at the same time also vanishes. Note that $\left\langle \vec{J}_k(0)\vec{J}_{-k}(t) \right\rangle$ is a tensor that can be represented by a $d \times d$ matrix where d is the dimension of space in which diffusion occurs. The components of the matrix are $\left\langle J_k^\alpha(0) J_{-k}^\beta(t) \right\rangle$ with α and β denoting the components of $\vec{J}$ in for example a cartesian coordinate system. When diffusion is isotropic (*e.g.* in a crystal structure with cubic symmetry with d=3 or on a triangular lattice with d=2), the diagonal terms of the matrix representation of $\left\langle \vec{J}_k(0)\vec{J}_{-k}(t) \right\rangle$ are all equal and the off diagonal terms are zero. The tensor can therefore be replaced by a scalar product $\left\langle \vec{J}_k(0) \cdot \vec{J}_{-k}(t) \right\rangle$ provided we divide by d, the dimension of the vector $\vec{J}$. Eq. (A.25) then becomes

$$D = \lim_{\omega \to 0} \lim_{k \to 0} \frac{1}{\langle \delta c_k \delta c_{-k} \rangle \, d} \int_0^\infty \left\langle \vec{J}_k(0) \vec{J}_{-k}(t) \right\rangle e^{i\omega t} dt \tag{A.26}$$

or after taking the limits

$$D = \frac{1}{\langle (\delta c)^2 \rangle \, d} \int_0^\infty \left\langle \vec{J}(0) \vec{J}(t) \right\rangle dt \tag{A.27}$$

Bibliography

[1] M. S. Whittingham. *Science*, 192:1126, 1976.

[2] M. S. Whittingham. *Prog. Solid State Chem.*, 12:41, 1978.

[3] K. Mizushima, P. C. Jones, P. J. Wiseman, and J. B. Goodenough. *Mat. Res. Bull.*, 15:783, 1980.

[4] M. M. Thackeray, W. I. F. David, P. G. Bruce, and J. B. Goodenough. *Mat. Res. Bull.*, 18:461, 1983.

[5] M. M. Thackeray, P. J. Johnson, L. A. de Picciotto, P. G. Bruce, and J. B. Goodenough. *Mat. Res. Bull.*, 19:179, 1984.

[6] M. M. Thackeray, J. O. Thomas, and M. S. Whittingham. *MRS bulletin*, 25(3):39, 2000.

[7] W. R. McKinnon and R. R. Haering. In R. E. White, J. O. M. Bockris, and B. E. Conway, editors, *Modern Aspects of Electrochemistry*, page 235. Plenum Press, New York, 1983.

[8] G. Ceder and A. Van der Ven. *Electrochimica Acta*, 45:131, 1999.

[9] J. Molenda, A. Stoklosa, and T. Bak. *Solid State Ionics*, 36:53, 1989.

[10] M. Menetrier, I. Saadoune, S. Levasseur, and C. Delmas. *J. Mater. Chem.*, 9:1135, 1999.

[11] T. Ohzuku, M. Kitagawa, and T. Hirai. *J. Electrochem. Soc.*, 137:769, 1990.

[12] A. Yamada and M. Tanaka. *Mater. Res. Bull.*, 30:715, 1995.

[13] J. E. Greedan, N. P. Raju, A. S. Will, C. Morin, S. M. Shaw, and J. N. Reimers. *Chem. Mater.*, 10:3058, 1998.

[14] Y. I. Jang, B. Huang, F. C. Chou, D. R. Sadoway, and Y. M. Chiang. *J. Appl. Phys.*, 87:7382, 2000.

[15] Y. I. Jang, F. C. Chou, and Y. M. Chiang. *Appl. Phys. Lett.*, 74:2504, 1999.

[16] L. D. Dyer, B. S. Borie, J. R. Smith, and G. P. Smith. *J. Am. Chem. Soc.*, 76:1499, 1954.

[17] J. B. Goodenough, D. G. Wickham, and W. J. Croft. *J. Phys. Chem. Solids*, 5:107, 1958.

[18] J. R. Dahn, U. Von Sacken, M. W. Juskow, and J. Al-Janabi. *J. Electrochem. Soc.*, 138:2207, 1991.

[19] J. N. Reimers and J. R. Dahn. *Phys. Rev.*, 46:3236, 1992.

[20] G. A. Nazri, J. M. Tarascon, and M. Armand, editors. *Solid State Ionics III*, number 293 in MRS Symposia Proceedings, Pittsburgh, 1993. MRS.

[21] T. Ohzuku, A. Ueda, and M. Nagayama. *J. Electrochem. Soc.*, 140:1862, 1993.

[22] A. Rougier, P. Gravereau, and C. Delmas. *J. Electrochem. Soc.*, 143:1168, 1996.

[23] M. M. Thackeray. *Prog. Solid State Chem.*, 25:1, 1997.

[24] J. M. Tarascon, W. R. McKinnon, F. Coowar, T. N. Bowmer, G. Amatucci, and D. Guyomard. *J. electrochem. Soc.*, 141(6):1421, 1994.

[25] J. M. Tarascon, F. Coowar, G. Amatucci, F. K. Shokoohi, and D. G. Guyomard. *J. Power sources*, 54(1):103, 1995.

[26] M. M. Thackeray, Y. Shao-Horn, A. J. Kahaian, K. D. Kepler, J. T. Vaughey, and S. A. Hackney. *Electrochem. Solid State Lett.*, 1(1):7, 1998.

[27] G. G. Amatucci, G. N. Schmutz, A. Blyr, C. Sigala, A. S. Gozdz, D. Larcher, and J. M. Tarascon. *J. Power Sources*, 69(1-2):11, 1997.

[28] A. Yamada. *J. Solid State Chem.*, 122(1):160, 1996.

[29] C. Delmas and I. Saadoune. *Solid State Ionics*, 53-56:370, 1992.

[30] C. Delmas, M. Menetrier, L. Croguennec, I Saadoune, A. Rougier, C. Pouillerie, G. Prado, M. Grune, and L. Fournes. *Electrochim. Acta*, 45(1-2):243, 1999.

[31] Y. I. Jang, B. Y. Huang, Y. M. Chiang, and D. R. Sadoway. *Electrochem. Solid State Lett.*, 1(1):13, 1998.

[32] Y. M. Chiang, D. R. Sadoway, Y. I. Jang, B. Y. Huang, and H. F. Wang. *Electrochem. Solid State Lett.*, 2(3):107, 1999.

[33] B. Ammundsen, J. Desilvestro, R. Steiner, and P. Pickering. *IMLB10 poster*, 2000.

[34] H. J. Orman and P. J Wiseman. *Acta Crystallogr., Sect. C:Cryst. Struc. Commun.*, 139:12, 1984.

[35] F. Capitaine, P. Gravereau, and C. Delmas. *Solid State Ionics*, 89:197, 1996.

[36] A. R. Armstrong and P. G. Bruce. *Nature*, 381:499, 1996.

[37] D. W. Murphy, R. J. Cava, S. M. Zahuak, and A. Santoro. *Solid State Ionics*, 9/10:413, 1983.

[38] M. G. S. R. Thomas, W. I. F. David, and J. B. Goodenough. *Mater. Res. Bull.*, 20:1137, 1985.

[39] G. A. Nazri, J. M. Tarascon, and M. Armand, editors. *Solid State Ionics III*, number 293 in MRS Symposia Proceedings, Pittsburgh, 1993. MRS.

[40] E. Rossen, J. N. Reimers, and J. R. Dahn. *Solid State Ionics*, 62:53, 1993.

[41] R. J. Gummow, M. M. Thackeray, W. I. F. David, and S. Hull. *Mater. Res. Bull.*, 27:327, 1992.

[42] B. Garcia, P. Barboux, F. Ribot, A. Kahn-Harari, L. Mazerollesa, and N. Baffier. *Solid State Ionics*, 80:111, 1995.

[43] Y. Shao-Horn, S. A. Hackney, C. S. Johnson, A. J. Kahaian, and M. M. Thackeray. *J. Solid State Chem.*, 140(1):116, 1998.

[44] C. Delmas, C. Fouassier, and P. Hagenmuller. *Physica B*, 99:81, 1980.

[45] G. G. Amatucci, J. M. Tarascon, and L. C. Klein. *J. Electrochem. Soc.*, 143:1114, 1996.

[46] L. Croguennec, C Pouillerie, and C. Delmas. *J Electrochem. Soc.*, 147(4):1314, 2000.

[47] A. A. Balchin. In F. Levy, editor, *Crystallography and crystal chemistry of materials with layered structures*, page 1. D. Reidel Publishing company, Dordrecht-Holland, 1976.

[48] W. D. Kingery, H. K. Bowen, and D. R. Uhlmann. *Introduction to ceramics.* John Wiley and Sons, 1960.

[49] T. Ohzuku and A. Ueda. *J. Electrochem. Soc.*, 141:2972, 1994.

[50] J. N. Reimers and J. R. Dahn. *J. Electrochem. Soc.*, 139:2091, 1992.

[51] P. Hohenberg and W. Kohn. *Phys. Rev.*, 136:B864, 1964.

[52] W. Kohn and L. J. Sham. *Phys. Rev.*, 140:A1133, 1965.

[53] D. Vanderbilt. *Phys. Rev.*, B 41:7892, 1990.

[54] G. Kresse and J. Furthmuller. *Phys. Rev.*, B 54:11169, 1996.

[55] D. de Fontaine. *Solid State Phys.*, 47:33, 1994.

[56] J. M. Sanchez, F. Ducastelle, and D. Gratias. *Physica*, 128A:334, 1984.

[57] H. E. Stanley. *Introduction to Phase Transformations and Critical Phenomena.* Oxford Science Publications, 1971.

[58] J. M. Yeomans. *Statical Mechanics of Phase Transitions.* Oxford Science Publications, 1992.

[59] R. K. Pathria. *Statistical Mechanics, second edition.* Butterworth Heinemann, 1996.

[60] D. A. McQuarrie. *Statistical Thermodynamics.* University Science Books, 1973.

[61] G. Ceder. *Comp. Mater. Sci.*, 144:144, 1993.

[62] J. M. Sanchez, J. P. Stark, and V. L. Moruzzi. *Phys. Rev.*, B 44:5411, 1991.

[63] M. Asta, R. McCormack, and D. de Fontaine. *Phys. Rev.*, B 48:748, 1993.

[64] G. D. Garbulsky and G. Ceder. *Phys. Rev.*, B 49:6327, 1994.

[65] G. D. Garbulsky. *Ground-state structures and vibrational free energy in first principles models of substitutional-alloy thermodynamics.* PhD dissertation, Massachusetts Institute of Technology, Department of Materials Science, 1996.

[66] V. Ozolins, C. Wolverton, and A. Zunger. *Phys. Rev.*, B 58:R5897, 1998.

[67] P. D. Bogdanoff and B. Fultz. *Phil. Mag. B*, 79:753, 1999.

[68] A. van de Walle, G. Ceder, and U. Waghmare. *Phys. Rev. Lett.*, 80:4911, 1998.

[69] A. van de Walle and G. Ceder. *Phys. Rev.*, B 61:5972, 2000.

[70] D. D. Morgan. *Computational Studies of Alloy Phase Stability.* PhD dissertation, University of California, Berkeley, Department of Physics, 1998.

[71] A. van de Walle. *The Effect of Lattice Vibrations in Substitutional Alloy Thermodynamcis.* PhD dissertation, Massachusetts Institute of Technology. Department of Materials Science, 2000.

[72] A. Zunger. In P. E. A. Turchi and A. Gonis, editors, *Statics and Dynamics of Alloy Phase Transformations*, page 361. Plenum, New York, 1994.

[73] K. Binder and D. W. Heermann. *Monte Carlo Simulation in Statistical Physics.* Springer Verlag, 1988.

[74] V. Ozolins. *Structural and Vibrational Properties of Transition Metal Systems from Ab initio Electronic-Structure Calculations.* PhD dissertation, Royal Institute of Technology, Stockholm, Sweden, Department of Physics, 1996.

[75] P. D. Tepesch, G. D. Garbulsky, and G. Ceder. *Phys. Rev. Lett.*, 74:2272, 1995.

[76] C. Wolverton. PhD dissertation, University of California, Berkeley, Department of Physics, 1993.

[77] J. W. D. Connolly and A. R. Williams. *Phys. Rev.*, B 27:5169, 1983.

[78] Z. W. Lu, S. H. Wei, A. Zunger, A. Frota-Pessoa, and L. G. Ferreira. *Phys. Rev.*, B 44:512, 1991.

[79] M. Asta. *First-Principles Calculations of Thermodynamic Properties and Phase Diagrams of Binary Substitutional Alloys.* PhD dissertation, University of California, Berkeley, Materials Physics, 1993.

[80] G. D. Garbulsky and G. Ceder. *Phys. Rev.*, B 51:67, 1995.

[81] L. G. Ferreira, A. A. Mbaye, and A. Zunger. *Phys. Rev.*, B 35:6475, 1987.

[82] L. G. Ferreira, A. A. Mbaye, and A. Zunger. *Phys. Rev.*, B 37:10547, 1988.

[83] D. B. Laks, L. G. Ferreira, S. Froyen, and A. Zunger. *Phys. Rev.*, B 46:12587, 1992.

[84] N. W. Ashcroft and N. D. Mermin. *Solid State Physics.* Saunders College Publishing, 1976.

[85] O. Madelung. *Introduction to Solid State Theory.* Springer Verlag, 1978.

[86] R. G. Parr and W. Yang. *Density Functional Theory of Atoms and Molecules.* Oxford University Press, 1989.

[87] R. O. Jones and O. Gunnarsson. *Rev. Mod. Phys.*, 61:689, 1989.

[88] M. Levy. *Proc. Natl. Acad. Sci.*, 76:6062, 1979.

[89] J. P. Perdew and A. Zunger. *Phys. Rev.*, B 23:5048, 1981.

[90] D. M. Ceperley and B. J. Alder. *Phys. Rev. Lett.*, 45:566, 1980.

[91] V. I. Anisimov, F. Aryasetiawan, and A. I. Lichtenstein. *J. Phys.:Condens. Matter*, 9:767, 1997.

[92] Z. Szotek, W. M. Temmerman, and H. Winter. *Phys. Rev.*, 47:4029, 1993.

[93] M. M. Rieger and P. Vogl. *Phys. Rev.*, 52:16567, 1995.

[94] S. Goedecker and C. J. Umrigar. *Phys. Rev.*, A 55:1765, 1997.

[95] A. F. Kohan and G. Ceder. *Comp. Mat. Sci.*, 8(1-2):142, 1997.

[96] A. F. Kohan. *Total-energy models for phase-stability studies in multicomponent oxides.* PhD dissertation, Massachusetts Institute of Technology, Department of Materials Science, 1997.

[97] D. J. Singh. *Planewaves, Pseudopotentials and the LAPW Method.* Kluwer Academic Publishers, 1994.

[98] J. C. Phillips and L. Kleinman. *Phys. Rev.*, 116:287, 1959.

[99] M. C. Payne, M. P. Teter, D. C. Allan, T. A. Arias, and J. D. Joannopoulos. *Rev. Mod. Phys.*, 64:1045, 1992.

[100] C. Wolverton. *private communication*, 1997.

[101] D. R. Hamann, M. Schluter, and C. Chiang. *Phys. Rev. Lett.*, 43:1494, 1979.

[102] G. B. Bachelet, D. R. Hamann, and M. Schluter. *Phys. Rev. B*, 26:4199, 1982.

[103] L. Kleinman and D. M. Bylander. *Phys. Rev. Lett.*, 48:1425, 1982.

[104] A. M. Rappe, K. M. Rabe, E. Kaxiras, and J. D. Joannopoulos. *Phys. Rev. B*, 41:1227, 1990.

[105] N. Troullier and J. L. Martins. *Phys. Rev. B*, 43:1993, 1991.

[106] D. M. Wood and A. Zunger. *J. Phys. A: Math. Gen*, 18:1343, 1985.

[107] G. Kresse and J. Furthmuller. *Comp. Mat. Sci.*, 6:15, 1996.

[108] G. Ceder, M. K. Aydinol, and A. F. Kohan. *Comp. Mat. Sci.*, 8:161, 1997.

[109] M. C. Day and J. Selbin. *Theoretical Inorganic Chemistry.* Reinhold Publishing corporation, 1962.

[110] C. J. Ballhausen. *Introduction to Ligand Field Theory.* McGraw-Hill, 1962.

[111] T. M. Dunn, D. S. McClure, and R. G. Pearson. *Crystal Field Theory.* Harper and Row, 1965.

[112] L. H. Hall. *Group Theory and Symmetry in Chemistry.* McGraw-Hill, 1969.

[113] M. T. Czyzyk, R. Potze, and G. A. Sawatzky. *Phys. Rev.*, 46:3729, 1992.

[114] M. K. Aydinol, A. F. Kohan, G. Ceder, K. Cho, and J Joannopoulos. *Phys. Rev.*, B 56:1354, 1997.

[115] J. van Elp, J. L. Wieland, H. Eskes, P. Kuiper, G. A. Sawatzky, F. M. F. de Groot, and T. S. Turner. *Phys. Rev.*, B 44:6090, 1991.

[116] A. Van der Ven, M. K. Aydinol, G. Ceder, G. Kresse, and J. Hafner. *Phys. Rev.*, B 58:2975, 1998.

[117] C. Wolverton and A. Zunger. *Phys. Rev. Lett.*, 81:606, 1998.

[118] A. Van der Ven, M. K. Aydinol, and G. Ceder. *J. Electrochem. Soc.*, 145:2149, 1998.

[119] C. Wolverton and A. Zunger. *Phys. Rev.*, B 57:2242, 1998.

[120] S. A. Safran. *Solid State Phys.*, 40:183, 1987.

[121] C. Delmas. *private communication*, 1999.

[122] H. Tukamoto and A. R. West. *J. Electrochem. Soc.*, 144:3164, 1997.

[123] M. K. Aydinol and G. Ceder. *J. Electrochem. Soc.*, 144:3832, 1997.

[124] E. Deiss, A. Woaun, J. L. Barras, C. Daul, and P. Dufek. *J. Electrochem. Soc.*, 144:3877, 1997.

[125] L. Benco, J. L. Barras, M. Atanasov, C. A. Daul, and E. Deiss. *Solid State Ionics*, 112:225, 1998.

[126] C. Wolverton and A. Zunger. *J. Electrochem. Soc.*, 145:2424, 1998.

[127] R. Benedek, M. M. Thackeray, and L. H. Yang. *Phys. Rev.*, B 60:6335, 1999.

[128] M Vanschilfgaarde. *private communication*, 1998.

[129] J. R. Dahn and W. R. McKinnon. *J. Phys. C*, 17:4231, 1984.

[130] A. Daumas and C. R. Herold. *Hebd. Seances Acad. Sci. Ser. C*, 286:373, 1969.

[131] W. C. Mackrodt, N. M. Harrison, V. R. Saunders, N. L. Allan, and M. D. Towler. *Chem. Phys. Lett.*, 250:66, 1996.

[132] V. G. Bhide, D. S. Rajoria, C. N. R. Rao, G. Rama Rao, and V. G. Jadhao. *Phys. Rev.*, B12:2832, 1975.

[133] C. N. R. Rao, Om Parkash, D. Bahadur, P. Ganguly, and S. Nagabhushana. *J. Solid State Chem.*, 22:353, 1977.

[134] J. Rodriquez-Carvajal, G. Rousse, C. Masquelier, and M. Hervieu. *Phys. Rev. Lett.*, 81:4660, 1998.

[135] G. Rousse, C. Masquelier, J. Rodriguez-Carvajal, and M. Hervieu. *Electrochem. Solid-State Lett.*, 2:1, 1999.

[136] A. Van der Ven and G. Ceder. *Phys. Rev.*, B 59:742, 1999.

[137] A. Van der Ven, C. Marianetti, D. Morgan, and G. Ceder. *Sol. State Ionics in press*, 2000.

[138] H. Wang, Y. I. Jang, B. Huang D. R. Sadoway, and Y. M. Chiang. *J. Electrochem. Soc.*, 146:473, 1999.

[139] M. S. Whittingham, R. Chen, T. Chiryil, and P. Zavalij. *Solid State Ionics*, 94:227, 1997.

[140] M. Tabuchi, K. Ado, H. Kobayashi, H. Kageyama, C. Masquelier, A. Kondo, and R. Kanno. *J. Electrochem. Soc.*, 145:L49, 1998.

[141] Y. I. Jang, B. Huang, Y. M. Chiang, and D. R. Sadoway. *Electrochem. Solid State Lett.*, 1:13, 1998.

[142] S. K. Mishra and G. Ceder. *Phys. Rev.*, B 59:6120, 1999.

[143] R. J. Gummow and M. M. Thackeray. *J. Electrochem. Soc.*, 141:1178, 1994.

[144] J. N. Reimers, E. W. Fuller, E. Rossen, and J. R. Dahn. *J. Electrochem. Soc.*, 140:3396, 1993.

[145] S. Levasseur, M. Menetrier, E. Suard, and C. Delmas. *Solid State Ionics*, 128(1-4):11, 2000.

[146] T. Takahashi, E. J. Wu, A. Van der Ven, and G. Ceder. *Jpn. J. Appl. Phys.*, 139(3A):1241, 2000.

[147] S. R. de Groot and P. Mazur. *Non-Equilibrium Thermodynamics*. Dover Publications, 1984.

[148] W. Yourgrau, A. van der Merwe, and G. Raw. *Treatise on Irreversible and Statistical Physics*. MacMillan, 1966.

[149] R. Kubo. *J. Phys. Soc. Jpn.*, 12:570, 1957.

[150] R. Kubo, M. Yokota, and S. Nakajima. *J. Phys. Soc. Jpn.*, 12:1203, 1957.

[151] R. Zwanzig. *J. Chem. Phys.*, 40:2527, 1964.

[152] R. Zwanzig. *Annu. Rev. Phys. Chem.*, 16:67, 1965.

[153] L. Onsager. *Phys. Rev.*, 37:405, 1931.

[154] L. Onsager. *Phys. Rev.*, 38:2265, 1931.

[155] L. P. Kadanoff and P. C. Martin. *Ann. Phys.*, 24:419, 1963.

[156] R. Gomer. *Rep. Prog. Phys.*, 53:917, 1990.

[157] Y. Zhou and G. H. Miller. *J. Phys. Chem.*, 100:5516, 1996.

[158] G. H. Vineyard. *J. Phys. Chem. Solids*, 3:121, 1957.

[159] C. Uebing and R. Gomer. *J. Chem. Phys.*, 95:7626, 1991.

[160] W. M. Franklin. In A. S. Nowick and J. J. Burton, editors, *Diffusion in Solids*, page 1. Academic, New York, 1975.

[161] K. C. Pandey and E. Kaxiras. *Phys. Rev. Lett.*, 66:915, 1991.

[162] G. DeLorenzi, C. P. Flynn, and G. Jacucci. *Phys. Rev.*, 30:5430, 1984.

[163] A. Antonelli, S. Ismail-Beigi, E. Kaxiras, and K. C. Pandey. *Phys. Rev.*, 53:1310, 1996.

[164] G. Mills, H. Jonsson, and G. K. Schenter. *Surf. Sci.*, 324:305, 1995.

[165] E. Kaxiras and K. C. Pandey. *Phys. Rev.*, B 47:1659, 1993.

[166] E. Kaxiras and J. Erlebacher. *Phys. Rev. Lett*, 72:1714, 1994.

[167] F. Bulnes, V. Pereyra, and J. L. Riccardo. *Phys. Rev.*, E 58:86, 1998.

[168] K. W. Kehr and K. Binder. In K. Binder, editor, *Applications of the Monte Carlo Method in Statistical Physics*, page 181. Springer Verlag, Berlin, 1984.

[169] M. Tringides and R. Gomer. *Surf. Sci.*, 145:121, 1984.

[170] C. Uebing and R. Gomer. *J. Chem. Phys.*, 100:7759, 1994.

[171] A. Van der Ven and G. Ceder. *Electrochem. Solid State Lett.*, 3(7):301, 2000.

[172] G. Nuspl, M. Nagaoka, K. Yoshizawa, F. Mohri, and T. Yamadbe. *Bull. Chem. Soc. Jpn*, 71:2259, 1998.

[173] M. D. Levi, G. Salitra, B. Markovsky, H. Teller, D Aurbach, U. Heider, and L. Heider. *J. Electrochem. Soc.*, 146(4):1279, 1999.

[174] J. M. McGraw, C. S. Bahn, P. A. Parilla, J. D. Perkins, D. W. Readey, and D. S. Ginley. *Electrochim Acta*, 45(1-2):187, 1999.

[175] J. Barker, R. Pynenburg, R. Koksbang, and M. Y. Saidi. *Electrochim. Acta*, 41(15):2481, 1996.